Mechanical Behavior of Silicon as Anode Material for Lithium-ion Batteries

by

Michael Jong-Hoon Chon

Sc. B., Engineering, Brown University, 2009
Sc. M., Engineering, Brown University, 2012

A dissertation submitted in partial fulfillment of the
requirements for the Degree of Doctor of Philosophy
in the School of Engineering at Brown University

Providence, Rhode Island
May 2016

This dissertation by Michael Jong-Hoon Chon is accepted in its present form
by the School of Engineering as satisfying the
dissertation requirement for the degree of Doctor of Philosophy.

Date _____ _____

Pradeep R. Guduru, Director

Recommended to the Graduate Council

Date _____ _____

Eric Chason, Reader

Date _____ _____

Christian Franck, Reader

Date _____ _____

Brian Sheldon, Reader

Approved by the Graduate Council

Date _____ _____

Peter M. Weber

Dean of the Graduate School

Vitæ

Michael J. Chon was born on January 9th, 1987 in Paraguay but grew up in Lincolnwood, Illinois — a neighboring suburb of Chicago. He credits his love of learning to the caring and passionate teachers throughout his public schooling at Lincolnwood School District 74 and Niles West High School District 219. In the fall of 2005, he began his formative career at Brown University as an undergraduate student concentrating in Engineering, before earning a Masters degree in 2012 en route to his Doctoral thesis defense in the winter of 2016. Along the way, he taught and mentored middle school students, wrote software in Silicon Valley, built houses in New Orleans, hiked the Appalachian Trail, learned to snowboard in Vermont, built bicycles and met his wife, Anna.

Dedicated to My Family

Acknowledgements

I would like to extend my deepest gratitude to my thesis advisor, Professor Pradeep Guduru, for his guidance and support throughout my doctoral studies. I am truly privileged to have been mentored by a scholar of great integrity, high standards and interminable patience.

I want to thank Prof. Janet Blume for her guidance and encouragement that ultimately led me to enroll in the PhD program at Brown, Prof. Ben Freund for the impromptu life lessons and kind words – both in and out of the classroom, Prof. K-S Kim for his support and mentorship during the summer of 2009, Prof. Allan Bower for always keeping his door open for conversations, Prof. Christian Franck for his enthusiastic support and encouragement, and Prof. Huajian Gao for his kindness and wisdom over the years. It has been a great honor to walk the same halls as you all.

I am grateful to my qualification exam and thesis committee members for their time, thoughts and directives. I hold their critique, encouragement and advice in the highest regard.

I want to acknowledge the staff at Brown University that have made all the little things possible: the core facility managers (Tony McCormick, Michael Jibitsky, Bill Patterson), the machinists at JEPIS (Charlie, Mike and Ray), the staff in Prince Lab (Chris Bull, Brian Corkum, Paul Waltz), the administrative assistants (Stephanie, Pat, Diane, Peggie, Tara and everyone on the 3rd floor), Todd the 6th floor janitor, and every DPS officer who has come to my rescue whenever I locked myself out of the lab in the middle of the night.

Thank you, Louis Restaurant, for gifting us with the Drunk Johnny omelet and

Muffin Mondays.

A quick shout out to my colleagues and fellow grad students: Jennet Toyjanova, Eyal Bar-Kochba, John DiBenedetto, Sean Teller, Rye Waldman, Greg Rizza, Maria Stournara, Gerry Della Rocca, Lee Cronin-Fine, Jay Sheth, Insun Yoon, Odysseus Skartsis, Anton Tokranov, Ravi Kumar, Siva Nadimpalli, Vijay Sethuraman, Naba Karan, Ron Dunn, Nitin Jadhav, Shaghayegh, Max Monn and everyone else at Brown.

A deep appreciation to my church community in Rhode Island for their constant support and companionship: Carlos Soto, Amber Ma, Scott Yi, Jackie & Roger Plante, the Axtmanns, Jason Jason Lee Lee, David Atkinson, Lorenna Ellis, Greg & Sarah Cowan Johnson, and Hope Muller.

I thank my beautiful wife, Anna, for her love and support. You know she loves you when she'll forego the sunny beaches of Southern California and endure snowy New England winters to be by your side as you finish up your Ph.D.

Finally, I want to thank my parents for the hardships endured and sacrifices made to give my brother and I the opportunity to thrive as individuals.

Soli Deo gloria

Contents

List of Tables

List of Figures

Chapter 1

Introduction

The viability of electric vehicles (EVs) as clean, environmentally-conscious means of transportation is quickly maturing from idealism to reality. The introduction of higher energy density battery technologies has been especially important in bringing full-battery powered EVs to mass appeal. Compared to early EVs that used lead-acid (Pb-A) or nickel metal hydroxide (Ni-MH) batteries, lithium-ion battery-powered EVs offer significantly higher range and performance while keeping manufacturing costs comparable to traditional vehicles (see Figure 1.1 and Table 1.1). Since the reintroduction of commercial EVs with lithium-ion batteries in the mid-2000s, the total number of EVs on the road has reached over 740,000 units globally [1]. By 2030, hybrid, plug-in hybrid and pure battery electric vehicles (HEV, PHEV, BEV, respectively) may account for more than half of new light-duty, passenger vehicle sales [2].

Still, further improvements to battery technologies are needed in order for EVs to become practical alternatives to traditional internal combustion engine (ICE) vehicles. Consider, as an elementary argument, the fuel cost savings of driving a Tesla Model S – a full-sized luxury sedan – versus a comparable ICE vehicle (Table 1.2); one would have to drive about 300,000 miles in order to recover the upfront cost of the Tesla. Assuming 15,000 miles are driven per year, the vehicle (and its battery) must last over 20 years and between 3000-4000 charge cycles to reach this milestone. Alternatively,

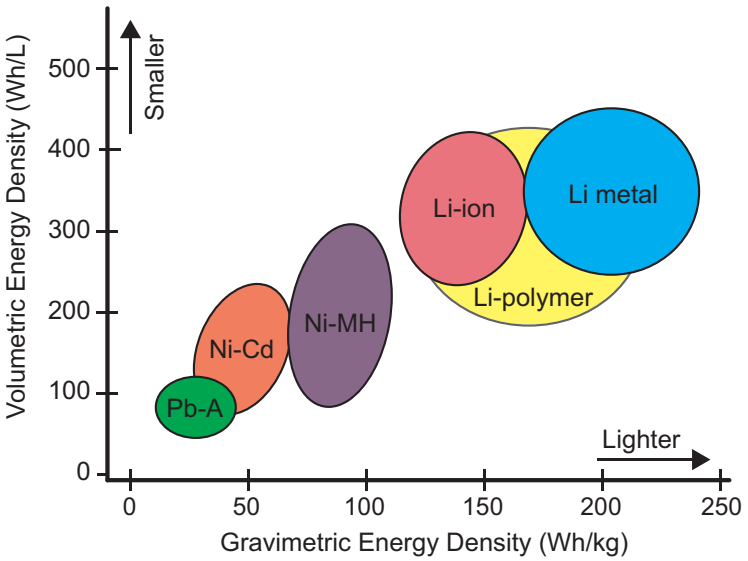

Figure 1.1: Theoretical energy per unit weight (horizontal axis) and volume (vertical axis)for currently available rechargeable battery technologies. Lithium-ion (Li-ion) batteries offer both higher gravimetric and volumetric energy densities than its predecessors. Adapted from Ref. [3] with permission.

smaller EVs like the Nissan LEAF are more affordable options that lower the upfront costs of ownership by opting for a smaller battery. The battery pack's reduced size and weight allows for higher energy efficiency and lower overall costs, even though its energy density is almost half of the Tesla's battery pack. However, the reduced capacity results in limited range and more frequent charging, increasing the wear on the battery pack. Thus, efforts to bring wider adoption of EVs have focused on reducing the battery's manufacturing costs, increase their capacity and improve their durability.

Higher Energy Density Batteries

One of the strategies to increase the energy density batteries of Li-ion batteries is to develop electrode materials with higher specific capacities (charge per unit weight). A typical commercial Li-ion battery utilizes graphite as the negative electrode (anode) and a Li-metal oxide – e.g., $LiCoO_2$ or $LiFePO_4$ – as the positive electrode (cathode).

Table 1.1: A comparison of BEVs in the U.S. market.

Vehicle (Model Year)	GM EV1 (1997)[4]	GM EV1 (1999)[5]	Nissan LEAF (2011)[6, 7]	Tesla Model S (2015)[8, 9]
Curb Weight	1,400 kg	1,319 kg	1,552 kg	2,188 kg
Battery Type	Pb-A	NI-MH	Li-ion	Li-ion
Batt. Weight	594 kg	481 kg	294 kg	544 kg
Batt. Capacity	18.7 kWh	26.4 kWh	24 kWh	85 kWh
Approx. Range	60 mi.	160 mi.	107 mi.	270 mi.
Specific Energy	31 Wh/kg	54 Wh/kg	81 Wh/kg	156 Wh/kg
Efficiency	311 Wh/mi.	165 Wh/mi.	224 Wh/mi.	315 Wh/mi.

As the battery is charged and discharged, Li^+ ions are shuttled back and forth between the two electrodes via an ionically conductive electrolyte as current flows in an external circuit (Figure 1.2).

On the cathode side, there has been great interest in developing organic compounds to replace the transition metal oxides found in current cathode materials. The building blocks of organic materials (carbon, nitrogen, oxygen, etc.) are readily available, inexpensive and the ability to fine tune these compounds make them especially promising. Additionally, the prospect of replacing expensive materials like cobalt (Co) makes them even more attractive. Currently, reversible capacities for sulfur-based organic cathodes have been reported to reach 300 mAh/g – over twice that of $LiCoO_2$ (120 mAh/g) – though capacities as high as 1320 mAh/g have been reported under controlled circumstances [3, 10–12]. On the anode side, elements such as silicon (Si), tin (Sn) and germanium (Ge) have been identified as candidates for high energy density electrode materials. Silicon is a particularly promising material: it is non-toxic, abundant and has a gravimetric capacity 10 times that of graphite (3579 mAh/g for Si vs. 372 mAh/g for graphite)[13].

As a consequence of increased energy density, however, there is a higher concen-

Table 1.2: Fuel cost for an EV versus a traditional ICE

Vehicle	Nissan LEAF	Tesla Model S	Traditional ICE
MSRP	$30,000	$75,000	$45,000
Fuel Type	Electric	Electric	Gasoline
Fuel Capacity	24 kWh	85 kWh	18 gal
Maximum Range	107 mi	270 mi	396 mi
Fuel Efficiency	224 Wh/mi	315 Wh/mi	25 mi/gal
Fuel Cost	$0.11/kWh	$0.11/kWh	$3.00/gal
Fuel Cost/mi.	$0.025/mi	$0.037/mi	$0.14/mi

tration of Li atoms in these electrodes, resulting in large volumetric changes during cycling. Silicon, for example, undergoes volumetric strains as high as 270% at maximum capacity. These strains lead to mechanical degradation of the active material and the surrounding binder material, resulting in rapid capacity fade and poor durability [3, 14, 15].

As a result, much effort has been put into designing complex nano- and micro-scale anode architectures that can accommodate these strains and mitigate mechanical failure. Examples include nanowires, microstructures, nanoporous particles, nanoparticles, and encapsulated particles [15–34]. However, design of these architectures still lack basic understanding of the mechanics of the constituent materials, structures and interfaces. As such, quantifying the mechanical behavior and failure criteria – and how they evolve during cycling – are fundamentally significant contributions to the scientific community and battery industry. Ultimately, a detailed mechanics description of the electrode microstructures and the interaction between stress and electrochemistry are necessary to arrive at robust materials choice, process design and optimized performance.

The goal of this thesis is to present an experimental effort to characterize the physical behavior and mechanical properties of silicon as a lithium-ion battery elec-

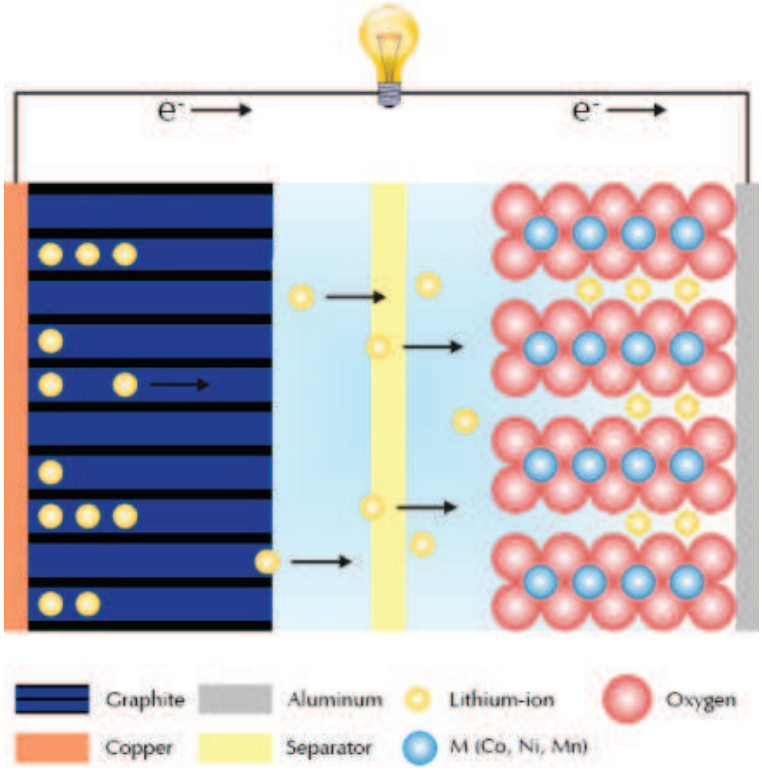

Figure 1.2: Schematic of a Li-ion battery during discharge. Li^+ ions travel from the negative electrode (anode) to the positive electrode (cathode) as current flows in an external circuit. From "Testing Lithium Ion Batteries" (https://www.gamry.com/application-notes/battery-research/testing-lithium-ion-batteries/). Copyright 2015 Gamry Instruments. Retrieved November 20, 2015. Reprinted with permission.

trode material. Silicon is chosen as the prototypical material in this study given its property as an amorphous, mechanically isotropic material at room temperature and the large body of literature that already exists on the electrochemical and mechanical performances of silicon-based anodes. The following techniques can be adapted towards other high energy density electrode materials.

In Chapter 2, the Multi-beam Optical Sensing (MOS) technique is utilized to measure *in situ* stress evolution of a thin film silicon electrode (TFSE). The goal is to apply this optical method to measure stress in electrodes during electrochemical cycling. The results show that the yield stress of lithiated silicon decreases with increasing lithium concentration and the TFSE exhibits extensive plasticity during

one lithiation/delithiation cycle. Motivated by these results, efforts are made to measure the biaxial modulus $M = \frac{E}{1-\nu}$ as a function of Li composition (c), as well as calculate the energy dissipation of the electrode due to plasticity.

In Chapter 3, a thermodynamic argument is made for a coupling behavior between stress and cell potential in lithiated silicon. This model is validated with an experimental setup that applies a mechanical load to a TFSE independently from electrochemical measurements. Based on the results of these experiments, modifications to current models are recommended. In Chapter 4, an experimental setup to observe a pre-crack in a TFSE during electrochemical cycling is demonstrated. Coupled with *in situ* stress measurements, this setup is used to report the fracture energy of lithiated silicon at various Li-Si compositions using linear elastic fracture mechanics.

Chapter 2

In situ Stress Measurements

The contents of this chapter have appeared in earlier publications [35–41]. Since then, publications based on these results have been reproduced by other investigators [42–50].

2.1 Introduction

In situ stress measurements in electrodes have been made in a wide variety of electrochemical systems [51–59]. These measurements were based on a cantilever beam-deflection (CBD) method developed by G.G. Stoney in 1901 in which the curvature of a steel substrate was used to calculate the stress in a nickel film during electrodeposition [60, 61]. Some of these studies were conducted on cathode electrode materials for lithium-ion batteries though none of them have gone beyond reporting stress evolution[51, 53, 55]. Furthermore, no attempts were made to calculate mechanical dissipation or establish a quantitative connection between stress evolution and mechanical damage.

Despite the prevailing view that silicon electrodes suffer from severe mechanical damage due to large volumetric strains, there has been limited effort to quantify the stress generated in silicon anodes during cycling. Prior to the work presented in this thesis, there was only one reported effort by Lee *et al.* to measure stress evolution in silicon electrodes during electrochemical cycling. Using the CBD method, Lee *et al.* [62] reported substrate deflection voltages with lithiation and delithiation cycles

(Figure 2.1). Correlating the decrease in deflection voltage in Figure 2.1a to a higher rate of capacity fade than in Figure 2.1b, Lee concluded that the volume expansion between 0.1 V to 0 V results in fracture of the film that contributes to capacity fade. However, these observations were only qualitative and no attempt was made to convert the beam deflection voltages to stress measurements. Furthermore, the CBD method is highly susceptible to measurement error and mechanical vibrations [63], compromising both the accuracy and precision of stress measurements.

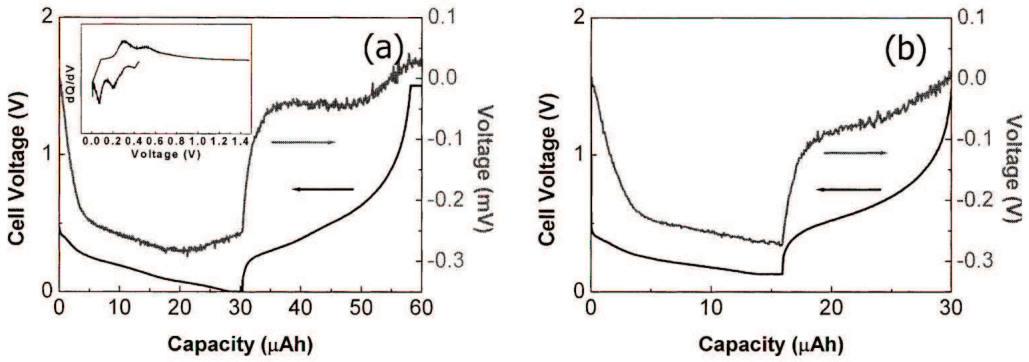

Figure 2.1: Cell potential and CBD beam deflection voltage from Lee et al. [62]. The lower curve is the cell voltage vs. Li metal reference electrode (left y-axis); the upper curve is the voltage reading from the position sensor (right y-axis), which is analogous to the substrate curvature. Reprinted with permission.

The focus of this chapter is to measure the stress evolution of thin film silicon electrodes in real time using an experimental method that circumvents many of the issues experienced by the CBD technique. Using this method, we also compare the mechanical dissipation in the electrode during cycling with other polarization losses and directly measure the biaxial modulus of the electrode as a function of Li concentration.

2.2 Substrate Curvature Measurement Techniques

2.2.1 Cantilever Beam Deflection

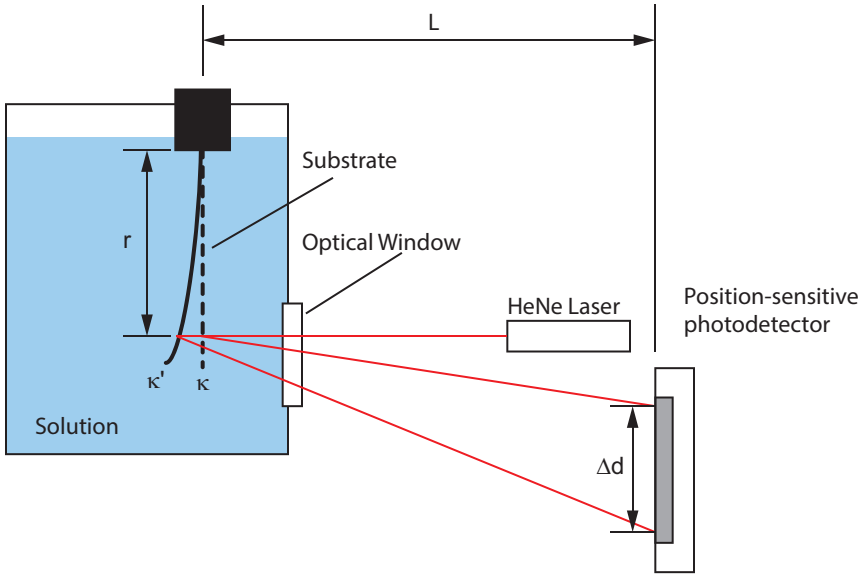

Figure 2.2: Schematic of the optical setup for the cantilever beam deflection (CBD) method. The curvature of the substrate is calculated from the change in position of the laser beam (Δd) following Equation 2.1. Adapted from Ref. [64] with permission.

In the cantilever beam-deflection (CBD) method, an elastic substrate is clamped at one end and an incident laser beam is reflected off the substrate surface and captured on a position detector (Figure 2.2). As the substrate's curvature changes due to film stress, the position of the reflected beam onto a photo-detector also changes. The substrate curvature (κ_s) is inferred from the translation of the beam position (Δd) using the relation,

$$\Delta\kappa_s = \frac{\Delta d}{2rL} \tag{2.1}$$

where r is the distance between the clamped end and the incident beam on the substrate and L is the distance from the sample to the position detector 2.2. The change in the film stress ($\Delta\sigma_f$) is then taken from the substrate curvature using the

Stoney equation [60],

$$\Delta\sigma_f = \frac{E_s {h_s}^2}{6\,(1-\nu_s)\,h_f}\Delta\kappa_s \tag{2.2}$$

where h_s is the substrate thickness, h_f is the film thickness, and E_s and ν_s are the Young's modulus and Poisson ratio of the substrate taken along the measured curvature.

Although this is the typical method for measuring film stresses in electrochemical systems, its sensitivity to the beam position introduces challenges in accurately characterizing the stress evolution of silicon anodes. Notably, this method is susceptible to ambient mechanical vibrations that increase the level of noise in the curvature measurements. Since lithium-ion battery experiments are often conducted inside inert atmospheric glove box systems, the effectiveness of vibration-isolation systems are limited by the close proximity to mechanical vibrations and available space inside the glove box. This method also has inherent measurement uncertainties when accounting for residual stresses during silicon film deposition (σ_r). Fabricating thin film silicon electrodes typically requires transporting the substrates to a separate clean room facility, which introduces challenges in measuring the curvature change due to film deposition without including uncertainties due to the change in position of the substrate. This method is also sensitive to ambient temperature variations (i.e., seasonal and day/night variations), adding yet another source of error. Furthermore, an analysis of this method carried out by Láng *et al.* showed that severe errors in measurement can result if the refractive indices and incident angles of each media through which the laser beam travels are not accounted for or accurately known [63].

2.2.2 Multi-beam Optical Sensing

Alternatively, Multi-beam Optical Sensing (MOS) is an optical technique that can overcome many of the limitations of CBD by employing an array of parallel laser beams to measure curvature changes of a substrate (Figure 2.3). This technique was

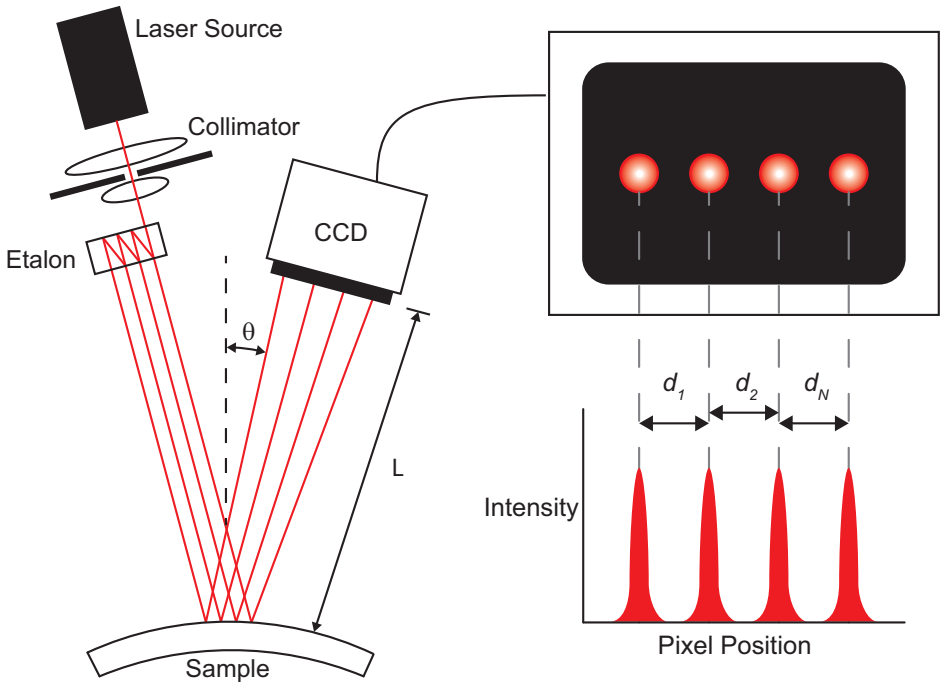

Figure 2.3: Schematic of a MOS setup using a linear array of laser spots.

developed by Chason *et al.* and has been used to monitor thin film stress in a variety of applications [61, 65–67].

A laser source generates an incident beam that is filtered and focused, then passed through an etalon to produce an array of equally spaced, parallel laser beams. The beams reflect off the substrate onto a CCD camera that captures the array, while image processing software tracks the pixel position of the centroid of each laser spot in real-time. By measuring the peak-to-peak distance of adjacent laser spots (d), the change in substrate curvature ($\Delta\kappa_s$) is calculated using the relation,

$$\Delta\kappa_s = \frac{d - d_0}{d_0}\left(\frac{1}{A_m}\right) \tag{2.3}$$

where d_0 is the initial distance and A_m is the mirror constant. A_m is essentially a conversion factor that is a function of the path length (L) and incident angle (θ) of the reflected beam:

$$A_m = 2L/\cos\theta \tag{2.4}$$

In addition to measuring L and θ, A_m can also be quickly and accurately determined by measuring the differential curvature ($\kappa^D = \frac{d-d_0}{d_0}$) from a curved reference mirror (κ =0.1 m^{-1}) after acquiring d_0 from a flat reference mirror. This eliminates many sources of experimental error by requiring just one measurement for calibration. Since A_m is sensitive to both path length and incident angle, it is periodically updated to account for any configurational adjustments to the MOS setup.

The advantage of using the relative distance between laser spots to measure substrate curvature rather than beam deflection is that this method is not sensitive to mechanical vibrations or rigid body motion of the substrate. This allows greater flexibility with sample orientation and placement for residual stress measurements. Additionally, this eliminates the need for vibration-isolation equipment due to improved signal-to-noise ratio in the measurements. It is also possible to use a second etalon oriented perpendicularly to the first to create a 2-D array of laser spots, allowing for curvature measurements in two orthogonal directions. Since the beams are directed onto a CCD camera, live images of the spots simplify the process of alignment and focusing of the beams.

2.3 Experimental

Thin film silicon electrodes (TFSEs) are electrochemically cycled in a custom Li-Si beaker cell with Li metal as the counter electrode (Figure 2.5). The TFSEs are fabricated using RF magnetron sputtering onto a mechanically isotropic wafer substrate, resulting in an amorphous silicon film. An optical-grade window on the cover of the beaker cell allows for *in situ* MOS curvature measurements of the substrate. As the TFSEs are electrochemically alloyed with lithium, they experience volumetric strains proportional to its Li content – as high as 270% at full lithiation [68]. The substrate constrains the in-plane displacements ($\varepsilon_{11} = \varepsilon_{22} = 0$) which result in large in-plane stresses in the film (σ_f), while out-of-plane components of stress are taken to be zero.

As the TFSEs are lithiated and delithiated, the stress changes in the film induce changes to the substrate's curvature. By monitoring the substrate curvature, the average stress in the film can be determined using Equation 2.2 after accounting for the height of the film due to volume expansion.

2.3.1 Sample Preparation

Fused silica wafers (double-side polished, 50 mm diameter, ∼500 µm thick) are used as substrates for stress measurements of thin film silicon electrodes. The wafers are processed in a clean room facility where they are cleaned of organic materials and particles with a series of solvent baths (Appendix A.3) before being loaded into the deposition chamber of a physical vapor deposition (PVD) system.

A 25 nm thick film of titanium (Ti) followed by 100 nm of copper (Cu) is deposited onto the "front" side of the wafer using e-beam PVD (Kurt J. Lesker, Lab-18) at a rate of 0.7 Å/s. The Cu layer provides uniform current distribution to the silicon film and contact area for the leads while the Ti layer improves adhesion between the wafer and the copper layer. A 100 nm film of Cu is deposited on the "back" side of the substrate to provide a reflective surface for MOS curvature measurements.

A circular shadow mask (d_{Si} = 47 mm) is placed over the wafers during silicon deposition to allow for contact points for the electrical leads and set a consistent surface area (A_f) for the electrode (Figure 2.4). Amorphous silicon films are deposited onto the front copper layer via RF magnetron sputtering (Kurt J. Lesker Lab18, 2" p-doped 99.999% Si target) at 180 W and working pressure of 2 mTorr of UHP argon for a deposition rate of ∼0.7 Å/s. A quartz crystal microbalance (QCM) in the deposition chamber monitors the thicknesses of the deposited films which are later verified with a surface profilometer (Dektak3) and white-light interferometer (Zygo NewView 6000). The thickness of the substrate is measured to within 0.001 mm accuracy with a high precision Mitutoyo dial micrometer.

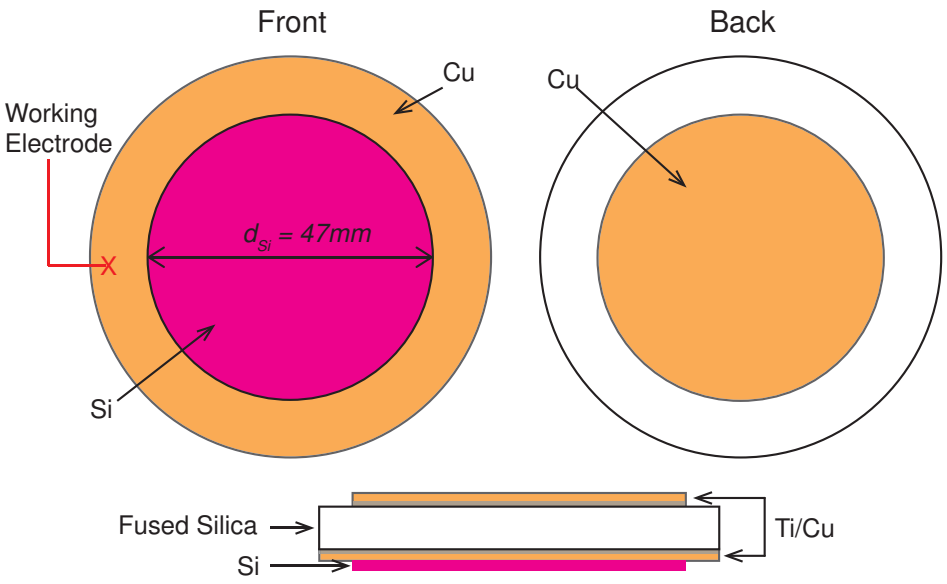

Figure 2.4: Schematic of thin film silicon electrode sample on fused silica wafer substrate.

2.3.2 Electrochemical Beaker Cell

Cell assembly and experiments are conducted in an environmental chamber (Labmaster SP, MBraun Inc.) in ultra-high purity (UHP) argon atmosphere with oxygen and moisture levels below 0.1 ppm. Custom PTFE (i.e., Teflon) beaker cells with built-in laser grade windows ($\lambda/4$ N-BK7, uncoated) are used to cycle the silicon electrode while allowing for *in situ* MOS curvature measurements (Figure 2.5). A disc of lithium metal at the bottom of each cell (60 mm diameter, 1 mm thick) functions as the counter and reference electrode. The lithium metal is weighted down by a stainless steel ring around its circumference to keep it in place. A layer of woven polymer film (Celgard 2300) is placed on top of the Li metal and fully saturated with ~10 mL of liquid electrolyte. The polymer film (also called a "separator") provides electrical insulation while allowing for ionic movement between the two electrodes via electrolyte. The electrolyte is a commercially available solution of 1.2 M $LiPF_6$ in 2:1 ethylene carbonate:diethyl carbonate by volume (BASF Selectilyte Series A6).

A thin wire of high purity copper is connected to the wafer sample at the exposed contact area (Figure 2.4) and secured onto the edge of the wafer with a small clip

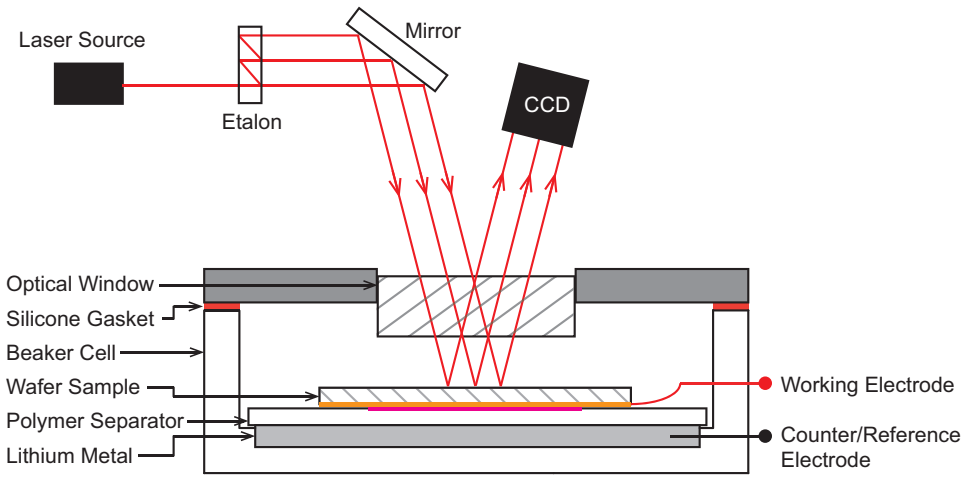

Figure 2.5: Schematic of the custom PTFE beaker cell for MOS measurements. The Si thin film electrode is cycled with Li metal, which acts as the counter and reference electrode. A laser-grade optical window allows for *in situ* MOS curvature measurements during cycling.

that was wire cut from a 1/16" sheet of low-oxygen copper. Another copper wire is secured to the lithium metal as the lead for the counter/reference electrode. Each wire is fed through the wall of the beaker cell via tapped holes, which are then sealed with stainless steel screws. Since the PTFE is relatively compliant, the tapping processes results in a hole smaller than the tap, resulting in a tight seal around the screw. As such, only a few turns of the screws are necessary for a sufficient seal; excessive turns run the risk of pinching off the copper wire and losing electrical contact. The screws also function as contact points for external leads to the potentiostat using alligator clips. The wafer sample is then placed silicon-side down onto the separator film and air bubbles trapped between the wafer and lithium metal are removed before completing assembly.

2.3.3 Electrochemical Measurements

A Solartron Analytical 1470E multichannel potentiostat (AMETEK, Inc.) running MultiStat software (Scribner Associates, Inc.) is used to conduct electrochemical

measurements. Electrical leads from the beaker cell are connected to one channel of the potentiostat via BNC feedthroughs that utilize KF-40 ports built into the glove box walls.

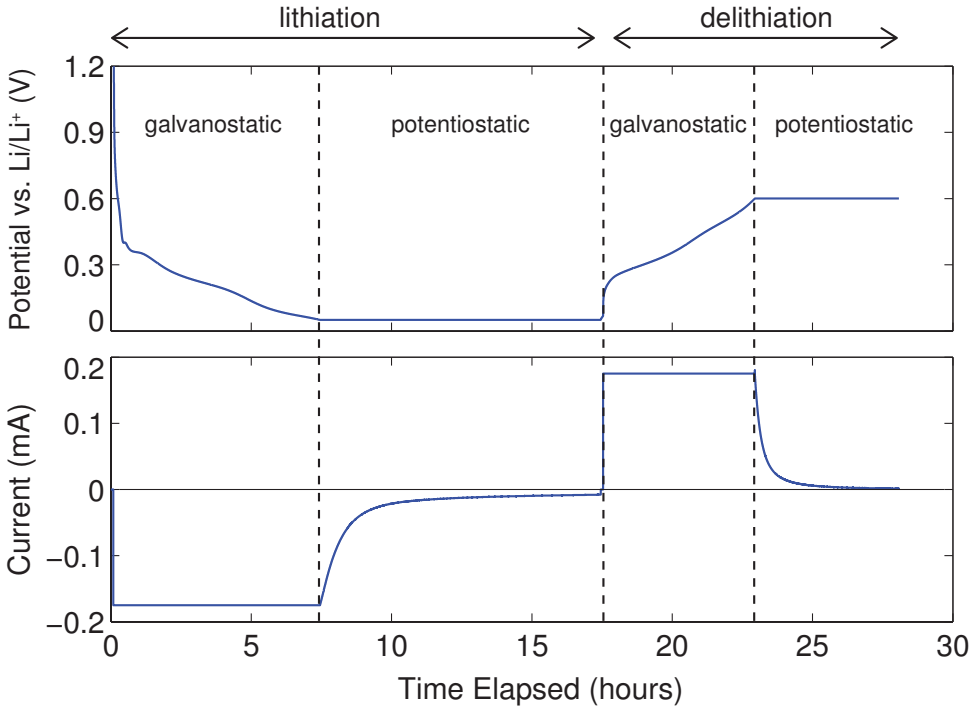

Figure 2.6: Cell potential and applied current of a Li-Si half-cell using the CCCP cycling protocol. As the Li concentration in the Si electrode increases with further lithiation, the relative composition of the electrode to the counter electrode (Li metal) and its electrochemical potential decreases. The process is reversed during delithiation.

Once the cell is assembled and the leads are connected to the potentiostat, it is cycled using the constant current constant potential (CCCP) protocol at a data acquisition rate of 1 point/sec (Figure 2.6). The cycling current is set to 175 µA, corresponding to a current density of ∼10 µA/cm^2. The equivalent charge rage is C/5 – i.e., it takes 5 hours to fully charge or discharge the electrode at constant current. Based on reported values for the diffusivity of Li in Si that range from 10^{-12} to 10^{-16} cm^2/s [69–73], the characteristic time for diffusion through the film thickness of 200 nm is no more than a minute. Since each lithiation and delithiation portion of the experiment is conducted over several hours, it is reasonable to assume that the

Li concentration is uniform throughout the film thickness.

The upper and lower cutoff potentials are set at 0.6 V and 0.05 V vs. Li/Li^+, respectively, followed by a constant voltage hold at the each cutoff potential (Table 2.1). The constant voltage (or "potentiostatic") step minimizes concentration gradients within the electrode before reversing the polarity of the current in the subsequent half-cycle. The lower limit of 0.05 V vs. Li/Li^+ is chosen to avoid the formation of crystalline $Li_{15}Si_4$ phase, which is thought to form below 0.03 V and contribute additional cyclic inefficiencies [74]. The open-circuit potential (OCP) steps measure the cell potential in the absence of current; the input impedance is 12 GΩ and the current is negligible.

Table 2.1: Constant current, constant potential (CCCP) cycling protocol. The lithiation half-cycle consist of steps 1–3 and the delithiation half-cycle consist of steps 4–6. One full electrochemical cycle consist of steps 1–6. Typically, any experiment finishes with an OCP step lasting 300 sec.

Step	Value	Notes
1. OCP	300 sec	
2. Galvanostatic (Constant current)	-175 µA	Lithiation of Si electrode
3. Potentiostatic (Constant potential)	0.05 V	
4. OCP	300 sec	
5. Galvanostatic	175 µA	Delithiation of Si electrode
6. Potentiostatic	0.6 V	

2.3.4 Substrate Curvature Measurements

Substrate curvature is monitored with a commercial MOS wafer curvature system (kSA-MOS, k-Space Associates, Inc.) using a 2x2 array of laser spots to measure curvature change in two orthogonal directions (Figure 2.7), where d_H and d_V are the horizontal and vertical distances between the laser spots, respectively.

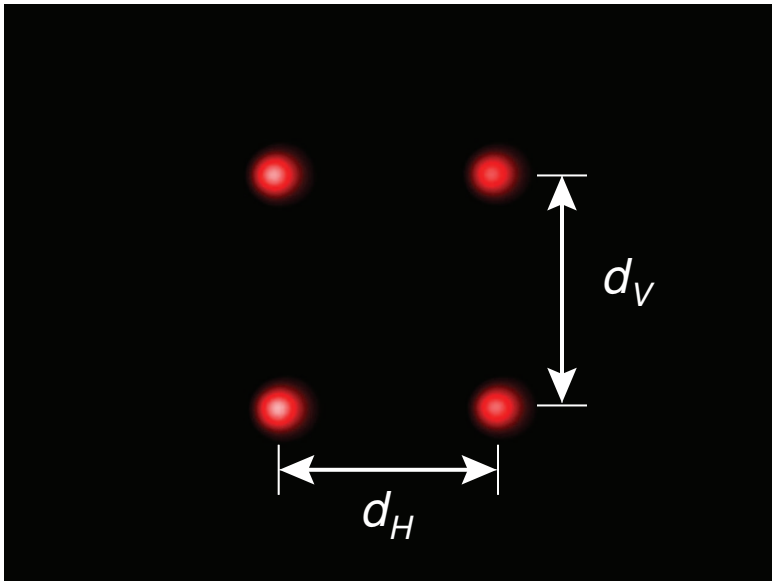

Figure 2.7: Screen capture of laser array from MOS CCD camera. d_H and d_V are the horizontal and vertical distances between the laser spots, respectively.

Since these wafer substrates may not be perfectly flat to begin with and incur some curvature during the deposition of Ti and Cu films, the curvature of each substrate is recorded prior to silicon deposition. The residual stress in the silicon film due to sputter deposition is then,

$$\sigma_r = \frac{E_s {h_s}^2}{6(1-\nu_s){h_f}^0}(\kappa^r - \kappa^0) \tag{2.5}$$

where κ^0 and κ^r are the substrate curvatures before and after silicon film deposition, respectively, and ${h_f}^0$ is the initial thickness of the deposited silicon film. The stress in the film is then,

$$\sigma_f = \sigma_r + \frac{E_s {h_s}^2}{6(1-\nu_s)h_f}\Delta\kappa_s \tag{2.6}$$

The film thickness (h_f) is a function of Li composition and is expressed as,

$$h_f = {h_f}^0(1 + 2.7z) \tag{2.7}$$

where z ranges from 0 to 1 and is known as the state of charge (SOC). A SOC of $z = 0$

corresponds to pure silicon and $z = 1$ corresponds to $Li_{15}Si_4$. This expression takes into account the volumetric strain corresponding to the maximum possible capacity of 3579 mAh/g at $Li_{3.75}Si$ for the lithiated-silicon system [13, 75], and assumes one-dimensional volume expansion – i.e., only the height of the thin-film electrode changes upon lithiation/delithiation. This is a reasonable assumption given that the film is constrained by the substrate, preventing its expansion in the radial direction and is supported with experimental observations using in situ AFM scans of patterned silicon films by Beaulieu *et al.* [68]

Once the cell is assembled, the vertical and horizontal displacements of the laser spots (as a function of time) are recorded during all the electrochemical experiments on the silicon film at an acquisition rate of 1 Hz.

2.4 Results

2.4.1 Stress-thickness and Cell Potential

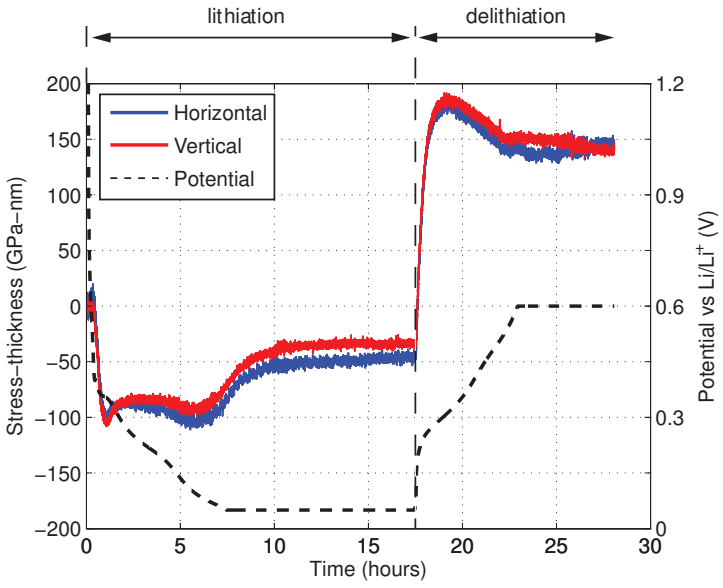

Figure 2.8: Cell potential and stress-thickness ($\sigma_f h_f$) vs. elapsed time during initial lithiation and delithiation.

Figure 2.8 shows the cell potential and stress-thickness ($\sigma_f h_f$) during the first lithiation/delithiation cycle of the silicon electrode plotted against elapsed time. The stress-thickness is a modified form of the Stoney equation given as,

$$\sigma_f h_f = \frac{E_s {h_s}^2}{6(1-\nu_s)} \Delta\kappa_s \tag{2.8}$$

Since the substrate's elastic properties and thickness are constant, the stress-thickness is directly calculated from the substrate curvature measurements. The elastic properties of the fused quartz substrate are taken to be $E_s = 71.7$ GPa and $\nu_s = 0.17$ [76, 77]. The coinciding horizontal (blue) and vertical (red) stress-thickness measurements in Figure 2.8 show that the wafer substrate deforms as a spherical cap with uniform curvature. The small difference in measured curvatures between the two perpendicular directions could be due to variation in the deposited film thickness and the substrate thickness, or from slightly non-uniform current density across the Si surface.

The stress-thickness is a useful parameter for approximating the state of stress in the film without introducing additional measurement error from the film thickness variations. For instance, taking the initial film thickness to be 100 nm, the stress in the silicon film increases by approximately 1 GPa in compression during the early stages of lithiation and remains in a compressive state through the lithiation half-cycle. Furthermore, the rapid change in sign of the stress-thickness at the early stages of delithiation shows that the film unloads elastically, enters a state of tensile stress and remains in tension throughout the delithiation cycle.

2.4.2 Accounting for Irreversible Losses

Figure 2.9 is a plot of the cell potential and stress-thickness data from Figure 2.8 plotted against the charge of the electrode. The charge ($Q = \int I \, \mathrm{d}t$) is calculated from the

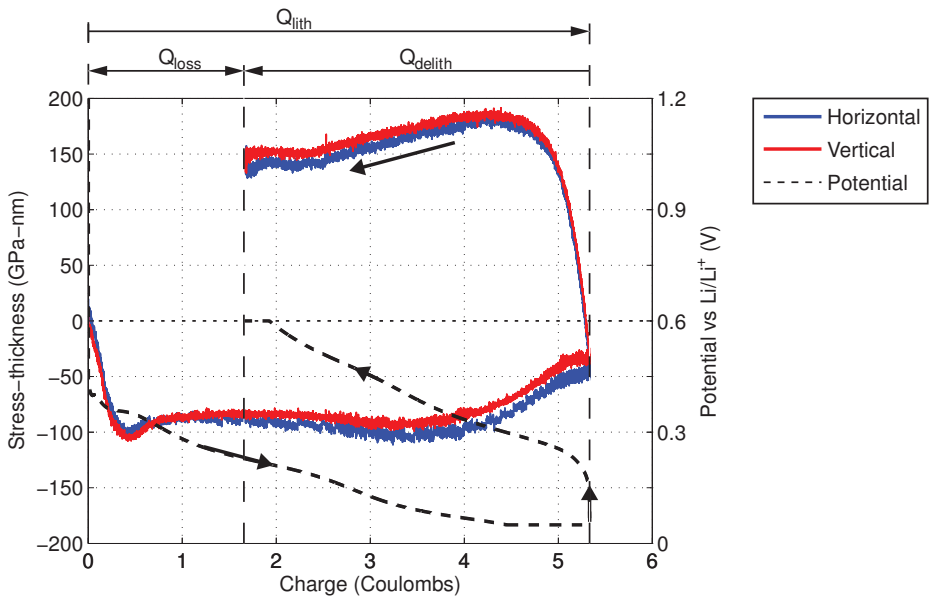

Figure 2.9: Stress-thickness and potential vs. charge ($Q = \int I\,\mathrm{d}t$) using the data from Figure 2.8. The unrecovered charge (Q_{loss}) creates uncertainty in characterizing the Li composition in the Si electrode and must be accounted for in order to report accurate values of film stress.

current measured by the potentiostat (see Figure 2.6) and not necessarily the charge held in the electrode. During the lithiation and delithiation cycle, a portion of the applied current is used to electrochemically reduce the electrolyte at the electrolyte-electrode interface to form a passivation layer on the electrode surface called the solid electrolyte interphase (SEI). SEI formation is an irreversible reaction that consumes Li-ions from the positive electrode, leading to a loss of capacity observed in the first lithiation/delithiation cycle of rechargeable lithium-ion batteries. Besides charge loss in the first cycle, continuous formation of this layer also increases resistance to Li-ion diffusion (i.e., internal impedance of a battery) [78]. It is also possible that some of the Li-ions are irreversibly bonded to the Si and are not recoverable electrochemically.

Since the volume expansion of the silicon electrode is taken to be a function of its state of charge (Equation 2.7), it is necessary to account for charge loss in order to accurately characterize the film thickness evolution and hence, the stress values in the silicone electrode. Figure 2.10 shows the cell potential and the stress-thickness of

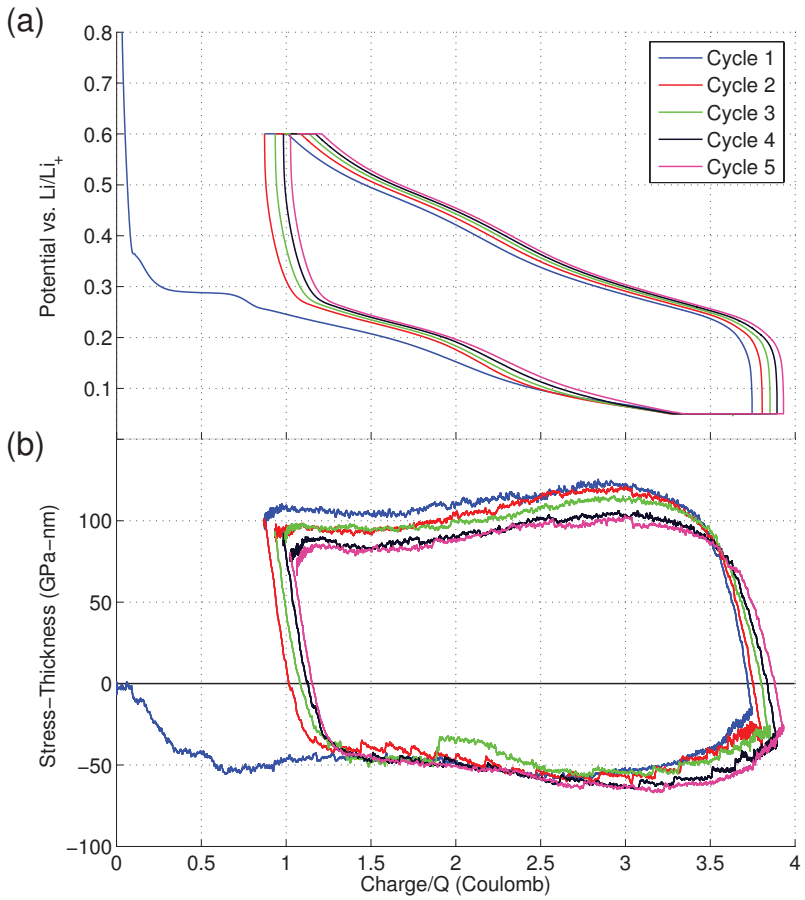

Figure 2.10: (a)Cell potential vs. charge and (b) the corresponding stress-thickness measurements following the CCCP protocol in described in Section 2.3.3. Only the first five cycles are shown for clarity. Similarly, only the horizonal curvature values are displayed in (b). The corresponding values of Q_{lith} and Q_{delith} of all seven cycles are shown in Figure 2.12.

the above TFSE sample plotted against charge during the first five cycles using the CCCP protocol described in Section 2.3.3. If Q_{lith} is the total charge transferred by the potentiostat during lithiation and Q_{delith} is the total charge during delithiation, then $Q_{loss} = Q_{lith} - Q_{delith}$ is the total charge lost in that cycle (see Figure 2.9). Figure 2.12 illustrates the corresponding Q_{loss} and cyclic efficiency of the sample in Figure 2.10, showing that Q_{loss} is significantly higher during the first cycle and that Q_{delith} is consistent across all seven cycles. A recent study on quantifying the loss due to SEI formation suggests that SEI losses occur primarily during lithiation and is not strongly influenced by the duration of the potential hold [41]. If SEI formation is taken

to be the predominant source of Q_{loss}, then Q_{delith} represents the total recoverable charge (hence, its capacity) of the silicon electrode. Taking the irreversible loss to occur at a fixed rate, the effective charge of the electrode (Q_{eff}) is modeled as,

$$Q_{eff} = \begin{cases} \left(\frac{Q_{delith}}{Q_{lith}}\right) Q, & \text{during lithiation} \\ Q, & \text{during delithiation} \end{cases} \tag{2.9}$$

where the charge at the end of a lithiation cycle coincides with the charge at the beginning of the subsequent delithiation cycle (and vice versa).

2.4.3 Stress vs. Capacity

Data presented in this section was collected subsequent to the initial lithiation-delithiation cycle of the silicon film. Although RF sputtered silicon films are amorphous in nature [38], initial lithiation of the film results in a phase transformation from a-Si to a-Li$_x$Si [79, 80]. This is akin to the phase transformation of crystalline silicon into a-Li$_x$Si during initial lithiation at room temperature [30, 81]. Given the unique behavior of the first cycle, this section will focus on the stress evolution of lithiated silicon following the initial cycle. Detailed analysis of stress evolution and characterizing Li composition during the first cycle will be discussed in Chapter 4.

Figure 2.13 shows the cell potential and the true film stress plotted against the gravimetric capacity ($C = Q/mass_{Si}$) of the silicon thin-film electrode. The mass is taken from the initial thickness ($h_f{}^0$), surface area (A_f) and density of the silicon film ($\rho = 2.32$ g/cm^3 for amorphous Si). The state of charge (z) is then,

$$z = C/C_{max} \tag{2.10}$$

where $C_{max} = 3579$ mAh/g. The stress is obtained by dividing the stress-thickness with the current value of the film thickness using Equation 2.7.

Upon lithiation, the substrate prevents the in-plane expansion of the film. This results in compressive stress in the film, which increases linearly with time (or capacity). If we assume that the strain induced by Li in Si is proportional to its concentration, then the linear increase in the compressive stress indicates elastic response. At compressive stress of about 0.7 GPa, the film appears to reach the elastic limit (which corresponds to a capacity of ∼250 mAh/g), and begins to flow with further lithiation in order to accommodate the additional volume expansion. The flow stress is seen to decrease with lithiation, reaching a value of about 0.3 GPa at a capacity of ∼2500 mAh/g at the end of lithiation. Hence, it can be concluded that the flow stress of lithiated Si decreases as the Li concentration increases.

Upon delithiation, the unloading is initially elastic; the stress reverses elastically until it becomes about 0.4 GPa in tension, where the film begins to flow in tension in order to accommodate the reduction in volume. The flow stress increases to about 0.8 GPa by the end of delithiation. Note that the stress response is similar in compression and tension. That is, at any state of charge, the flow stress in compression and tension are approximately the same. Thus, the film undergoes repeated compressive and tensile-plastic flow during successive lithiation–delithiation processes, respectively. Since plastic flow dissipates mechanical energy, during delithiation, some of the electrical work done on the half cell by the potentiostat is dissipated as plastic work in the silicon electrode. Similarly, during lithiation, some of the stored energy of the half cell is dissipated in compressive plastic flow of the electrode. Thus, in addition to other polarization losses, plastic dissipation in the Si electrode must be taken into account. The measurements shown in Figure 2.13 correspond to the third charge–discharge cycle; subsequent cycles show a very similar behavior. Since the state of stress during lithiation and delithiation is different even at an identical state of charge, all material properties that depend on stress will be different during lithiation and delithiation.

2.4.4 Mechanical Dissipation

Since lithiation of silicon results in volumetric strain proportional to the state of charge, the area enclosed by the stress-capacity curve in Figure 2.13b is analogous to the mechanical dissipation due to plasticity. To calculate this energy loss, consider the volume expansion of a piece of silicon electrode due to an incremental change in composition, Δc. If the deformation is small enough, the infinitesimal strain can be decomposed as,

$$\Delta\varepsilon_{ij} = \Delta{\varepsilon_{ij}}^{c} + \Delta{\varepsilon_{ij}}^{p} + \Delta{\varepsilon_{ij}}^{e} \tag{2.11}$$

where ${\varepsilon_{ij}}^{c}$ is the strain due to change in Li composition, ${\varepsilon_{ij}}^{p}$ is the plastic strain, and ${\varepsilon_{ij}}^{e}$ is the elastic strain. Taking the compositional strain to be isotropic,

$$\Delta{\varepsilon_{ij}}^{c} = \frac{\Delta{\varepsilon_{v}}^{c}}{3}\delta_{ij} \tag{2.12}$$

where ${\varepsilon_{v}}^{c} = \eta\Delta c$. Taking the volumetric strain to be linear with Li composition [82], the compositional strain rate $\left(\eta = \frac{\partial{\varepsilon_{v}}^{c}}{\partial c}\right)$ is constant. By symmetry, there is no net strain in the in-plane directions for a thin film bonded to a substrate ($\Delta\varepsilon_{11} = \Delta\varepsilon_{22} = 0$). If the film is already in a state of plastic yield, the change in composition results in a plastic strain that prevents in-plane expansion. Since plastic deformation is volume conserving, the incremental plastic strain tensor can be written as,

$$\Delta{\varepsilon_{ij}}^{p} = \begin{bmatrix} \frac{-\Delta{\varepsilon_{v}}^{c}}{3} & 0 & 0 \\ 0 & \frac{-\Delta{\varepsilon_{v}}^{c}}{3} & 0 \\ 0 & 0 & \frac{2}{3}\Delta{\varepsilon_{v}}^{c} \end{bmatrix} \tag{2.13}$$

The strain energy per unit volume element dissipated due to plasticity is given as,

$$\Delta w^{m} = {\sigma_{ij}}^{*}\Delta{\varepsilon_{ij}}^{p} \tag{2.14}$$

where ${\sigma_{ij}}^* = \sigma_{ij} - \frac{1}{3}\sigma_{kk}\delta_{ij}$ is the deviatoric stress tensor and is taken to be relatively constant over Δc. Since the film is under a state of equibiaxial stress ($\sigma_{11} = \sigma_{22} = \sigma_f$), the deviatoric stress tensor is given as,

$${\sigma_{ij}}^* = \begin{bmatrix} \frac{\sigma_f}{3} & 0 & 0 \\ 0 & \frac{\sigma_f}{3} & 0 \\ 0 & 0 & \frac{-2\sigma_f}{3} \end{bmatrix} \tag{2.15}$$

Thus, the incremental mechanical dissipation due to Δc is,

$${\Delta W_{lith}}^m = \frac{2}{3}\sigma_f \left(\frac{\partial {\varepsilon_v}^c}{\partial c} \right) V_f \Delta c \tag{2.16}$$

where $V_f = A_f h_f$ is the total volume of the thin film electrode. Since the film is constrained in the in-plane direction, A_f is taken to be constant. Integrating Equation 2.16 over the range of compositions exhibiting plastic flow ($c = c^p$), the total mechanical dissipation due to plasticity during lithiation is,

$${W_{lith}}^m = \frac{2}{3} A_f \eta \int_{c=c^p} \sigma_f h_f \, \mathrm{d}c \tag{2.17}$$

which is illustrated as the area highlighted in the plot of $\sigma_f h_f$ vs. c below (Figure 2.14).

In order to compare ${W_{lith}}^m$ with other polarization losses, consider the following energy balance during lithiation,

$$W^{electrode} = {W_{lith}}^c + {W_{lith}}^p + {W_{lith}}^m \tag{2.18}$$

where $W^{electrode}$ is the available energy in the half-cell, ${W_{lith}}^c$ is the work done by the cell on the potentiostat, ${W_{lith}}^m$ is the mechanical dissipation in the Si electrode during compressive plastic flow, and ${W_{lith}}^p$ is the sum of all other sources of dissipation due to various polarization losses (i.e., kinetic, ohmic and transport). The first quantity,

${W_{lith}}^c$ is given by,

$$ {W_{lith}}^c = \int_{t=t_{lith}} IV \, \mathrm{d}t \tag{2.19} $$

where t_{lith} is the time interval during lithiation, V is the cell potential (voltage), and I is the current at which lithiation is carried out. Recognizing that $I \, \mathrm{d}t = \mathrm{d}Q$ where $\mathrm{d}Q$ is the incremental change in charge and Q_{lith} is the total charge outputted by the potentiostat,

$$ {W_{lith}}^c = \int_{Q=Q_{lith}} V \, \mathrm{d}Q \tag{2.20} $$

is simply the area under the V vs. Q curve during lithiation (Figure 2.11a).

Similarly, the energy balance during delithiation for which the work done by the potentiostat on the cell (${W_{delith}}^c$) is given by,

$$ {W_{delith}}^c = W^{electrode} + {W_{delith}}^m + {W_{delith}}^p \tag{2.21} $$

where all terms in the above equation stand for the same quantities as in Equation 2.18, except that the subscript "delith" now stands for delithiation. Eliminating $W^{electrode}$ between Equations 2.18 and 2.21 gives the energy loss for once charge/discharge cycle of the Li-Si half-cell,

$$ {W_{lith}}^c - {W_{delith}}^c = {W_{lith}}^m + {W_{delith}}^m + {W_{lith}}^p + {W_{delith}}^p \tag{2.22} $$

The left hand side of Equation 2.22 is the area enclosed by the *Potential vs. Charge* curve, which is analogous to the *Potential vs. Capacity* curve in Figure 2.13a. The quantity $W^m = {W_{lith}}^m + {W_{delith}}^m$ is the total mechanical energy dissipation due to plasticity as described by Equation 2.17. Evaluation of the quantities in Equation 2.22 from the experimental data shows that the mechanical dissipation in a Si thin film electrode is approximately 45% of the total energy dissipation, which is a significant fraction and is comparable to the polarization losses elsewhere in the cell (Table 2.2).

The observation that plastic deformation contributes significantly to the total

Table 2.2: Breakdown of sources of energy loss. Mechanical dissipation via plasticity (W^m) accounts for about 45% of the total work done by the Li-Si half-cell. Units are in J.

Cycle	ΔW^c	${W_{lith}}^m$	${W_{lith}}^m$	${W_{total}}^m$
2	1.004730	0.206436	0.248045	0.454
3	1.046133	0.210088	0.248962	0.459
4	1.058353	0.200429	0.257331	0.458
5	1.038175	0.189955	0.263220	0.453
6	0.997933	0.179101	0.263364	0.442
7	0.949565	0.170771	0.268875	0.440

energy dissipation during an electrochemical cycle in a TFSE half-cell is a new insight from the experiments and analysis presented here. However, to place it in proper perspective, it should be noted that a typical full cell battery operates at a potential of ∼4 V vs. the cathode. Therefore, a potential hysteresis of ∼0.2 V due to stress (i.e., plastic deformation) accounts for approximately 5% of the total energy dissipation. This is still a non-trivial contribution and it must be properly accounted for for an accurate thermal analysis of the battery and battery packs.

2.4.5 Biaxial Modulus of Lithiated Silicon

The variation of the silicon anode's yield stress with Li composition suggests that its material properties may be evolving with Li composition. Additionally, there is an observed difference in the slope of the elastic unloading at low and high concentrations of Li (red lines in Figure 2.14), which suggests a change in the elastic modulus between the two states of charge. Since the number of Li atoms is over 3.5 times that of the Si atoms at full lithiation, it is reasonable to expect significant changes in mechanical properties with SOC. However, little data is available in literature on the mechanical properties of lithiated silicon. In this section, we present an experimental effort to

directly measure the biaxial modulus of silicon thin-film electrode as a function of lithium concentration.

Recall the linear decomposition of the strain within the lithiated silicon film in Equation 2.11. If the film is delithiated incrementally from a state of plastic yield, then it unloads elastically such that there is no plastic strain (${\varepsilon_{ij}}^p = 0$). The elastic strain due to a change in the equibiaxial stress in the film ($\Delta\sigma_f$) is then,

$$ {\varepsilon_{ij}}^p = \frac{\Delta\sigma_f}{M_f} \tag{2.23} $$

where $M_f = \frac{E_f}{1-\nu_f}$ is the biaxial modulus of the film. A change in composition induces a volumetric strain following Equation 2.7, which can also be written as,

$$ {\varepsilon_{ij}}^c = (1 + 2.7z)^{1/3} - 1 \tag{2.24} $$

In the case of a thin film, the in-plane components of the left hand side of Equation 2.11 are zero due to substrate constraints and the biaxial modulus can be written as,

$$ M_f = -\Delta\sigma_f / \Delta{\varepsilon_{ij}}^c \tag{2.25} $$

Thus, by making incremental changes to the film composition at various SOCs and measuring the corresponding change in film stress, the biaxial modulus of the film can be measured experimentally. It was shown earlier that the Li–Si electrodes undergo cycles of compressive and tensile stress during lithiation and delithiation, respectively, in Section 2.4.3. Since full delithiation can result in large tensile stresses and film cracking, the elastic constants are best measured during the first lithiation half-cycle when the stress is known to be compressive and cracks do not form in a thin film configuration. A representative history of current density, potential and stress showing a fraction of a long sequence SOC perturbation cycles) is plotted in Figure 2.15(a)–(c).

The stress–strain data in the elastic unloading region was used to estimate the

biaxial modulus of the Li–Si system. Note the rapid stress relaxation immediately after the current interrupted, possibly due to double layer discharge. Ideally, the stress should reach a steady state during the open-circuit step before delithiation commences so that viscoplastic stress relaxation does not contribute to the stress drop. However in the Li–Si system, side reactions slowly and continuously remove Li from Si, resulting in a corresponding continuous change in stress. Hence the stress does not reach a steady-state value even after days [38]. In this investigation, we assume that one hour of open-circuit relaxation is sufficient to minimize the contribution of viscoplastic relaxation to the stress drop during delithiation.

The biaxial moduli of Li–Si calculated from the data set shown in Figure 2.15b–c, and the results are shown in Figure 2.16. The experiments reveal that the biaxial modulus decreases significantly, from 65 GPa at $Li_{0.4}Si$ to about 30 GPa at $Li_{3.5}Si$. Recent *ab initio* molecular dynamics (AIMD) simulations by Shenoy *et al.* of the amorphous Li-Si system observe that the elastic constants follow the rule of mixtures to a reasonable extent [83]. If x is the stoichiometric ratio of Li to Si atoms, $\chi_{Li} = \frac{x}{x+1}$ is the Li fraction of the Li_xSi film and $\chi_{Si} = 1 - \chi_{Li}$ is the Si fraction, then the estimated biaxial moduli of silicon electrode (M_{est}) following the rule of mixtures is,

$$M_{est} = \frac{\chi_{Li}E_{Li} + \chi_{Si}E_{Si}}{1 - (\chi_{Li}\nu_{Li} + \chi_{Si}\nu_{Si})} \tag{2.26}$$

Figure 2.16 shows that our experimental values agree reasonably well with the rule of mixtures for the Li-Si system, particularly at higher Li content.

If the reduction in elastic moduli is any indication of increased ductility due to alloying, significant changes in other mechanical properties – such as fracture energy – can be expected as well. Hence, it becomes essential to consider the change in material properties while modeling stress evolution and mechanical damage in Si anodes.

2.5 Conclusions and Future work

We have demonstrated the use of the multi-beam optical sensor (MOS) technique to measure stress evolution in a silicon thin film electrode during lithiation and delithiation. Stress evolution upon electrochemical cycling reveals that the Si electrode undergoes repeated cycles of compressive- and tensile-plastic flow, dissipating mechanical energy. The stress evolution data enables estimation of the mechanical dissipation, which was found to be comparable to the polarization losses elsewhere in the cell. An *in situ* method is used to measure the change in the biaxial modulus of Si anodes as a function of Li concentration. It involves perturbing the SOC of the anode through a small delithiation–relithiation cycle, while measuring the change in film stress with a MOS wafer curvature system. The measurements show that the biaxial modulus drops substantially from ∼65 GPa for $Li_{0.4}Si$ to ∼30 GPa for $Li_{3.5}Si$. A simple rule of mixtures was seen to agree well with the measurements. Therefore, it may be reasonable to expect that other relevant mechanical properties (e.g., ductility and fracture toughness) would also change substantially. These observations have implications for realistic modeling of the mechanics of Si anodes to predict their cycle life.

The results also suggest that stress contributes significantly to the chemical potential of lithiated silicon. Further experiments aimed at understanding the influence of the mechanical stresses on the equilibrium potential of the lithiated-silicon are currently ongoing in our laboratory. Such experiments are expected to provide insights to understand the potential hysteresis, suggests ways to reduce hysteresis, which can increase the energy efficiency of the cell. An additional consequence of the above analysis is that the contribution of stress to the chemical potential of lithiated silicon is significant and should be taken into account.

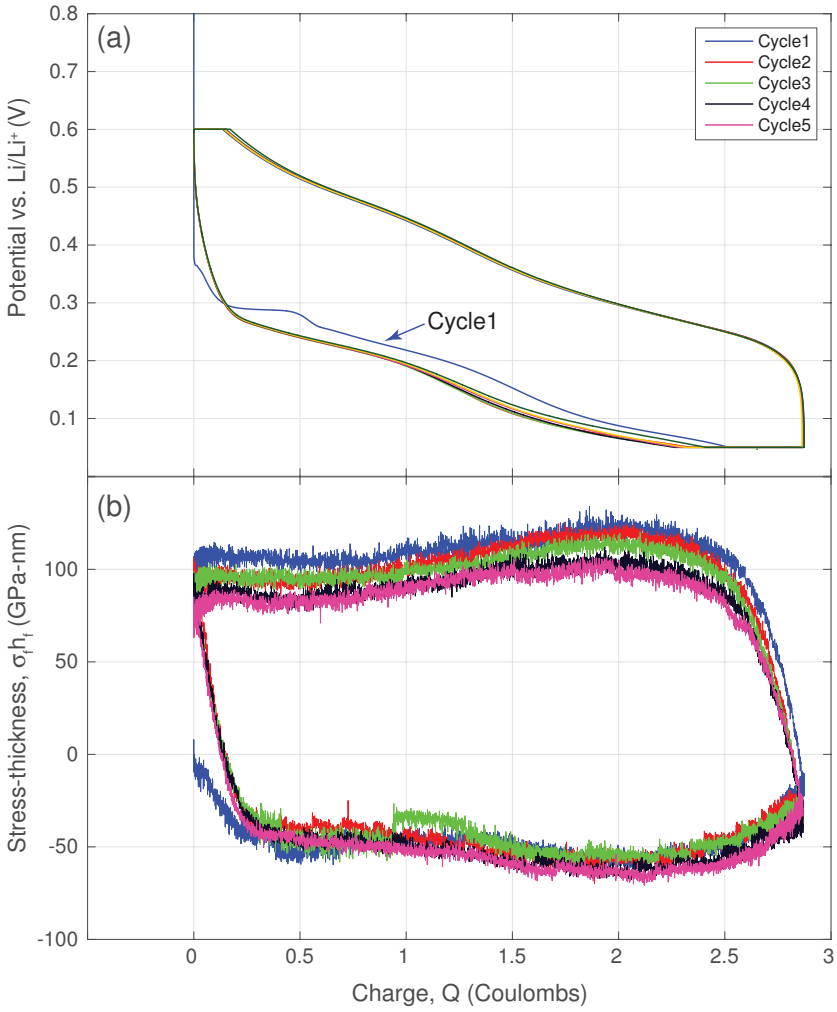

Figure 2.11: Cell potential and stress-thickness from Figure 2.10 plotted against Q_{eff} showing consistent cycle behavior in cycles 2–5. The deviation of the potential curve during Cycle1 suggests additional mechanisms may contribute to Q_{loss} during first cycle lithiation.

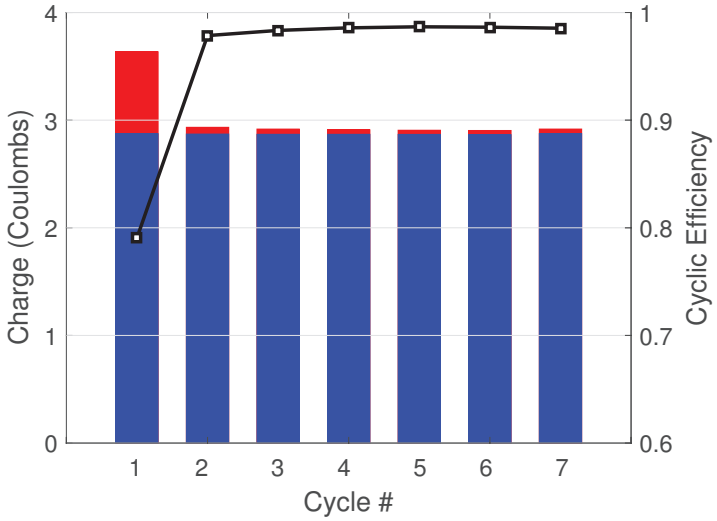

Figure 2.12: (a)Cell potential vs. charge and (b) the corresponding stress-thickness measurements following the CCCP protocol in described in Section 2.3.3. Only the first five cycles are shown for clarity. Similarly, only the horizonal curvature values are displayed in (b). The corresponding values of Q_{lith} and Q_{delith} of all seven cycles are shown in Figure 2.12.

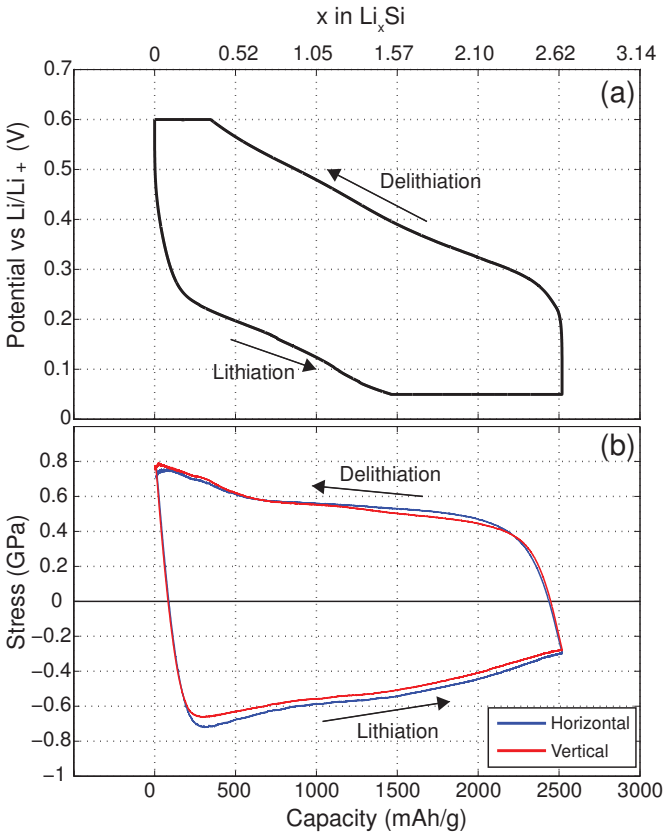

Figure 2.13: (a) Cell potential vs. capacity during one electrochemical cycle of a Si thin-film electrode cycled at C/5 rate between 0.6 and 0.05 V vs. Li/Li$^+$ and (b) the corresponding stress calculated from the substrate curvature data using the Stoney equation. The equivalent Li composition (x) is shown in the upper x-axis. The blue and red curves correspond to the stresses calculated from the averaged horizontal and the vertical displacement of the spots, respectively. The arrows in both figures indicate cycling direction.

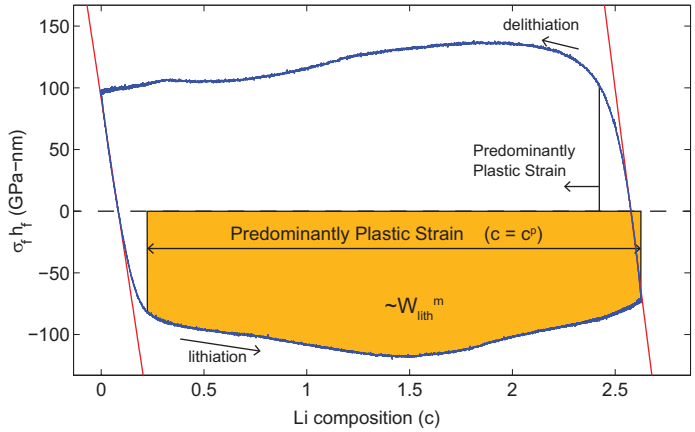

Figure 2.14: Plot of stress-thickness with Li composition (x in Li_xSi) during the third lithiation/delithiation cycle of a thin film silicon eletrode.

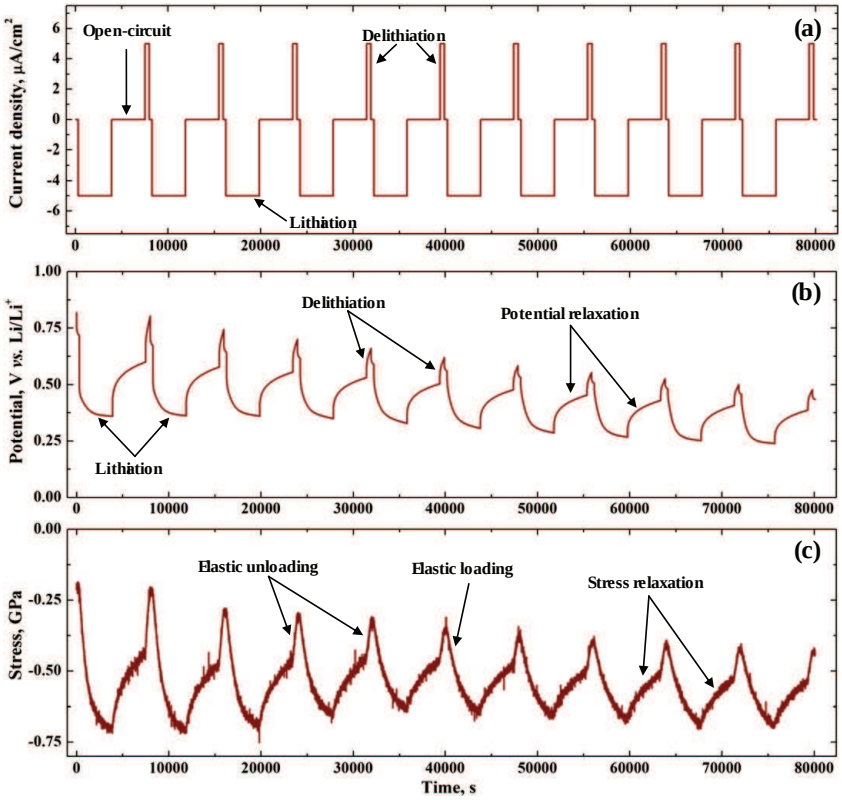

Figure 2.15: Representative plot of (a) current–density, (b) cell potential and (c) stress evolution obtained *in situ* from the experiments designed to measure biaxial moduli (M_f) of a lithiated-silicon electrode.

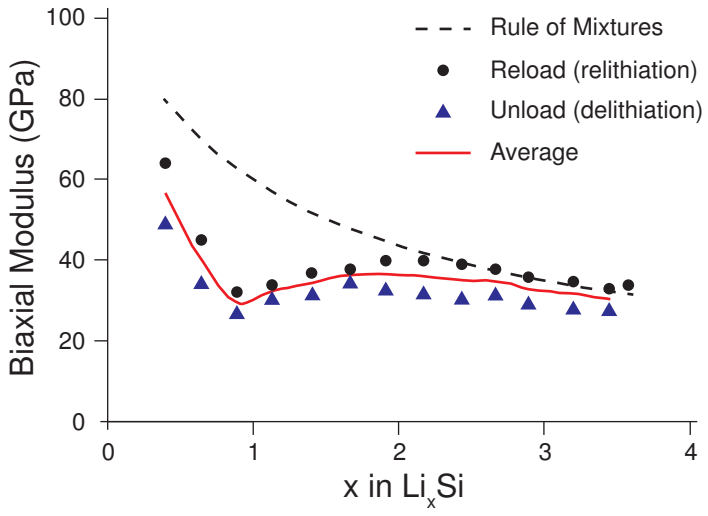

Figure 2.16: Variation of biaxial modulus as a function of lithium concentration (or SOC) along with a comparison from the data obtained through rule of mixtures. The biaxial modulus of Li_xSi decreases significantly with the lithium concentration, from 64 GPa at negligible lithium concentration to approximately 30 GPa for $Li_{3.5}Si$. The rule of mixtures agrees to experimental values more accurately at higher values of lithium concentration (i.e., $x > 1.8$). The discrepancy between the experimental data and the data from the rule of mixtures between $x = 0.6$ and $x = 1.8$ is attributed to the uncertainties associated with the SEI formation.

Chapter 3

Stress Potential Coupling

3.1 Introduction

The electrochemical lithiation and delithiation of silicon has been extensively studied in a multitude of anode architectures such as nano-wires [16–20], amorphous thin films [15, 28, 29, 31, 32], crystalline thin films [33], and composites made with crystalline silicon particles and powders [22–26, 75, 81, 84]. Yet regardless of the geometry studied, the electrochemical potential vs. Li/Li^+ of these silicon anodes at a given state of charge (SOC) during lithiation is considerably lower than its potential at that same SOC during delithiation (Figure 3.1). Data from literature shows that the difference between the lithiation and delithiation potentials at a given SOC — defined here as the "potential offset" — exists irrespective of anode architecture or characteristic size, with values ranging from 250–320 mV [14–16, 38, 45, 47–49, 74, 84, 85].

There are several kinetic effects that are known to contribute to the offset, most of which occur at the electrode/electrolyte interface and are consequences of extracting current across the electrode. For example, there exists an overpotential ($\eta' = E_{measured} - E_{actual}$) required to drive a reversible electrochemical reaction forward (or backwards) and generate a current (I) from the electrode. The relationship between the current density ($i = I/A_{electrode}$) and η' is given by the Butler-Volmer

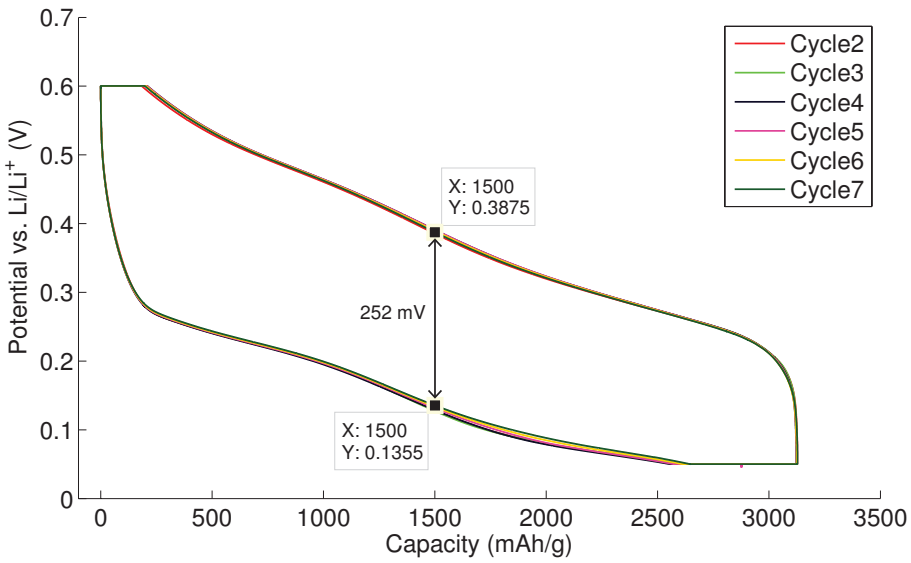

Figure 3.1: Plot of Cell Potential vs. Specific Capacity of a thin film silicon electrode illustrating the potential offset.

equation,

$$i = i_0 \left[\exp\left\{ \left(\frac{nF\,(1-\beta)}{RT} \eta' \right) \right\} - \exp\left\{ \left(\frac{-nF\beta}{RT} \eta' \right) \right\} \right] \tag{3.1}$$

where $i_0 = nF(k_f C_O)^{1-\beta}(k_b C_R)^{\beta}$ is the "exchange current". n is the number of electrons involved in the reaction, F is the Faraday constant, R is the universal gas constant, T is the absolute temperature (in K), k_f and k_b are the reaction constants of the forward and backward reactions, C_O and C_R are the concentrations of the the oxidizer and reducer, respectively, and $0 < \beta < 1$ is a measure of the symmetry of the reaction. β is typically taken to be 0.5 [40]. The relationship between the overpotential and current density is plotted schematically in Figure 3.2. Since electrochemical cycling requires some non-trivial current, Equation 3.1 reveals that there will always be some finite η' that shifts the measured potential as to increase the potential offset.

As a consequence of this potential offset, the silicon electrode exhibits a hysteresis loop during a lithiation/delithiation cycle. The area enclosed by the hysteresis loop represents the total energy dissipated by the cell during the cycle (i.e., the net work done by the potentiostat controlling the cell potential and current). Hence, the potential offset is indicative of the energy efficiency of the battery.

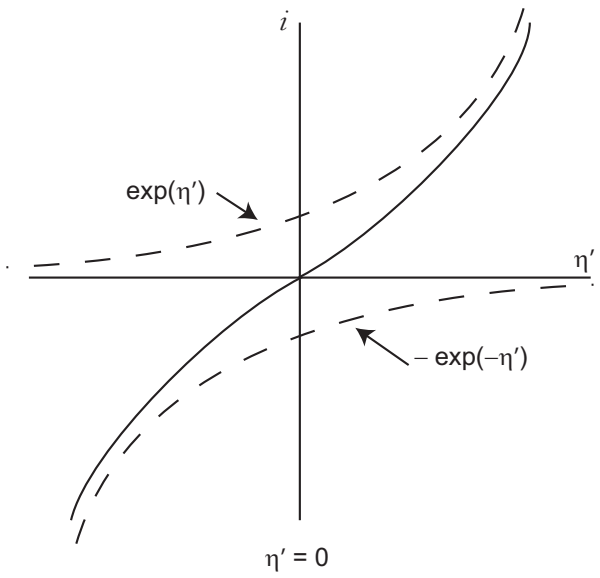

Figure 3.2: Illustration of the Butler-Volmer equation relating the electrode current (i) to applied overpotential η'. At sufficiently high overpotentials, the electrode operates in the Tafel regime and η' is not strongly influenced by i.

Traditionally, energy dissipation is thought to occur at the electrode-electrolyte interface due to the overpotential and IR losses (i.e., heat dissipation) elsewhere in the battery. However, it is demonstrated in Section 2.4.4 that the mechanical energy dissipation of a thin film silicon electrode due to plasticity accounted for 45% of the total energy loss of that cycle. It can be argued that in the absence of stress, there would be no plastic deformation and the area enclosed by the hysteresis loop in Figure 3.1 would be smaller. This suggests that in addition to contributions to the potential offset due to kinetic phenomena, there exists a relationship between the cell potential and its state of stress. Indeed, from an energetic standpoint, it is reasonable to believe that the presence of stress changes the total free energy of an electrode and would change the work required to insert an additional Li atom into a stressed host structure. The purpose of this chapter is to quantify the contribution of stress to the potential offset, known as the stress-potential coupling, using a thermodynamic model and to verify this model with experiments. The treatment here follows that described in Sethuraman *et al.* [35] and Sheldon *et al.* [47].

3.2 Potential of a Silicon Electrode

The silicon thin films used in this study are fabricated using RF magnetron sputter deposition, resulting in amorphous or nanocrystalline films. *In situ* x-ray diffraction (XRD) studies at room temperature [74, 81] and TEM observations [79, 80] show that amorphous silicon remains amorphous as it is lithiated for the first time and expands uniformly with lithium concentration. It has been shown that room temperature electrochemical lithiation of Si results in an amorphous Li_xSi (a-Li_xSi) phase, but transforms into crystalline $Li_{3.75}Si$ below a potential of about 30 mV. However, if the lithiation potential is maintained above 50 mV, the lithiated silicon film is expected to stay amorphous [74]. Based on these observations, it is assumed that the lithiated silicon electrode behaves as an amorphous solid solution whose solute (Li) concentration varies during electrochemical cycling, provided that the potential stays above 50 mV. Using these assumptions, we begin with the Larche-Cahn analysis of thermochemical equilibrium of a solid solution under stress to describe the effect of mechanical stress on the equilibrium potential of an electrochemical cell [86–89].

3.2.1 Equilibrium Chemical Potential of Lithium in Silicon

The linear form of the Larche-Cahn thermodynamic model [86] incorporates the effects of mechanical stress to the chemical equilibrium of a solid solution. The model assumes that the energy density (u') of the solid solution is a single valued function of entropy density (s') and other state variables,

$$u' = u'(\varepsilon_{ij}, s', \rho_i', ..., \rho_N') \tag{3.2}$$

where ε_{ij} is the strain tensor, ρ_i' is the molar density of component i per unit volume of the reference configuration, and N is the number of components in the system. In the special case of a binary interstitial solution ($N = 2$), the differential of the energy

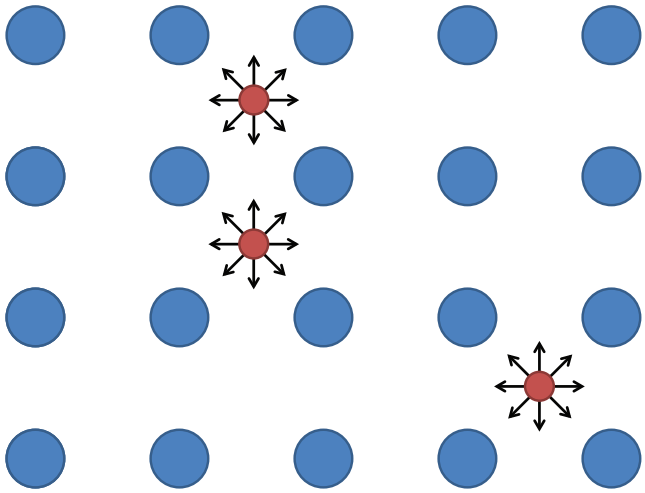

Figure 3.3: Illustration of an interstitial solid solution. The presence of the solute (small, red atoms) induces a displacement in the network (large, blue atoms), resulting in a strain due to solute concentration (ε^c).

density can be represented as,

$$\mathrm{d}u' = \sigma_{ij}\,\mathrm{d}\varepsilon_{ij} + \theta\,\mathrm{d}s' + {\rho_0}'\mu\,\mathrm{d}c \tag{3.3}$$

where $\sigma_{ij} = \frac{\partial u'}{\partial \varepsilon_{ij}}$ is the Cauchy stress tensor and $\theta = \frac{\partial u'}{\partial s'}$ is the temperature, taken to be constant in the current treatment. The chemical potential (μ) of the solute in the solution for a binary interstitial solution is given as,

$$\mu = \left(\frac{\partial u'}{\partial c}\right)_{s',\varepsilon} = \left(\frac{\partial u'}{\partial {\rho_1}'}\right)_{{\rho_2}',s',\varepsilon} - \left(\frac{\partial u'}{\partial {\rho_2}'}\right)_{{\rho_1}',s',\varepsilon} \tag{3.4}$$

The solute (Li) is free to move within the bulk (Si) and ρ_{Li} is taken to be constant throughout the volume. ${\rho_0}'$ is the total number of bulk atoms per unit volume in the reference configuration, which is taken to be constant. The composition ($c = \rho_{Li}/{\rho_0}'$) is the ratio of solute (Li) atoms to the Si atoms.

In the case of small strains, it is assumed that the collective effects of alloying and mechanical loads are small enough that additive decomposition of the strain tensor ($\varepsilon_{ij} = {\varepsilon_{ij}}^e + {\varepsilon_{ij}}^c$) is valid. Following the conventions established in Section 2.4.4, ${\varepsilon_{ij}}^c$

is the elastic strain due to a change in composition of the silicon and assumed to be isotropic. ${\varepsilon_{ij}}^{e}$ is the elastic strain due to an applied load (σ_{ij}) given by,

$$ {\varepsilon_{ij}}^{e} = S_{ijkl}\sigma_{kl} \tag{3.5} $$

S_{ijkl} is the compliance tensor, which is taken to be a function of composition only. The following Maxwell relation can be derived from Equation 3.3 by differentiating $u' - \sigma_{ij}\varepsilon_{ij}$ twice with respect to c and σ_{ij} [86]:

$$ \left(\frac{\partial \varepsilon_{ij}}{\partial c}\right)_{\sigma_{kl},\theta} = -{\rho_0}' \left(\frac{\partial \mu}{\partial \sigma_{ij}}\right)_{c,\theta,\sigma_{kl\neq ij}} \tag{3.6} $$

Combining Equation 3.5 with Equation 3.6, the linear form of the differential of the chemical potential due to a change in stress state at a constant composition is then,

$$ {\rho_0}' \, \mathrm{d}\mu = -\frac{\partial {\varepsilon_{ij}}^{c}}{\partial c} \, \mathrm{d}\sigma_{ij} - \left(\frac{\partial S_{ijkl}}{\partial c}\sigma_{kl}\right) \mathrm{d}\sigma_{ij} \tag{3.7} $$

However, volumetric strains in Si electrodes can reach as high as 270%, with extensive plasticity at the stresses observed during electrochemical cycling that clearly violate the assumptions made in the linear (small strain) theory. Nonlinear forms of the equilibrium chemical potential exist that can account for these finite strains [40, 87]. Before we proceed to implement the nonlinear theory, however, let us first examine the relative magnitudes of the two stress terms in Equation 3.7.

Since the lithiated silicon remains amorphous during cycling, it is assumed that its elastic properties are isotropic and its compliance tensor, S_{ijkl}, can be described in terms of the elastic modulus E and the Poisson's ratio ν of the film,

$$ S_{ijkl} = \frac{1+\nu}{E}\left(\delta_{il}\delta_{jk} + \delta_{ik}\delta_{jl}\right) - \frac{\nu}{E}\delta_{ij}\delta_{kl} \tag{3.8} $$

for which the second term on the RHS of Equation 3.7 becomes,

$$\left(\frac{\partial S_{ijkl}}{\partial c}\sigma_{kl}\right)\mathrm{d}\sigma_{ij} = \left[\frac{\partial}{\partial c}\left(\frac{1+\nu}{E}\right)\sigma_{ij} - \frac{\partial}{\partial c}\left(\frac{\nu}{E}\right)\sigma_{kk}\right]\mathrm{d}\sigma_{ij} \tag{3.9}$$

In the context of thin film silicon electrodes, $\sigma_{ij} = \sigma_f$ represents a state of equibiaxial stress within the plane of the film and zero stress in the out-of-plane direction. Equation 3.9 then becomes,

$$\left(\frac{\partial S_{ijkl}}{\partial c}\sigma_{kl}\right)\mathrm{d}\sigma_{ij} = \frac{\partial}{\partial c}\left(\frac{1}{M_f}\right)\sigma_f\,\mathrm{d}\sigma \tag{3.10}$$

where $M_f = \frac{E_f}{1-\nu_f}$ is the biaxial modulus of the film and varies with Li composition. If the compositional strain is also taken to be isotropic such that,

$$\varepsilon_{ij}{}^{c} = \frac{\varepsilon_v{}^{c}}{3}\delta_{ij} \tag{3.11}$$

where $\varepsilon_v{}^{c}$ is the volumetric strain due to a change in Li composition, then the ratio (r) of the second term of Equation 3.7 to the first term is,

$$r = 3\sigma_f\left[\frac{\frac{\partial}{\partial c}\left(\frac{1}{M_f}\right)}{\frac{\partial}{\partial c}\varepsilon_v{}^{c}}\right] \tag{3.12}$$

In situ AFM scanning experiments by Beaulieu *et al.* revealed that the volumetric strain of a thin film silicon electrode varies linearly with composition [82]. Taking $c = 3.75$ to correspond to the composition of the electrode at 270% volumetric strain, $\eta = \frac{\partial}{\partial c}$ is a constant and is approximately 0.7 (Table 3.1). M_f is observed in Section 2.4.5 to decrease from 65 GPa at $c = 0.4$ to 30 GPa at $c = 3.5$ (Figure 2.16). A similar decrease in the biaxial modulus is predicted using elastic constants taken from *ab initio* molecular dynamic (AIMD) simulations by Shenoy *et al.* [83] We observed $\sigma \sim$0.5 GPa for a large portion of lithiation and delithiation, typically between $c = 0.5$

to $c = 3.5$ (2.13). Within this range of composition, substituting the relevant values of the parameters in Equation 3.12 yields $r \sim 1\%$. Hence, it can be concluded that the contribution from the second term in Equation 3.7 is small compared to that of the first term and will therefore be ignored in the subsequent discussion.

Table 3.1: Parameters used to calculate r in Equation 3.12.

Parameter	Approx. Value
σ_f	0.5 GPa (Figure 2.13)
$\frac{\partial}{\partial c}\left(\frac{1}{M_f}\right)$	0.007 (Ref. [36], Section 2.16)
$\eta = \frac{\partial}{\partial c}$	0.7 (Ref. [82])

As a consequence of the above analysis, it is sufficient to use the linear form of the Larché-Cahn chemical potential for finite strain applications as long as the Cauchy stress (σ_{ij}) is used as the appropriate stress measure [40, 44]. Thus, the equilibrium chemical potential of Li in Si is given as,

$$\mu_{Li}(Si) = \mu_{ref} + RT \log\left(\gamma \frac{c}{c_{max} - c}\right) - \frac{v_{Si}\eta}{3}\sigma_{kk} \tag{3.13}$$

where $\sigma_{ij} = 0$ and $c = c_{max}/2$ define the reference state, γ is the activity coefficient of Li in Si, and $v_{Si} = 1/\rho_0{}'$ is the molar volume of Si in the reference configuration.

3.2.2 Equilibrium Potential of a Li-Si Half-Cell ($\mathbf{E_0}$)

When a piece of silicon with some concentration (c) of Li is immersed in a liquid electrolyte containing Li^+ ions, an equilibrium reaction is expected to occur at the electrode surface between the Li in the silicon ($Li(Si)$), the Li^+ ions in the electrolyte ($Li^+(elyte)$), and the electrons in the silicon ($e^-(Si)$):

$$LI(Si) = Li^+(elyte) + e^-(Si) \tag{3.14}$$

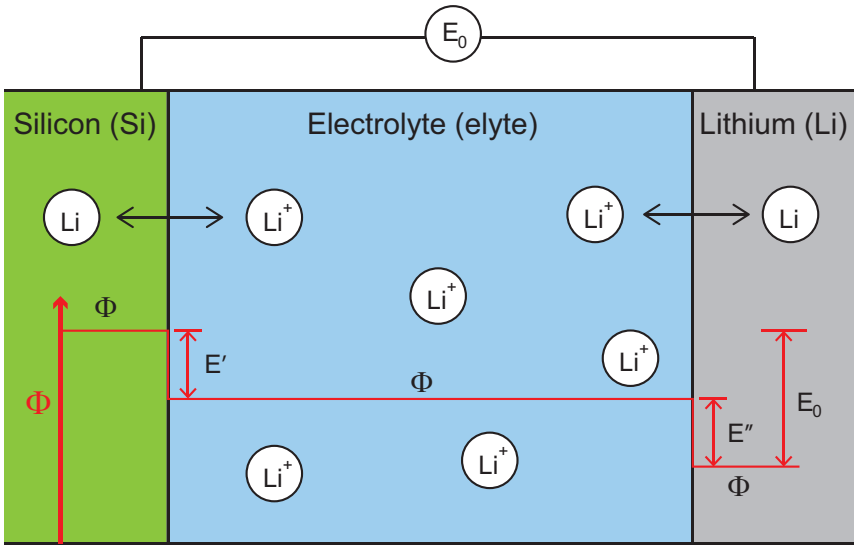

Figure 3.4: Schematic of a Li-Si half-cell in chemical equilibrium. The silicon contains some concentration (c) of Li and is under some state of stress (σ_{ij}).

Note that the symbols in parenthesis indicate the phase where the preceding species is found. The system eventually reaches a state of electrochemical equilibrium such that there is no net change in the concentration of reactants and products. The equilibrium condition in this case is,

$$\sum_i n_i \bar{\mu}_i = 0 \tag{3.15}$$

where n_i is the number of species i and $\bar{\mu}_i$ is the electrochemical potential of species i. The electrochemical potential is a thermodynamic measure of a species' chemical potential (μ_i) that also takes into consideration the electrostatic energy contribution from its charge,

$$\bar{\mu}_i = \mu_i + z_i F \Phi_I \tag{3.16}$$

Here, z_i is the valence (or charge) of species i, F is the Faraday constant and Φ_I is the local electrostatic potential of phase I. In the case of an atom with no charge, $z = 0$ and $\bar{\mu}_i = \mu_i$. Taking the Li in silicon to have no charge (an approximation arising from the assumed electrical conductivity of lithiated silicon), the equilibrium

chemical potential of Li in silicon ($\mu_{Li}(Si)$) comes out to be,

$$\mu_{Li}(Si) = \mu_{Li^+}(elyte) + \mu_{e^-}(Si) - F(\Phi_{Si} - \Phi_{elyte}) \tag{3.17}$$

Let $E' = (\Phi_{Si} - \Phi_{elyte})$ be the potential difference between the silicon electrode and electrolyte. If a piece of lithium metal is then added to the system, $E'' = \Phi_{elyte} - \Phi_{Li}$ is the potential difference once equilibrium is established between the electrolyte and lithium metal. Given that the concentration of Li^+ ions in the electrolyte is not affected by the introduction of Li metal (typically true of most commercial Li-ion battery electrolytes, including the one used in this study), $E_0 = E' + E''$ is the potential of the resultant Li-Si half-cell (Figure 3.4).

Thus, the equilibrium potential of a silicon electrode (E_0) at a state of stress σ_{ij} at a given composition of Li c can be written as,

$$FE_0 = \mu' - RT \log\left(\gamma \frac{c}{c_{max} - c}\right) + \frac{v_{Si}\eta}{3}\sigma_{kk} + FE'' \tag{3.18}$$

where μ' is given as,

$$\mu' = \mu_{Li^+}(elyte) + \mu_{e^-}(Si) - \mu_{ref} \tag{3.19}$$

μ' and E'' will be constant if the concentration of Li^+ ions in the electrolyte remains constant.

3.3 Experimental Procedure

Thin film silicon electrodes (TFSEs) are fabricated onto a circular, elastic substrate and cycled at constant current. During lithiation, the influx of Li atoms into silicon induces a volumetric strain proportional to the state of charge [82]. For a TFSE, this strain results in a state of plastic flow at a compressive stress of ~1 GPa (Section 2.4.3, [35]).

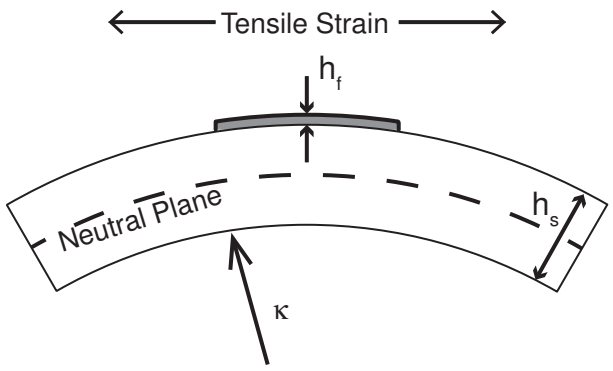

Figure 3.5: Curvature-induced tensile strain in a silicon thin film during lithiation induces elastic unloading of the film.

If the substrate is subjected to a curvature change ($\Delta\kappa$) as shown in Figure 3.5, a tensile strain is induced in the silicon film which unloads the Si electrode from the state of yield.

If the film thickness (h_f) is small compared to that of the substrate (h_s), the variation in the induced strain through the thickness of the film is negligible and the strain in the film can be taken as the strain at the surface of the substrate due to the imposed curvature change. For an isotropic substrate with uniform thickness, the neutral plane coincides with its mid-plane and the strain at the surface can be expressed as,

$$\Delta\varepsilon = \frac{\Delta\kappa h_s}{2} \tag{3.20}$$

Since the electrode is under compressive stress during lithiation, the imposed tensile strain results in elastic unloading of the electrode. Elastic stress-strain relations relate the change in stress state ($\Delta\sigma_{ij}$) due to the change in substrate curvature to the change in the state of strain in the film. Assuming **(a)** the applied strains to the electrode do not change the behavior of the electron double layer at the electrode surface and **(b)** the composition of the electrode remains constant, Equation 3.18 gives the following relation between the change in the equilibrium cell potential as a

result of a change in stress state in the silicon anode:

$$\Delta E_0 = \frac{v_{Si}\eta}{3F}\Delta\sigma_{kk} \tag{3.21}$$

By experimentally measuring the change in cell potential due to the applied strain, we can determine the stress-potential coupling magnitude at a given composition. Additional measurements at different compositions and over multiple cycles are made to obtain a more comprehensive understanding of the stress-potential coupling behavior.

3.3.1 Electrode Fabrication

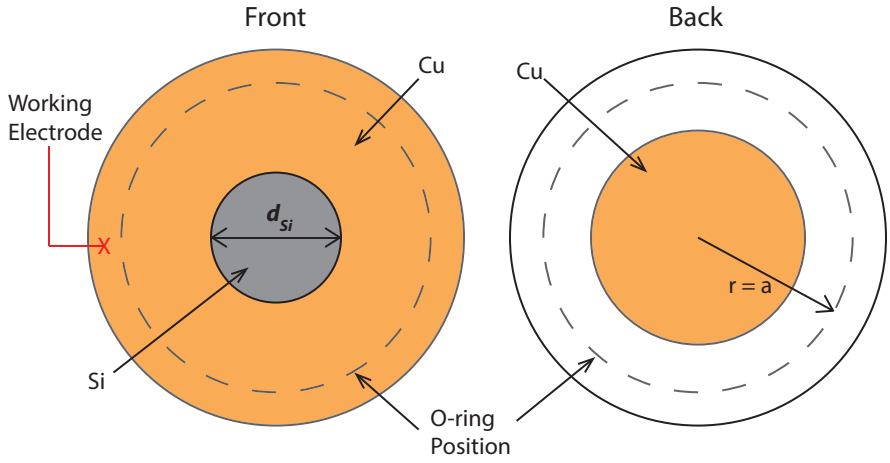

Figure 3.6: Schematic of wafer sample. (**Front**) Si electrode (grey) on Cu current collector (orange). Electrical lead is connected at the edge of the wafer, allowing for a tight seal for the o-ring (dotted lines). (**Back**) Cu film for cleaner MOS signal.

Fused silica wafers (double-side polished, 50 mm diameter, 500 ± 20 µm thick) are used as substrates for thin film Si electrodes. A 40 nm film of Ti is deposited onto the front of the wafer using e-beam physical vapor deposition (Kurt J. Lesker, Lab-18), followed by 200 nm of Cu. The Cu underlayer provides uniform current distribution in the Si film and contact area for the leads while the Ti layer improves adhesion between the wafer and the Cu layer. A thin film of Si (thickness h_f and diameter

d_{Si}) is then sputtered onto the Cu layer using a shadow mask RF magnetron sputtering, Lesker Lab-18). The diameter of the Si is limited to 8 mm to minimize strain variations within the anode during measurements (Appendix B). The thicknesses of the films are measured using a surface profilometer (Dektak3) and a white-light interferometer (Zygo NewView 6000). The thickness of each sample's substrate was measured within 0.001 mm accuracy with a high precision dial micrometer (Mitutoyo). The electrodes are assembled in a special electrochemical cell (Figure 3.7) then cycled with a potentiostat (Solartron Analytical 1470E) using constant current, constant voltage (CCCV) protocol at 10 µA current. Given the relatively large area of Cu vs. Si, the current density in the Si electrode is initially very small (∼0.6 µA/cm^2). Assuming SEI formation continues throughout the experiment (though at a lesser extent after the first cycle [41]), the current density in the film may range from 5–15 µA/cm^2 during the measurements. The lower and upper cutoff potentials are set at 50 mV and 0.6 V, respectively.

3.3.2 Electrochemical Cell

The cell consists of two sections (Figure 3.7, separated by the wafer and each section sealed with non-conductive perfluoro-elastomer (FFKM) o-rings from Marco Rubber (Markez Z1206). The lower section functions as an electrochemical half-cell with Si as the working electrode and Li metal as the counter electrode. A commercial liquid electrolyte (BASF Selectilyte Series A6) which is a solution of 1.2 M lithium hexafluoro-phosphate ($LiPF_6$) in ethylene carbonate/diethylene carbonate (1:2 by weight) is used to provide ionic transport between the two electrodes.

The upper section is connected to a ultra-high purity (UHP) argon gas cylinder with a high precision regulator (1–15 psi range) and digital pressure gauge (1 mbar precision). A laser grade window at the top of the cell allows for MOS curvature measurements of the wafer. The cell is held together with a circular array of six

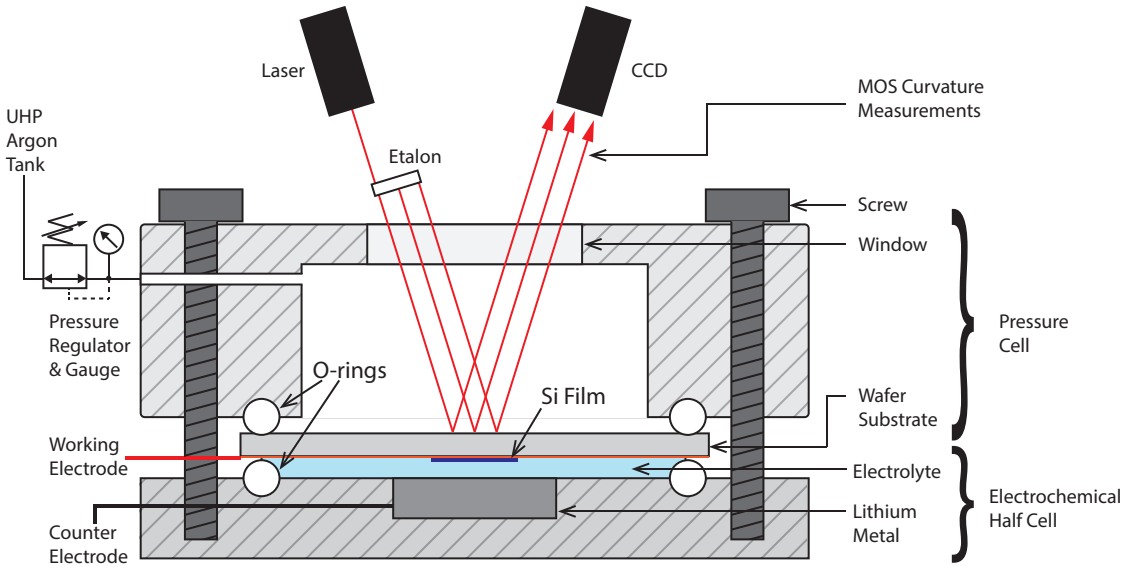

Figure 3.7: Schematic of electrochemical cell. The FFKM o-rings function as both sealant and clamping mechanism. Given that the boundary conditions of the clamping mechanism can range anywhere between simply supported to rigidly clamped, it is necessary to monitor the substrate curvature in addition to the applied pressure (Appendix B).

screws that help maintain the seal in each section and provide the uniform mechanical clamping force along the edge of the wafer.

3.3.3 Curvature Measurements with MOS

The substrate curvature is monitored using a multibeam optical sensor (MOS) wafer curvature system (kSA-MOS, kSpace Associates, Inc.), and illustrated schematically in Figure 3.7. The MOS system uses a 2x2 array of parallel laser beams that reflect off the sample surface onto a CCD camera. The relative change in the spot spacing is related to the wafer curvature by,

$$\Delta\kappa = \frac{d - d_0}{d_0}\left(\frac{1}{A_m}\right) \tag{3.22}$$

where d is the distance between two adjacent laser spots on the CCD camera

(see Figure 1b in Ref. [35]) and d_0 is the initial distance. A_m is the mirror constant determined from MOS measurements of two reference mirrors with known curvatures. The curvature is decomposed into two orthogonal directions ($\Delta\kappa_x$ & $\Delta\kappa_y$), calculated from the horizontal and vertical spot spacing, respectively.

3.3.4 Calculating Stress

Taking the silicon electrode to be an isotropic thin film, the change in the electrode's state of stress is given by Hooke's law under plane stress conditions. In matrix form,

$$\begin{bmatrix} \Delta\sigma_{xx} \\ \Delta\sigma_{yy} \\ \Delta\sigma_{xy} \end{bmatrix} = \frac{E_f}{1-{\nu_f}^2} \begin{bmatrix} 1 & \nu_f & 0 \\ \nu_f & 1 & 0 \\ 0 & 0 & \frac{1-\nu_f}{2} \end{bmatrix} \begin{bmatrix} \Delta\varepsilon_{xx} \\ \Delta\varepsilon_{yy} \\ \Delta\varepsilon_{xy} \end{bmatrix} \tag{3.23}$$

where E_f and ν_f are the Young's modulus and Poisson's ratio of the silicon film that vary with Li concentration. $\Delta\varepsilon_{xx}$ and $\Delta\varepsilon_{yy}$ are the in-plane strain components of the electrode determined from Equation 3.20 using the two orthogonal curvatures:

$$\begin{aligned} \Delta\varepsilon_{xx} &= \frac{\Delta\kappa_x h_s}{2} \\ \Delta\varepsilon_{yy} &= \frac{\Delta\kappa_y h_s}{2} \end{aligned} \tag{3.24}$$

Substituting this into Equation 3.23,

$$\Delta\sigma_{kk} = \Delta\sigma_{xx} + \Delta\sigma_{yy} = M_f(\Delta\kappa_x + \Delta\kappa_y)\frac{h_s}{2} \tag{3.25}$$

The above equation gives the change in stress of the silicon electrode at constant SOC due to the change in curvature of its substrate. $M_f = \frac{E_f}{1-\nu_f}$ is the Li concentration-dependent biaxial modulus of the Li_xSi and was discussed previously in Section 2.4.5. Given the discrepancy between the estimated biaxial modulus values (M_{est}) to the experimentally measured values of M_f (Figure 2.16), the experimentally determined

values are used in the following calculations to avoid additional uncertainty in the measurements.

3.4 Results

During initial lithiation, the potential of the Li-Si half cell drops from an OCP of ∼3 V to ∼250 mV, where it exhibits a plateau for some duration of time (t_{lith0}) before gradually decreasing to the lower cutoff potential (see Figure 4.6). The plateau is indicative of a phase transformation of the sputtered amorphous silicon (a-Si) film into an amorphous lithiated silicon phase, a-Li$_x$Si [79, 80]. In order to maintain consistency with the Larché-Cahn model, measurements during the first lithiation cycle are taken after the potential falls below 200 mV where the lithiated silicon is presumed to behave like a solid solution. Subsequent cycles do not exhibit this plateau and are taken to behave as a solid solution throughout the entire cycle.

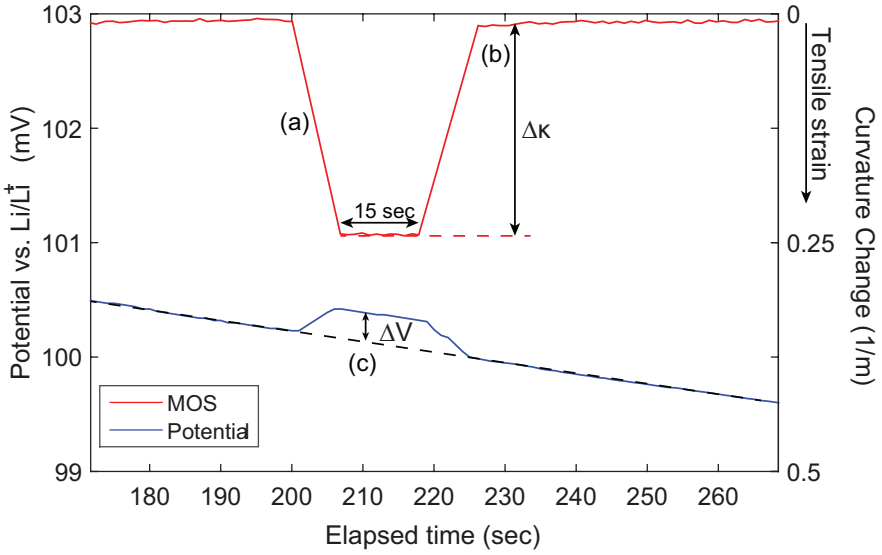

Figure 3.8: Potential jump due to change in substrate curvature. (a) Pressure is applied to the substrate. (b) MOS measures the resultant curvature change. (c) Potentiostat measures the voltage jump due to tensile strain induced by curvature. Once the pressure is released, the curvature returns to zero and the potential continues along its original trajectory. Each pulse typically lasts 10-15 seconds.

An representative experimental measurement of the stress-potential coupling is shown in Figure 3.8. During constant current lithiation, the concentration of Li in the Si electrode increases and the cell potential vs. the Li counter electrode decreases gradually with time. A momentarily application of pressure to the substrate induces a tensile strain in the film, elastically unloading it. As a result of the change in film stress, there is a corresponding jump in cell potential. Releasing the pressure returns the curvature of the substrate to its original value and the cell potential continues along its initial trajectory. Simultaneous measurements of potential change (ΔV) and the stress change via curvature change ($\Delta\kappa$) during the pressure pulse establishes the stress-potential coupling at the corresponding SOC. Multiple measurements with increasing pressures (Figure 3.9) produce a scatter plot of ΔV vs. $\Delta\sigma_{kk}$ values — the slope of which gives the stress-potential coupling magnitude (Y_{LiSi}) at the given SOC.

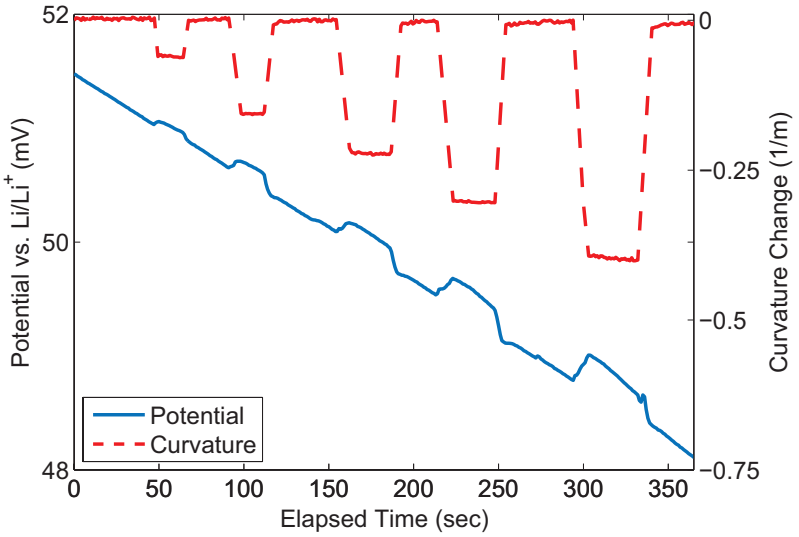

Figure 3.9: A typical set of measurements for a given SOC.

Repeating these measurements over a range of SOCs and over several cycles yields a comprehensive data set, revealing variations in Y_{LiSi} from as low as 20 mV/GPa to 115 mV/GPa. Figure 3.10 is a cumulative plot of five different samples of two different initial thicknesses (2 samples of 204 nm and 3 samples of 145 nm).

The distribution of Y_{LiSi} with SOC and cycle number is illustrated in Figure 3.11. On the y-axis is the slope of a set of data points in Figure 3.10; on the x-axis is the SOC represented by Li composition (x). Each point in Figure 3.11 represents one slope measured at a given SOC and connected points indicate measurements taken on the same sample within the same cycle. Cycle numbers are distinguished by color and marker shape, where blue circles are measurements taken during the initial lithiation of the silicon electrode. Figure 3.11 shows that the values of Y_{LiSi} tend to increase with increasing Li content (x) for a given lithiation cycle, while the values from the first cycle are generally higher than subsequent cycles for a given SOC.

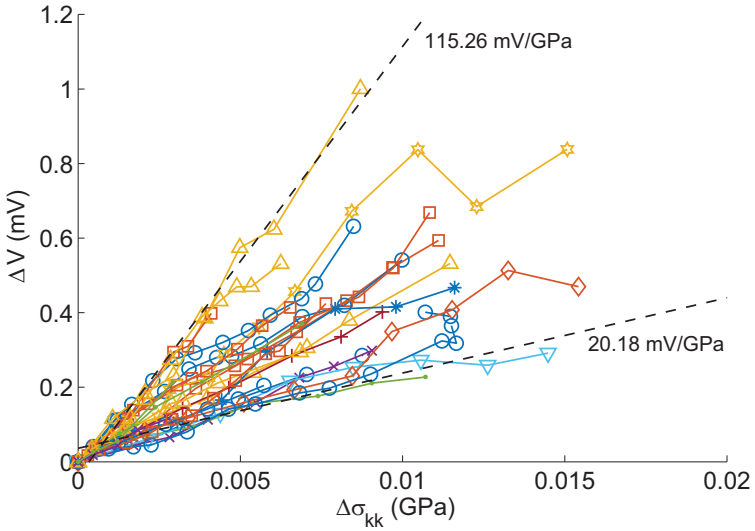

Figure 3.10: Compilation of 5 different samples showing a range of stress-potential coupling magnitudes. Each data point is one pressure pulse and a connected set of points represents one set of measurements. For small stresses and strains, the Larche-Cahn potential predicts a linear relationship between ΔV and σ_{kk}. The slope of the scatter plot, then, is the magnitude of the stress-potential coupling factor, Y_{LiSi}.

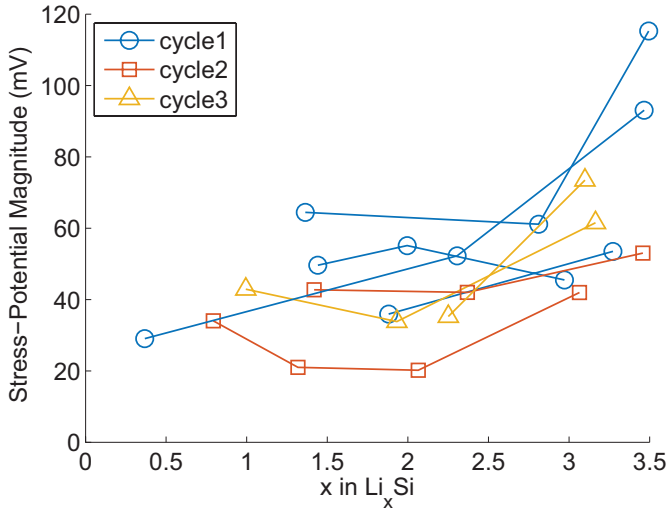

Figure 3.11: Stress-potential magnitude variation with Li concentration and cycle number. Each point is one slope measured at a given SOC and connected points indicate measurements taken on the same sample for a given cycle. Cycle numbers are distinguished by color and marker shape, where blue circles are measurements taken during the initial lithiation of the silicon film.

A similar plot using the rule of mixtures to calculate M_f shows nominal changes to these bounds (15 - 114 mV/GPa), while the upward trend of Y_{LiSi} with Li content become more pronounced (Figure 3.12). Therefore, the discrepancy between the experimental and computational values of M_f does not appear to impact the overall stress-potential coupling behavior of the silicon electrode. Furthermore, it appears that the biaxial modulus does not strongly influence the variation in Y_{LiSi}.

Figure 3.13 is a cumulative plot of ΔV vs. $\Delta\varepsilon_{kk}$ analogous to Figure 3.10 to illustrate the influence of M_f to the variation and upward trend of Y_{LiSi} with Li content. Since ε_{kk} is measured directly from curvature measurements (Equation 3.24), Figure 3.13 shows that the variation Y_{LiSi} is not caused by the changing biaxial modulus of the film. Also note the two dotted lines indicating the minimum and maximum slopes that exhibit a similar variation in the slopes with that of Figure 3.10. This suggest that the variations in the stress-potential coupling magnitudes are an observed phenomenon of the material.

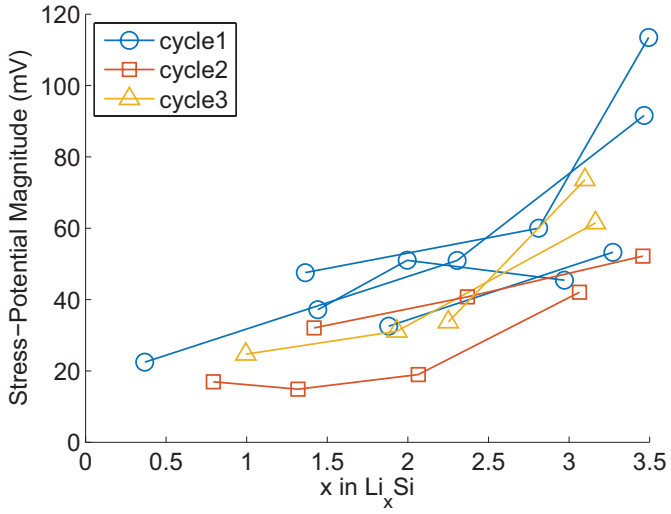

Figure 3.12: Stress-potential magnitude variation with Li concentration and cycle number using elastic constants from Shenoy's DFT calculations. The upward trend and higher first cycle values of the magnitudes are insensitive to the uncertainty between theoretically and experimentally determined biaxial moduli.

3.5 Discussion

The experimental results in the preceding section suggest that Y_{LiSi} varies between 20–115 mV/GPa with Li content while, paradoxically, the Larché-Cahn model predicts a constant value for the stress-potential coupling magnitude (Y_{LiSi}). Equation 3.21 gives the stress-potential coupling in a thin film silicon electrode based on the Larché-Cahn chemical potential at constant composition. Given the density of amorphous silicon to be 2.2 g/cm^3 [90], from which v_{Si} = 12.7 cm^3/mol and F = 96485 C/mol, the Larché-Cahn model predicts,

$$\frac{\Delta E_0}{\Delta \sigma_{kk}} = \frac{v_{Si}\eta}{3F} = 62\text{mV/GPa} \tag{3.26}$$

To understand the cause of this discrepancy, consider the three terms that define the stress-potential magnitude (Equation 3.26. F is the Faraday constant and v_{Si} is the molar volume of the Si film in the reference configuration, which is also constant. $\eta = \frac{\partial {\varepsilon_v}^c}{\partial c}$ is the change in volumetric strain with respect to Li concentration. *In situ*

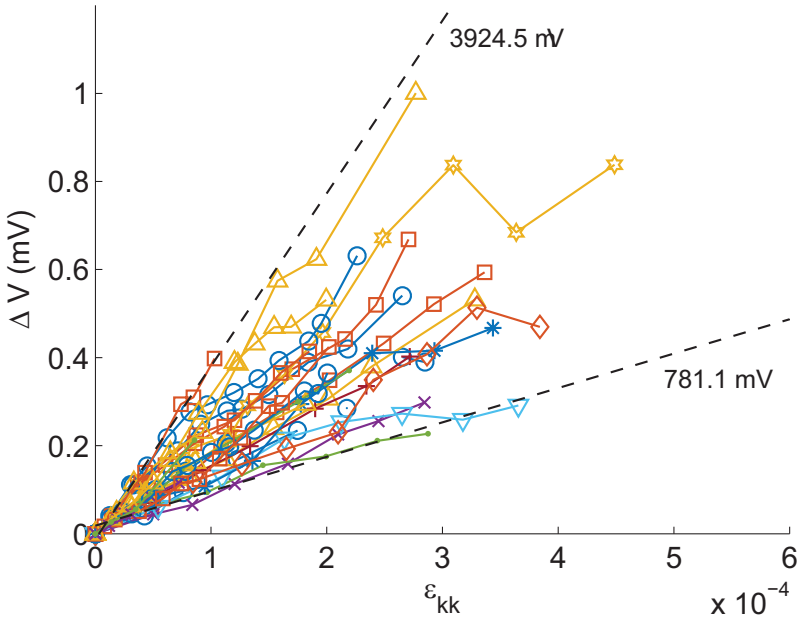

Figure 3.13: Potential jump due to applied strain. Since both ΔV and $\Delta\varepsilon_{kk}$ can be measured directly, the variation of slopes is most likely not an artifact of the changing elastic constants of lithiated silicon.

AFM scans showed the volumetric strain of a thin film silicon electrode varies linearly with Li content [82], suggesting that η is effectively constant as well. This result was confirmed by another member of our research group using a similar *in situ* AFM technique. These observations suggest that the Larché-Cahn chemical potential may not fully characterize the physics involved in this system.

Furthermore, *in situ* studies of silicon islands [48, 82] also observe that a thin film of Si does not return to its original volume after the first lithiation/delithiation cycle. If the stress-potential magnitude depends on the compositional volumetric strain, then this irreversible volume change during the first cycle may explain the difference in the first cycle values of Y_{LiSi} to subsequent cycles. Recently, a new continuum model by Bower *et al.* to allow for irreversible volume changes (a phenomenon not account for in current models) suggests that vacancies can form as a result of plastic deformation during the lithiation of silicon [91]. According to this model, it is possible that η may vary if the rate of vacancy formation is dependent on the rate of plastic

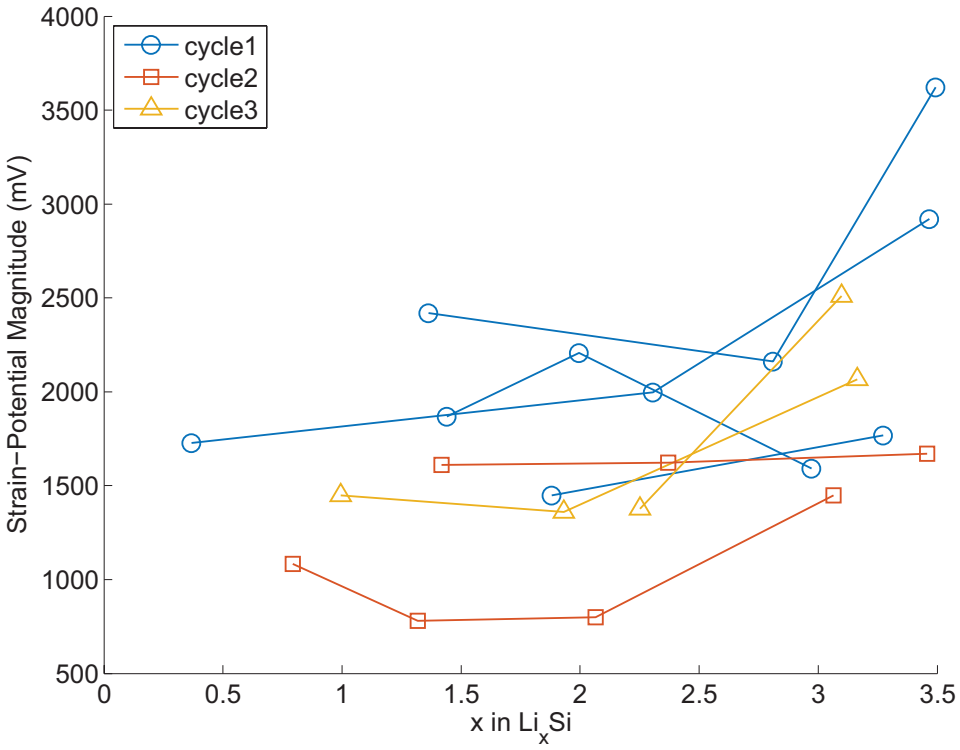

Figure 3.14: Compilation of 5 different samples showing a range of stress-potential coupling magnitudes (Y_{LiSi}). Each data point is one pressure pulse. Maximum applied tensile stress is 16 MPa. The dotted lines indicate the upper and lower bounds of the magnitudes.

strain or compositional change.

The existence of the stress-potential coupling behavior has several implications. Recent studies of the equilibrium potential as a function of SOC for the Li-Si system using the galvanostatic intermittent titration technique (GITT) [23, 69, 92] and OCP relaxation experiments [38] report two equilibrium potentials – one corresponding to the lithiation direction and one corresponding to the delithiation direction. Equation 3.18 shows that compressive and tensile stresses will respectively lower and raise the equilibrium potential at a given Li composition. Thus, the difference in stress states at a given SOC ($\Delta\sigma_{SOC}$) may explain the observed difference in equilibrium potentials of the electrode. For example, Baggetto *et al.* reports the equilibrium potentials vary by 280 mV at $Li_{1.25}Si$ and 150 mV at $Li_{3.5}Si$ [92], which correspond to 50–60% of the

total potential offset of the electrode when cycled at C/10 rate. It is believed that the origin of the equilibrium potential difference may be thermodynamic in nature. Taking $\Delta\sigma_{SOC} \approx 1.2$ GPa and $Y_{LiSi} = 62$ mV/GPa, it is plausible that the stress-potential coupling behavior makes a considerable contribution (about 60–70 mV) to the difference in equilibrium potential.

The electrode stress also has implications for the maximum realizable charge and discharge capacity, similar in the way kinetic overpotential and ohmic drop affect these capacities. From our foregoing discussion, the potential offset exhibited by the lithiated silicon has two components: the overpotential required to drive a finite current and the stress effect. The Butler-Volmer equation describes the shift in the measured potential of an electrode away from the equilibrium potential as a result of a finite current. Consequently, the lower cutoff potential is reached prematurely during lithiation and the cycle finishes at a lower state of charge than theoretically possible. Similarly, the upper cutoff potential is reached before all the lithium can be extracted from the electrode during delithiation, resulting in a reduction in the maximum realizable discharge capacity. The stresses in the electrode can further exacerbate the reduction in realizable capacity by shifting the potential even further from its theoretical equilibrium value (Figure 3.15). These conclusions confirm results by Sheldon et al., who report decreased Li solubility in silicon electrodes as a result of stress in the material [47].

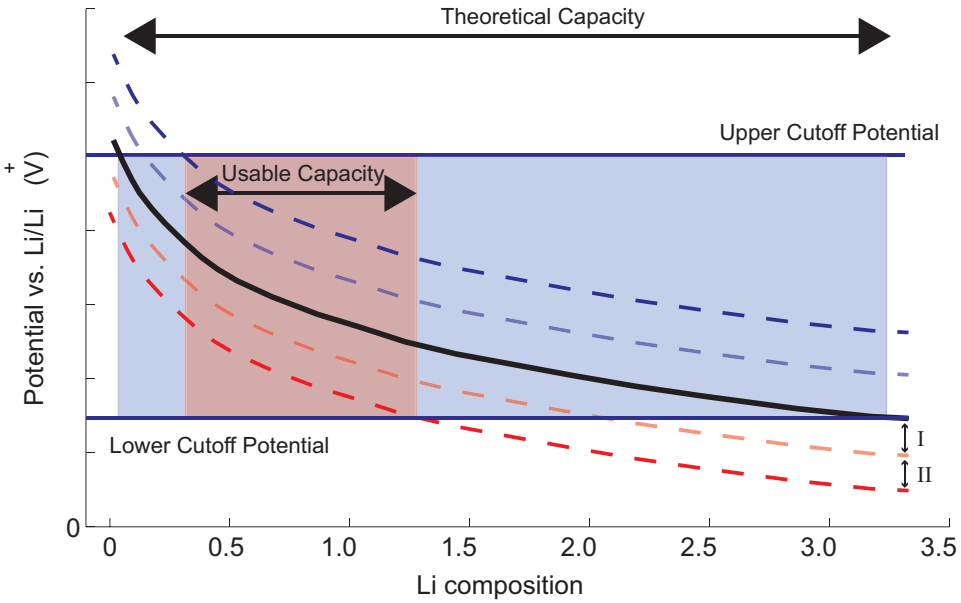

Figure 3.15: Compilation of 5 different samples showing a range of stress-potential coupling magnitudes (Y_{LiSi}). Each data point is one pressure pulse. Maximu applied tensile stress is 16 MPa. The dotted lines indicate the upper and lower bounds of the magnitudes.

Since the area of the potential vs. capacity loop represents the energy dissipation in each cycle, the stress effect on the potential also impacts the energy efficiency of the electrode. In the previous chapter, the energy dissipation due to plastic deformation of lithiated silicon is shown to be comparable to the polarization losses. Eliminating the mechanical dissipation would result in an equivalent improvement of energy efficiency of the system. Thus, stress considerations suggest that improvements to energy efficiency and capacity of silicon electrodes can be obtained through electrode designs that minimize or eliminate stresses in the material.

3.6 Conclusion

An experimental setup to induce mechanical strain to a thin film electrode independent of lithiation is demonstrated. The setup is used to measure the magnitude of the stress-potential coupling factor of lithiated silicon (Y_{LiSi}) at a given state of charge.

The change in stress is calculated from the change in curvature of the substrate and the Li concentration-dependent biaxial modulus of the film, M_f. MOS is used to measure the curvature change, which varies linearly with the applied pressure (Appendix B), while values for the biaxial moduli are determined separately. We find that Y_{LiSi} varies between 20–115 mV/GPa and tends to increase with increasing Li concentration. This variation in Y_{LiSi} can be attributed to the evolving free volume of the Si film, which becomes diffuse at high Li content. In light of these observations, we recommend correcting current models to incorporate an evolving free volume of the solute (i.e., Si). This setup provides an elegant method to precisely control stress and strain variations in a thin film electrode, providing a means of quantitative analysis of the influence of stress on electrode potential, with applications extending beyond lithium-ion battery research. The experimental method presented in this section can provide quantitative values of the evolving free volume once the stress-potential coupling behavior is corrected for the evolving free volume.

Chapter 4

Fracture Energy of Lithiated Silicon

4.1 Introduction

Wider use of silicon-based anodes as viable electrodes is hindered by durability issues stemming from large volume changes during cycling that lead to mechanical degradation of the active material and the surrounding matrix. This can lead to loss of active material (thus, capacity), while fracturing within the active material creates new surfaces that further exacerbate capacity loss due to SEI formation [85],Maranchi2006. Efforts to develop novel architectures such as micro/nano-wires, patterned microstructures and coated particles using an iterative method have made improvements to capacity retention [16–21, 27]. Recently, there have been efforts to empirically determine critical dimensions for microstructures and particles that resist fracture [22, 25, 45, 48, 93–96]. What still remains elusive, however, is the ability to systematically optimize the designs of such architectures to minimize and even eliminate the likelihood of mechanical degradation. For this to occur, it is necessary to make quantitative measurements of the stresses in the material that drive damage and failure, and the material properties that resist them. Recent attempts to measure the fracture energy of lithiated silicon report values between 5.4–11 J/m^2 [42, 46, 97]. However, these

attempts have been unable to pinpoint the critical material properties at the onset of fracture, resulting in a high degree of uncertainty in the reported values.

In this chapter, an experimental technique is developed to observe a pre-crack in a thin film silicon electrode during cycling. This technique is used to measure the fracture energy of lithiated silicon using linear elastic thin film mechanics. Utilizing the real-time stress measurements demonstrated in Chapter 2, the critical stress and state of charge of the electrode at the onset of crack propagation is ascertained. Since the parameters used to calculate fracture energy evolve with Li content, the fracture energy is measured at various SOC to characterize the material over the full range of Li compositions.

4.2 Background

4.2.1 Energy Release Rate of a Channel Crack

Fracture is a mechanism that allows a system under a mechanical load to reduce its energetic state by means of configurational change. When a crack advances, potential energy in the bulk is released through the formation of new surfaces. The potential energy released per unit surface area formed is known as the energy release rate (G) and has units of J/m^2. At crack initiation, the energy release rate is equal to the energy required to form a unit of new area, also known as the fracture energy.

For demonstrative purposes, imagine a preexisting channel crack of length a in an isotropic thin film of thickness hf bonded to an elastic substrate (Figure 4.1). The film is fully cracked (i.e., the crack goes through the thickness of the film to the underlying substrate) and under a state of tensile stress. The channel crack will propagate when the energy release rate (G) reaches the fracture energy of the material (G_c). For short cracks, the crack front shape and energy release rate change as the crack extends. However, analysis by Nakamura and Kamath show that crack

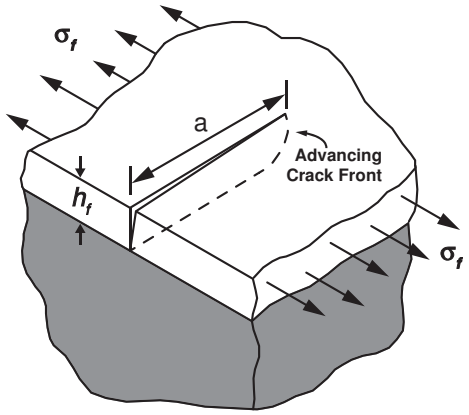

Figure 4.1: Channel crack in a think film on an elastic substrate under tensile stress. Adapted from Ref. [98] with permission.

channeling reaches steady state conditions at crack lengths greater than twice the thickness of the film ($a >> 2h_f$) [99]. For such cracks, Beuth gives an exact solution to the steady state energy release rate along the crack front (G_{SS}) [98],

$$G_{SS} = \frac{\pi}{2}\frac{h_f {\sigma_f}^2}{\overline{E}_f} g(\alpha, \beta) \tag{4.1}$$

Here, $\overline{E}_f = \frac{E_f}{1-{\nu_f}^2}$ is the plane strain modulus of the film, σ_f is the critical film stress that induces crack propagation and $g(\alpha, \beta)$ is a nondimensional measure of crack opening displacement. The Dundurs parameters, α and β, for plane strain problems are given as,

$$\alpha = \frac{\overline{E}_f - \overline{E}_s}{\overline{E}_f + \overline{E}_s}, \qquad \beta = \frac{\mu_f(1-2\nu_s) - \mu_s(1-2\nu_f)}{2\mu_f(1-\nu_s) + 2\mu_s(1-\nu_f)} \tag{4.2}$$

where $\mu = \frac{E}{2(1+\nu)}$ is the shear modulus and the subscript "s" refers to the material properties of the substrate.

Thus, by monitoring a sufficiently long, preexisting channel crack, the fracture energy (G_c) of a thin film silicon electrode can be calculated from the critical film properties at the onset of crack propagation. Since the material properties and thickness of the film vary with SOC, it is necessary to measure G_c at various SOC. Given that Gss scales linearly with film thickness, this can be achieved by varying the initial

film thickness of the silicon film.

4.3 Experiment Design

4.3.1 Sample Fabrication

Fused silica wafers (double-side polished, 50 mm diameter, 250-500 µm thick) are used as elastic substrates for thin film silicon electrodes. The wafers are diced into 6 mm wide strips using a Disco DAD-321 dicing saw and cleaned of particulates prior to electrode fabrication. A 25 nm thick film of titanium followed by 200 nm of copper is deposited onto the front side of the wafer using e-beam physical vapor deposition (Kurt J. Lesker, Lab-18). The copper underlayer provides uniform current distribution to the silicon film and contact area for the leads while the titanium layer improves adhesion between the wafer and the copper layer. A 100 nm film of Cu is deposited on the back side of the substrate to provide a reflective surface for MOS curvature measurements. The curvature of each strip is measured prior to silicon deposition to account for residual stresses developed during sputter deposition of the silicon film.

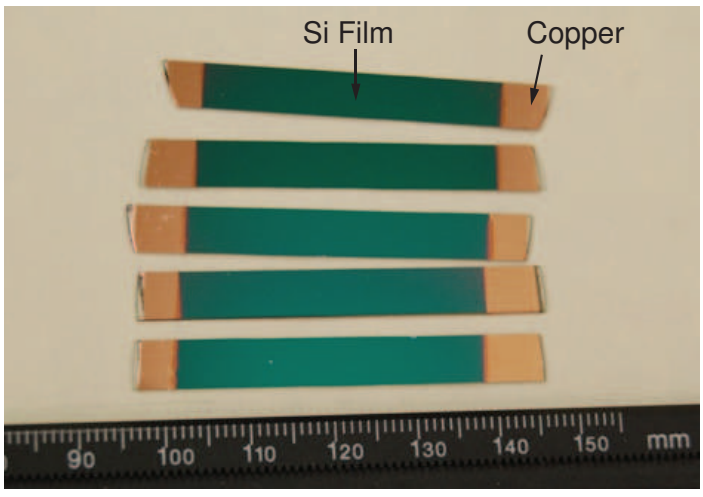

Figure 4.2: TFSE samples on diced wafer substrates with the Si film shown in green.

Thin films of silicon of various thicknesses are deposited by RF magnetron sputtering (Kurt J. Lesker Lab18, p-doped 99.999% Si target) onto the front copper layer. A shadow mask is used to cover the ends of the wafer strips during silicon deposition to provide contact areas for the leads (Figure 4.2). The thicknesses of the films are monitored using a quartz crystal microbalance (QCM) in the deposition chamber and verified with a surface profilometer (Dektak3) and white-light interferometer (Zygo NewView 6000). The thickness of the substrate is measured within 0.001 mm accuracy with a high precision dial micrometer (Mitutoyo).

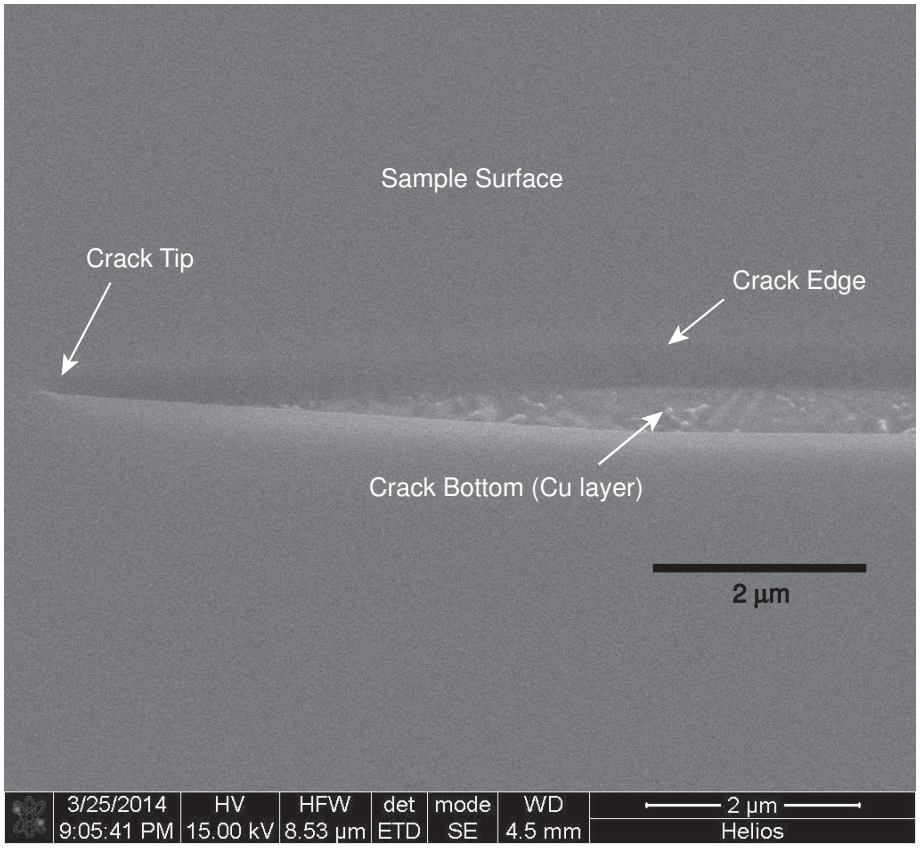

Figure 4.3: SEM image of the tip of the pre-crack. The image is tilted 52 degrees with respect to the SEM objective. The parameters are fine-tuned using dummy samples to obtain cracks through the thickness of the silicon film without removing the underlying copper layer.

An initial crack is then introduced at the center of each Si electrode sample with focused ion beam (FIB) milling using an FEI Helios Nanolab and the bitmap template

shown in Figure A.2 (see Appendix A.3 for detailed procedures). The cracks are approximately 40 µm long and 1 µm wide at the center. Once the extraction current and dwell time are properly calibrated, the FIB is capable of producing crack tip radii ∼10-20 nm and vertical walls along the edges of the crack (Figure 4.3).

4.3.2 Electrochemical Cell

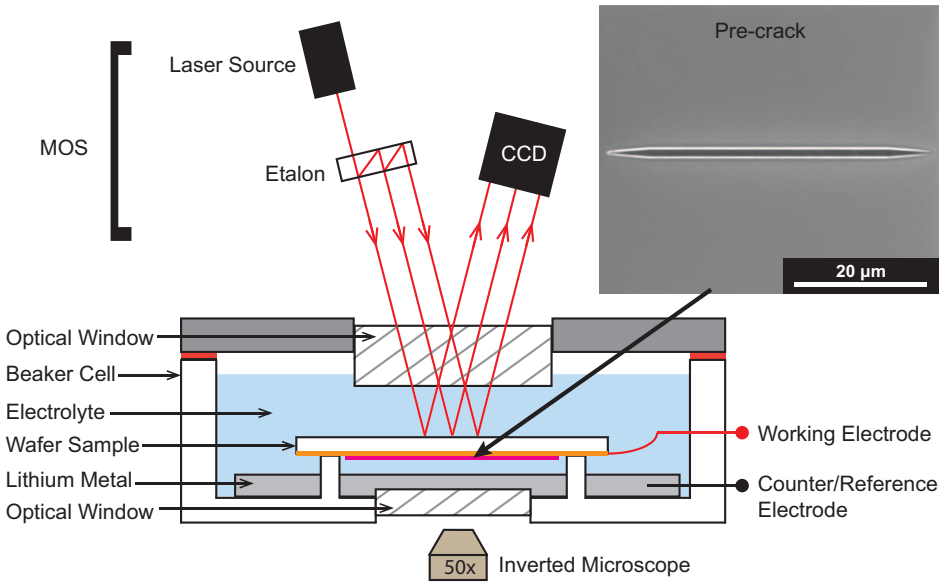

Figure 4.4: Schematic of electrochemical cell and MOS setup. The ends of the sample are supported by notches, allowing it to bend freely without external moments or forces for accurate curvature measurements. The silicon film is on the lower surface and is imaged by the optical microscope while curvature measurements are taken off the upper surface using MOS.

The thin film silicon electrode (TFSE) samples are assembled in a custom beaker cell that allows for simultaneous *in situ* imaging of the sample surface and *in situ* stress measurements of the film during cycling (Figure 4.4). A CCD camera on an inverted microscope monitors and records images of the crack during cycling while MOS records the curvature of the substrate.

The beaker cell is designed to support the wafer strip at each end over a glass window to allow for electrolyte to reach the film surface while minimizing the gap

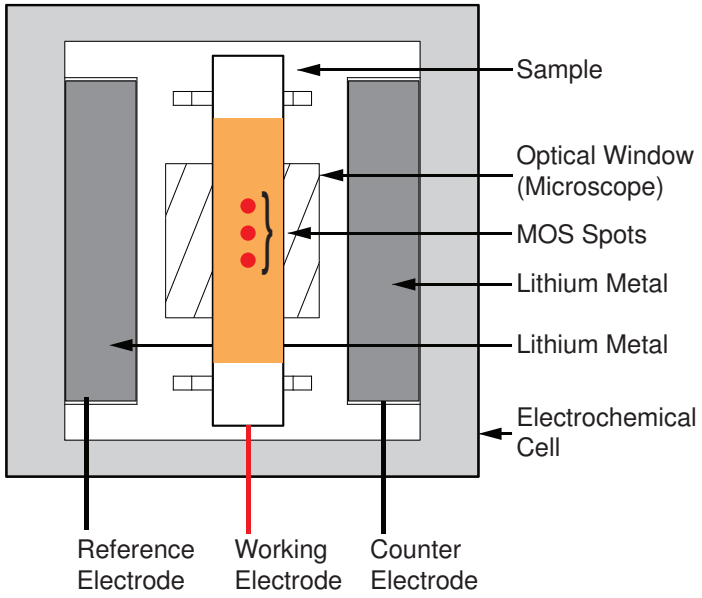

Figure 4.5: Top view of electrochemical cell showing layout of sample and Li metal. The sample is simply supported by the two notches above and below the optical window.

between the window and sample surface for clearer optical images. The sample rests on two notches so that it can bend freely without experiencing external moments at the edges. Lithium metal is used as the counter and reference electrode and positioned along the length of the sample to make room for the window while minimizing the distance between the two electrodes (Figure 4.5). Since the electrodes are not in contact with each other, there is no need for polymer separators for this setup. Instead, the cell is flooded with liquid electrolyte such that the upper optical window is submerged under the electrolyte. This allows for ionic conductivity between the silicon electrode and Li metal while avoiding distortions to the MOS laser beam. The electrolyte used is a 1.2 M $LiPF_6$ in 2:1 ethylene carbonate:diethyl carbonate solution (BASF Selectilyte Series A6).

4.4 Experimental Procedure

Samples are assembled with the silicon film facing down in the electrochemical cells in ultra-high purity (UHP) Argon glove box with oxygen and moisture levels below 0.1 ppm. The cells are sealed using a silicone rubber gasket and checked for leaks. Once assembled, the cells are removed from the glove box and placed onto the inverted microscope's stage. A Solartron Analytical 1470E potentiostat is used to conduct constant current, constant potential (CCCP) experiments with 0.05 V and 1.2 V as the lower and upper cutoff potentials. To avoid variations in concentration gradients between samples, the silicon films are lithiated at a fixed current density of 12.5 $\mu A/cm^2$ (C/8 – C/15 rate) instead of a fixed charge rate.

During electrochemical cycling, images of the sample surface are recorded using a CCD camera mounted to an inverted microscope (Nikon Eclipse MA100) while stress measurements are made with MOS using a linear array of spots. The microscope is equipped with 20x and 50x long working distance objectives. A LabVIEW VI is programmed to display live images of the sample at 5 frames per second, though images are saved to the hard drive at 60 second intervals to conserve disk space. The higher frame rate allows the user to focus the microscope between recorded images, since the curvature changes in the sample often causes the sample surface to leave the focal plane of the objective. The time at which the crack initiates (t_c) is determined from the time stamp of the recorded images. The corresponding curvature and SOC at t_c is used to calculate the fracture energy of the film.

To account for refraction of the laser beams passing through the liquid electrolyte, the mirror constant (A_m) is acquired while the two reference mirrors are submerged in the electrolyte. The electrolyte alters the measured curvature following the relation,

$$\Delta\kappa = \frac{d - d_0}{d_0}\frac{1}{A_m}\left(\frac{n_{Ar}}{n_e}\right) \tag{4.3}$$

where n_{Ar} and n_e are the refractive indices of Argon and the electrolyte, respectively

[46]. The inferred value of n_e from the increase in MOS curvature measurements is consistent with reports of the refractive indices of the electrolyte to be ∼1.4 [46, 100].

After each experiment, the gaskets are replaced and the cell is sonicated in anhydrous methanol and allowed to fully dry to prevent moisture contamination in subsequent experiments. Since matching the time stamps of the microscope images to the MOS and electrochemical measurements is a critical step in this technique, the local times of each computer – one controlling the potentiostat and the other controlling the microscope images and MOS measurements – are periodically synchronized with each other and are never more than 30 seconds apart during the experiments.

4.5 Results

4.5.1 Initial Lithiation Behavior

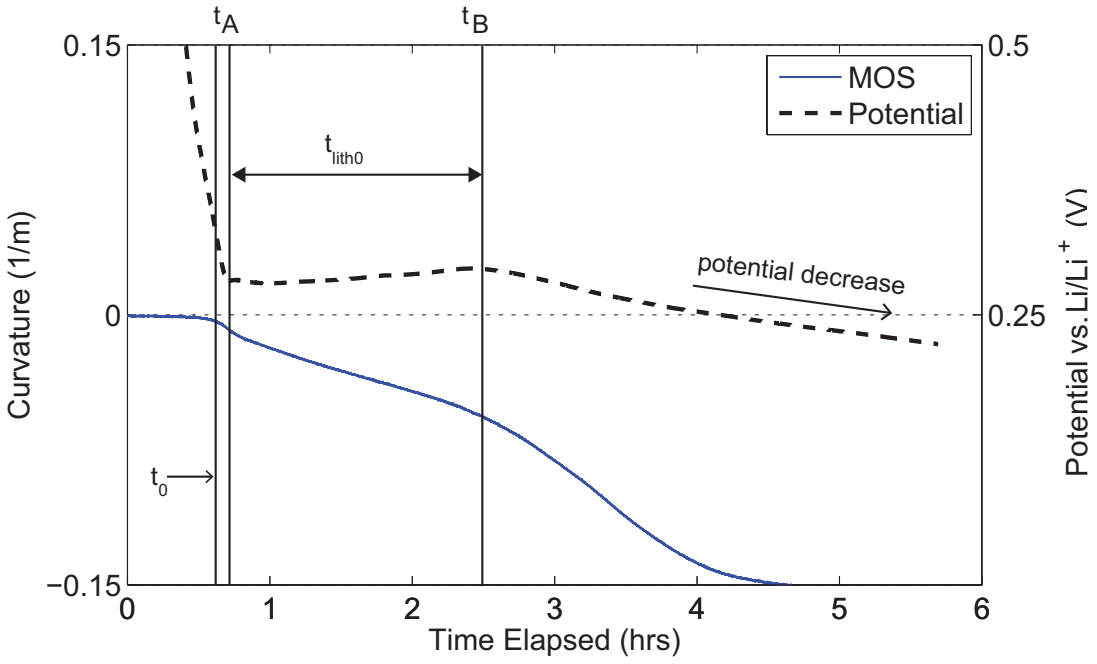

Figure 4.6: Initial lithiation behavior of silicon electrodes.

During initial lithiation, the potential of the Li-Si half-cell drops from an OCP of

$\sim$3 V to $\sim$0.3 V, where it plateaus for some time (t_{lith0}) before gradually decreasing to the lower cutoff potential (Figure 4.6). A front originating from the crack propagates outward starting from $t = t_A$ and eventually fades in with the rest of the bulk at $t = t_B$ (Figure 4.7d).

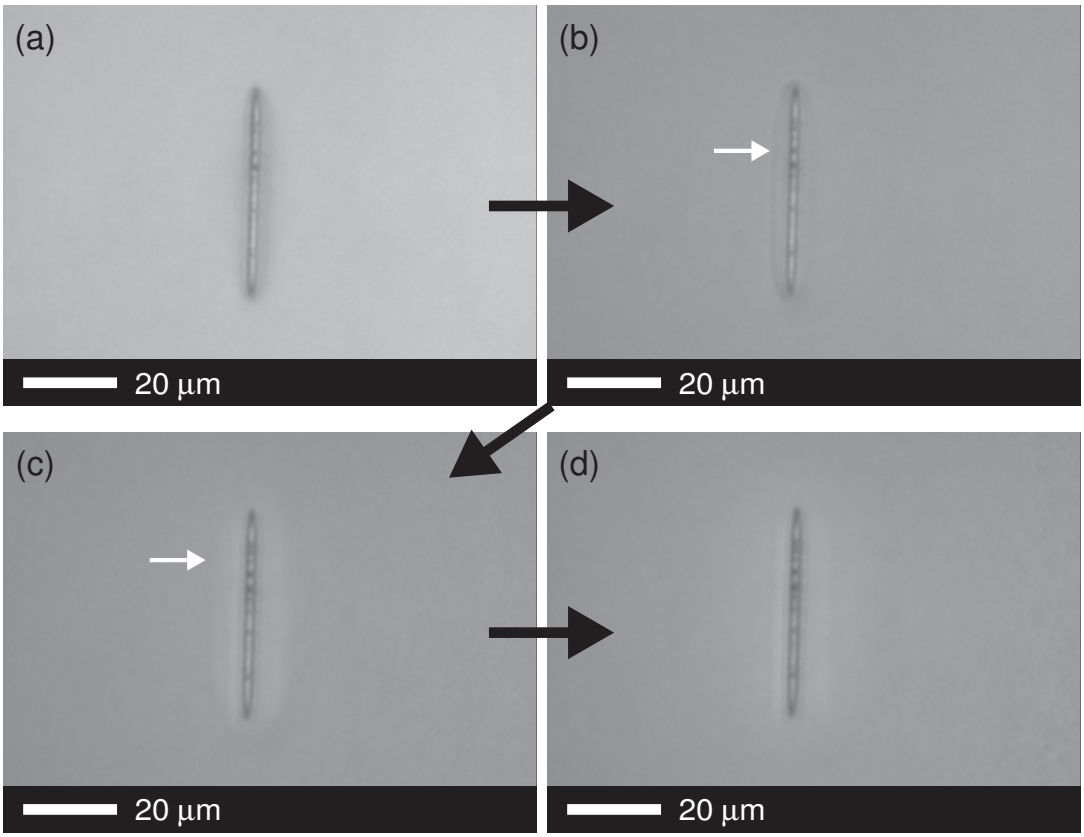

Figure 4.7: Microscope images of a front propagating from the crack during t_{lith0}. The white arrow indicates the position of the front. The front disappears at $t = t_B$ in (d).

Since a voltage plateau indicates a two-phase system with a moving phase boundary, this front may be interpreted as an a-Li$_x$Si phase boundary propagating into the a-Si film as observed in recent in situ TEM experiments [79, 80]. The disappearance of the front and gradual decrease of cell potential suggests that the film begins to lithiate uniformly throughout the electrode for $t > t_B$.

The curvature of the substrate remains unchanged above 0.3 V before decreasing linearly with time at $t = t_0$. t_0 is taken to be at the intersection of the initial curvature change with the initially flat curvature (Figure 4.8). Also note how the curvature of

the sample in Figure 4.8 begins to evolve prior to the cell potential reaching the voltage plateau at $t = t_A$ by over 400 seconds.

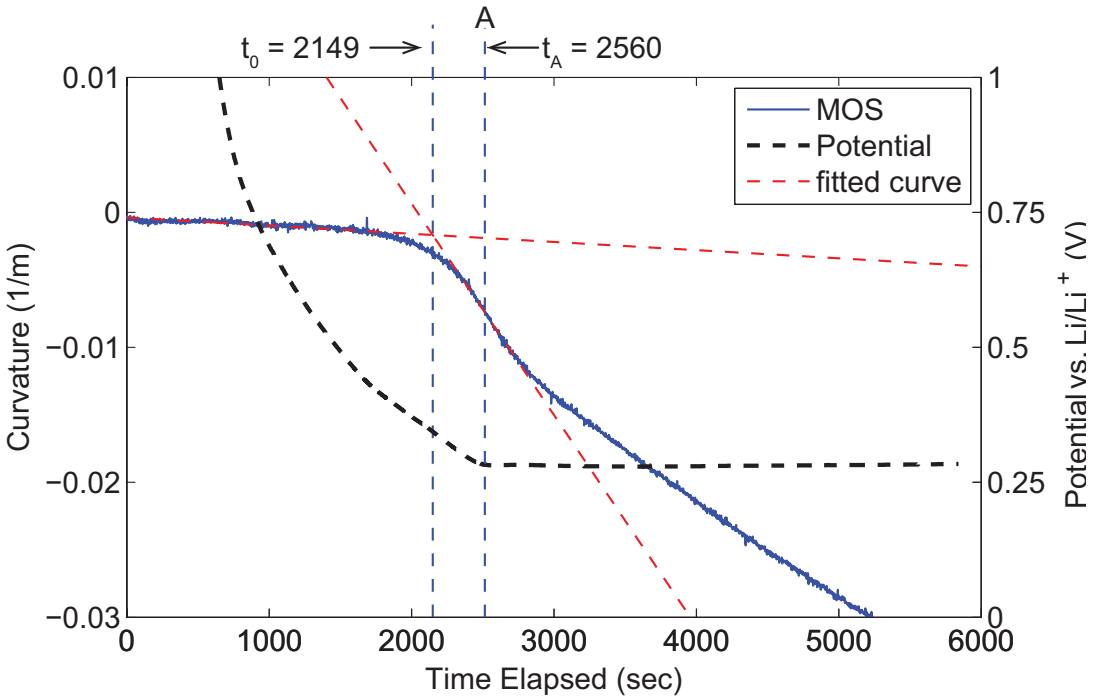

Figure 4.8: Calculating t0 from the slope of the MOS curvature.

Recall from Equation 2.8 that the substrate curvature is analogous to the stress-thickness of the film. Assuming that the film thickness does not noticeably change prior to phase transformation and that stresses due to SEI formation are negligible [46], the premature change in curvature of the substrate shows the silicon film taking in some finite amount of Li that induces a state of stress in the film prior to phase transformation. Furthermore, the change in slope of the curvature at around $t = 3000 > t_A$ in Figure 4.8 may be caused by the change in film thickness from phase transformation.

4.5.2 *In situ* Observations and Crack Propagation

Figure 4.9 shows the stress-thickness and cell potential data set for a sample with initial thickness of 343 nm. As the Si film continues to lithiate, the compressive stress

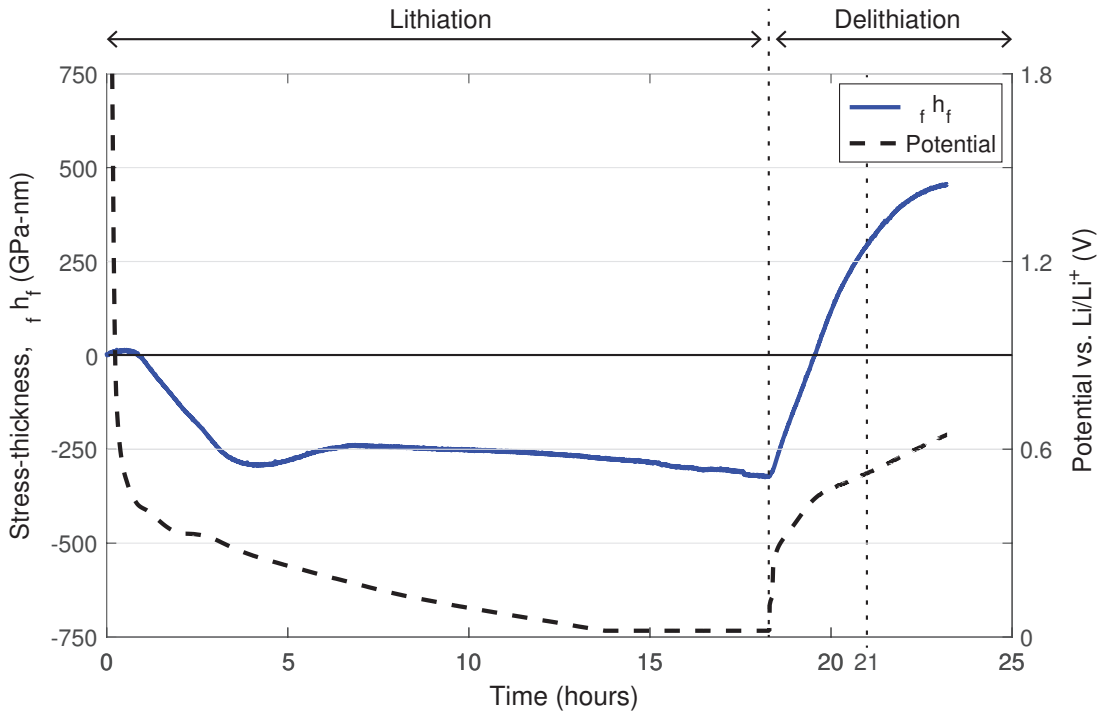

Figure 4.9: Stress-thickness and cell potential vs. elapsed time of a sample of initial thickness ${h_f}^0 = 343$ nm. The crack propagates from the initial crack at $t_c = 20{:}57$ based on the time stamp of the microscope images in Figure 4.10.

in the film increases until it reaches its yield stress, after which it plastically flows until the end of lithiation. Volume expansion in the film is observed in the microscope images as a change in the distance between the focal planes of the sample surface and bottom of the crack. At low Li concentrations, the depth of field of the microscope is sufficient to observe both surfaces (Figure 4.7), while only the top surface is in focus in images recorded at higher Li concentrations (Figure 4.10a). Upon delithiation, the silicon film unloads elastically and the film stress becomes increasingly tensile as the removal of lithium induces volume contraction in the film. Further delithiation induces plastic flow beyond its yield stress, which increases as the removal of Li causes the electrode to harden. As the film thickness decreases, the film surface and the bottom of the crack once again return to the focal plane of the microscope (Figure 4.10b).

As a result of the tensile stress in the film during delithiation, a crack propagates

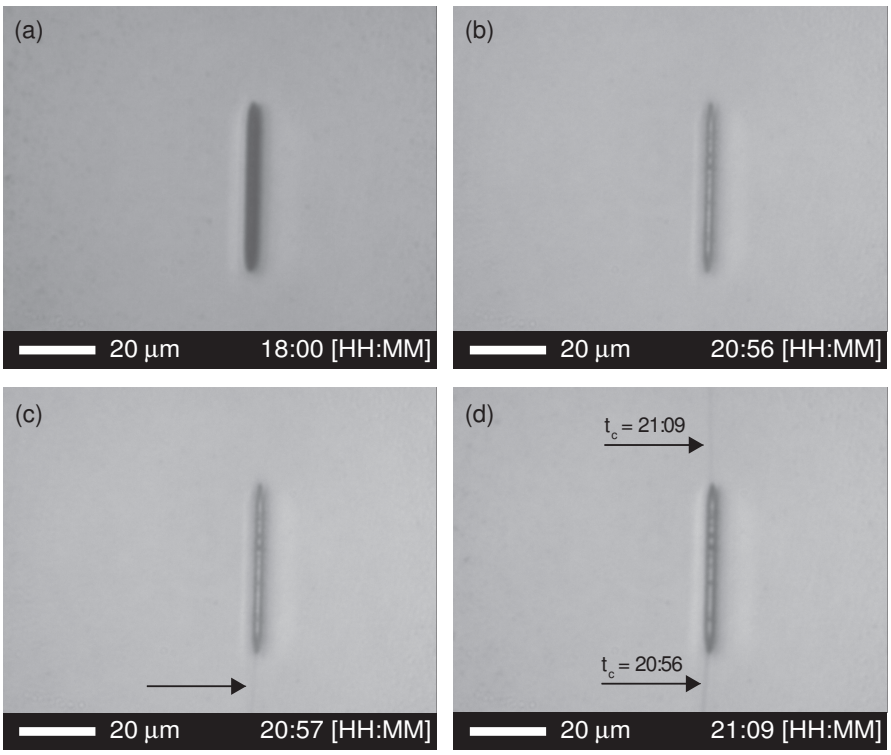

Figure 4.10: Microscope images of the pre-crack corresponding to data presented in Figure 4.9. (a) Volume expansion of the film causes the bottom of the crack to leave the field of view of the microscope while it is focused on the top surface. (b) Upon sufficient delithiation, the film thickness decreases enough to see both surfaces. (c) The crack propagates from the bottom edge of the initial crack between 20:56 and 20:57. (d) A second crack propagates from the top edge 13 minutes later. The differences in the stress and SOC between the two events were negligible, yielding similar fracture energy values.

from the initial flaw once the critical conditions to drive the crack are satisfied (Figure 4.10c); a second channel crack typically propagates from the opposite edge soon after (Figure 4.10d). The MOS curvature (κ_c) and charge (Q_c) correlating to the time stamp of these events (t_c) are then used to calculate G_c. As delithiation continues and the film continues to contract, additional cracks are formed while the existing channel cracks widen as a result of an interfacial sliding mechanism between the Si and Cu films [45, 46, 48, 49, 96] until a sufficient amount of lithium has been removed and the stress in the film increases rapidly. This is followed by a rapid decrease in stress that corresponds to the formation of high density crack patterns. In samples

where the initial film thickness is sufficiently high or there is poor adhesion to the substrate, delamination of the film may also occur. Conversely, crack propagation is not observed in samples with sufficiently low initial film thicknesses (i.e., below ~100 nm).

4.5.3 Dependence of Fracture Energy with SOC

Equations 4.1 and 4.2 show that the steady state energy release rate of a channel crack in a thin film (G_{SS}) is a function of film stress (σ_f), film thickness (h_f) and the elastic constants of the film and substrate. The film stress and thickness are calculated following the procedure discussed in Section 2.4.2. Although experimental values of the biaxial modulus (M_f) are available, decoupling E_f and v_f from M_f may introduce additional uncertainties to the calculations. Instead, $\overline{E_f}$ is calculated using the elastic constants from Shenoy *et al.*'s AIMD simulations [83], which are given as a function of Li composition (x) as,

$$E_f = \frac{18.9x + 90.13}{1 + x}, \qquad v_f = \frac{0.24x + 0.28}{1 + x} \tag{4.4}$$

Similarly, the shear moduli of the film (μ_f) are also calculated using Equation 4.4. Recent experiments reporting the elastic moduli of lithiated silicon using nanoindentation show good agreement with elastic moduli values from Equation 4.4 for all x [101, 102].

The elastic constants of the film and substrate are then used to calculate the Dundurs parameters (α and β) from Equation 4.2. For physically admissible values of α and β, Beuth provides tabulated values of $g(\alpha, \beta)$ [98], which show stronger dependence on α than β 4.11.

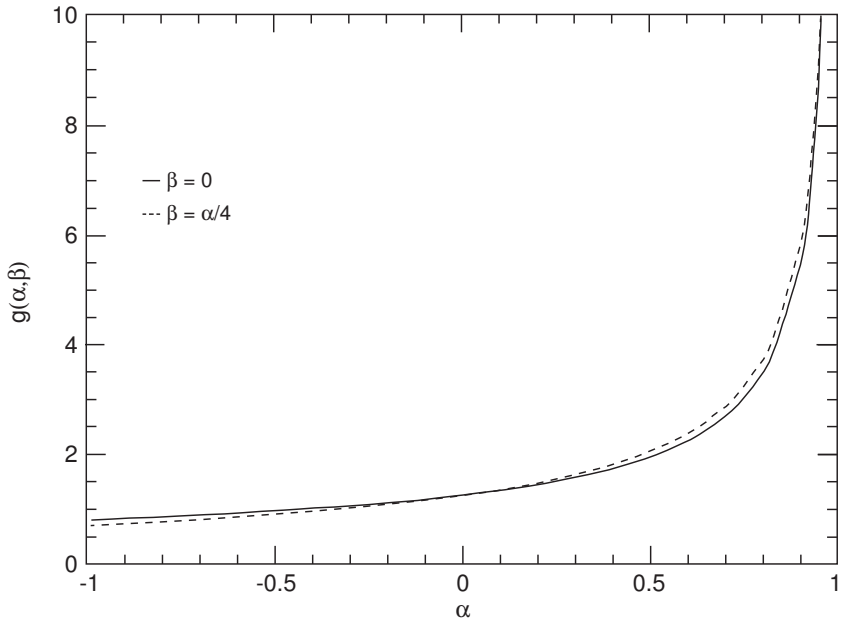

Figure 4.11: $g(\alpha, \beta)$ for typical values of α and β shows strong dependence on α moreso than on β. Reprinted from Ref. [98] with permission.

4.5.4 Calculating SOC

Since the elastic constants and film thickness (and consequently, the film stress) are influenced by the Li content of the film, large errors can be introduced to the fracture energy calculations if the Li content in the Si film is not properly accounted for. Recall from Section 2.4.2 that the Li content in the Si electrode is calculated with the assumption that Q_{delith} represents the maximum charge contained in the electrode (Q_{max}). However, there are some samples where delamination of the film occurs before the film fully delithiates. Consequently, further refinement of the charge data is necessary to obtain a consistent measure of the Si electrode's state of charge.

Table 4.1 summarizes Q_{loss} for samples of varying thicknesses that do not form cracks or delaminate during the first cycle. Although the average Q_{loss} per unit area of Si (A_f) is nearly twice the value reported by Nadimpalli *et al.* [41], it appears to be consistent across these samples. Assuming experimental conditions are consistent across all samples presented in this chapter, the irreversible loss for a given sample is taken to be, $\overline{Q_{loss}} = 0.196 A_f$. The maximum charge of the electrode is then,

Table 4.1: Breakdown of SEI loss per unit area of Si film for fracture energy samples. Units of charge (Q) are in Coulombs and units of area are in cm^2.

Sample	Q_{lith}	Q_{delith}	Q_{loss}	A_f	$Q_{loss}/area$
1	1.6397	1.1288	0.5109	2.476	0.20634
2	1.5802	1.2338	0.3464	1.997	0.17346
3	1.2651	0.7828	0.4823	2.014	0.23947
4	0.6696	0.3278	0.3418	2.088	0.16370
5	1.7939	1.3327	0.4612	2.096	0.22003
6	0.8985	0.5361	0.3624	2.116	0.17126
1	1.0244	0.6132	0.4112	2.089	0.19684
				Average (St. Dev):	0.196 ± 0.026

$Q_{max} = Q_{lith} - \overline{Q_{loss}}$. Taking the irreversible loss to occur at a fixed rate and only during lithiation, the effective charge of the electrode (Q_{eff}) is modeled as,

$$Q_{eff} = \begin{cases} \left(\frac{Q_{max}}{Q_{lith}}\right) Q, & \text{during lithiation} \\ Q, & \text{during delithiation} \end{cases} \tag{4.5}$$

where $Q = \int I \, \mathrm{d}t$ was defined earlier in Section 2.4.2. The steps to calculate the capacity (C) from Q_{eff} also follow the procedures outlined in Section 2.4.2. The consistency between stress vs. capacity curves from samples from this study (Figure 4.12) suggests that this method of SOC correction will yield consistent values for the fracture energy.

Interestingly, not all samples are able to reach full lithiation during these experiments, possibly due to stress-potential effects and variations in the cell impedance. For instance, sample FT082 (initial thickness ${h_f}^0 = 343$ nm) only reaches a capacity of 2200 mAh/g (Figure 4.12) after about 15 hours of constant current lithiation and a 3 hour potentiostatic hold (Figure 4.9). Using the preceding SOC correction protocol, the stress profile remains consistent with other samples.

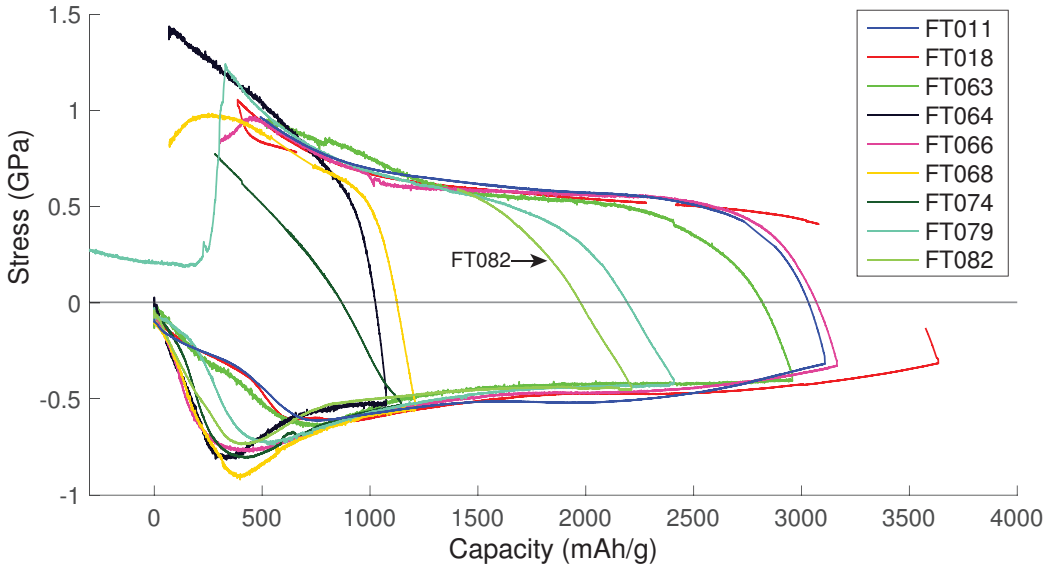

Figure 4.12: Compliation of stress vs. capacity curves using Q_{eff} to model SOC.

4.5.5 Fracture Energy of Lithiated Silicon

A cumulative plot of the fracture energies of lithiated silicon (G_c) for a range of Li compositions (x) is shown in Figure 4.13. For reference, the fracture energies of unlithiated silicon ($x = 0$) are also included using fracture toughness values (K_{IC}) of crystalline and polycrystalline silicon [103] with their respective elastic moduli [61, 104, 105]. The relation between the fracture toughness and fracture energy for plane stress is given as [106],

$$G_c = \frac{{K_{IC}}^2}{E} \tag{4.6}$$

Measurements reported in this chapter (blue diamonds) at lower Li content give values of G_c between 5.4 J/m^2 at $x = 0.4$ to 8 J/m^2 at $x = 1$, which are consistent with values of unlithiated silicon and those reported in recent experiments [42, 46, 97]. Nadimpalli reports an upper bound of the fracture energy at $x = 0.4$ to be between 9-11 J/m^2 (yellow triangle), while Pharr reports values of 8.5 ± 4.3 J/m^2 at $x = 0.7$.

Fracture energies at higher Li content are less consistent, ranging from 3.84 J/m^2 at $x = 1.7$ to 10.5 J/m^2 at $x = 2.3$, which are comparable to those reported by Pharr

$(5.4 \pm 2.2$ J/m^2 at $x = 2.7)$.

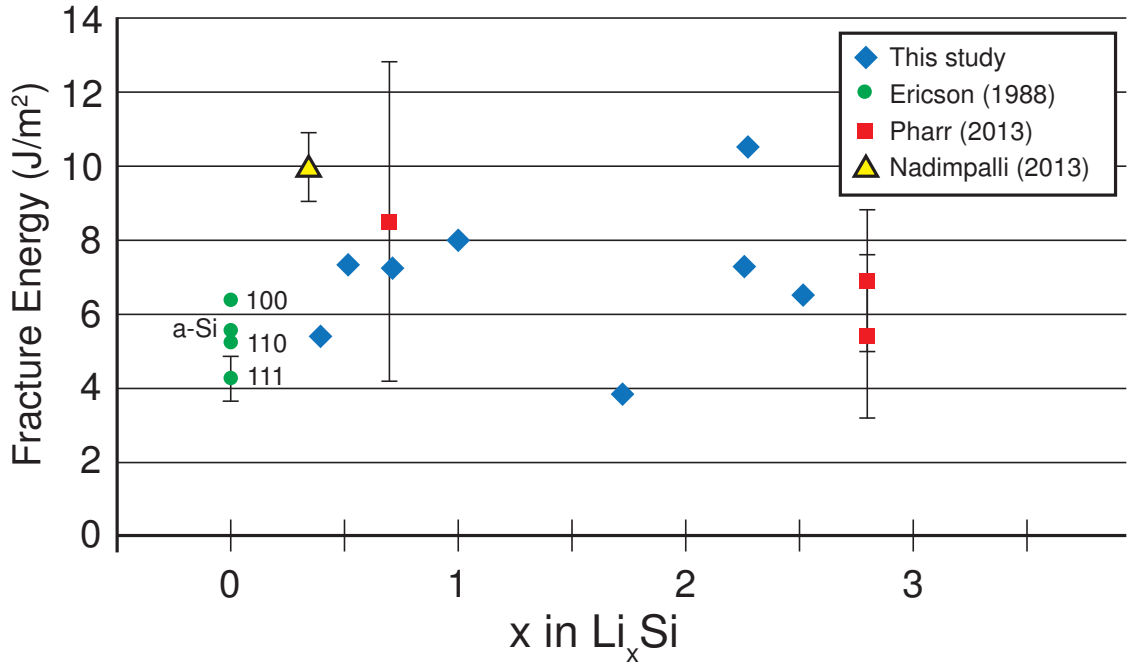

Figure 4.13: Cumulative plot of fracture energy (G_c) as a function of Li concentration (x).

4.6 Discussion

A key observation from the microscope images is the speed of the crack front during crack initiation. Although lithiated silicon exhibits extensive plastic deformation during cycling and undergoes elastic softening at higher Li content, Pharr et al. argues that the lithiated silicon is essentially elastic during the fracture process if the crack moves sufficiently faster than the mechanisms involved with plastic deformation [46]. Using low magnification objectives, the crack fronts in these experiments are seen to travel at beyond the field of view of the microscope (up to 100 µm) during the 60 seconds between consecutive images. In such a case, the linear elastic analysis by Beuth is valid for calculating the fracture energy of this material.

It should be noted, however, that the analysis by Beuth only considers the steady

Table 4.2: Comparison of fracture energy values assuming rigid substrate (Beuth) and interfacial sliding (Haftbaradaran). Units in the middle and right columns are J/m^2.

Li composition (x)	Rigid Substrate [98]	Interfacial Sliding [96]
0.39	5.41	8.70
0.52	7.35	17.93
0.71	7.26	14.10
1.00	7.97	23.69
1.72	3.84	3.99
2.26	7.31	28.17
2.27	10.54	19.01
2.53	6.53	13.32

state energy release rate of a thin film bonded to an elastic substrate. In practice, the silicon films used in this chapter and in many other studies [15, 45, 48–50, 107] utilize a copper underlayer that provides uniform current density to the electrode. The copper layer is thought to mitigate delamination of silicon films, thereby improving anode capacity and durability [15, 107]. However, given that the yield stress of copper is an order of magnitude lower than the flow stress of lithiated silicon (∼70 MPa), plastic flow of the copper underlayer surrounding the crack is expected. Furthermore, combined density functional theory and AIMD simulations by Stournara *et al.* [108] suggest lithium can facilitate sliding at the interface between the silicon film and substrate.

To account for these effects, Haftbaradaran *et al.* [96] incorporates these phenomena into an "interfacial sliding" mechanism and proposes the following condition for steady state crack growth,

$$\frac{1}{3\tau_0}\frac{h_f {\sigma_f}^3}{\overline{E_f}} \geq G_c \tag{4.7}$$

where τ_0 is the sliding strength of the interface, measured experimentally to be ∼40 MPa [50, 109]. Using this model, the fracture energies of the lithiated silicon system

can be 2–3 times higher than those presented in Figure 4.13 (Table 4.2).

4.7 Conclusion

This chapter demonstrates an experimental method used to determine the critical material properties of a lithiated silicon film at the onset of fracture. A crack is introduced to a thin film silicon electrode, which is then cycled in an electrochemical cell that allows concurrent in situ MOS measurements and microscope imaging. A front propagating from the crack surface coinciding with a voltage plateau during initial lithiation is observed, presumably due to a moving a phase boundary. Since the change in stress and SOC is negligible within that time frame, the exact conditions at crack propagation from the microscope images taken at 60 second intervals.

To account for SEI loss in the calculations, a method to correct for irreversible losses is presented. This method is demonstrated to yield consistent stress profiles across multiple thin film silicon electrode samples. The fracture energy (G_c) of lithiated silicon is then calculated from the critical material properties using the corrected SOC values and values of G_c over a range of SOCs are reported. These values are consistent with previously reported values using Beuth's analysis of the steady state energy release rate of a thin film bonded to an elastic substrate. The fracture energies are also calculated using models that incorporate interfacial sliding mechanisms. These models predict fracture energies 2–3 times higher than those given by rigid substrate models.

Appendix A

Fabrication Recipes

A.1 Solvent Clean

This process uses a series of solvent baths to remove particles and organic residue from the wafer substrates. This protocol is used prior to thin film deposition avoid pinhole defects from forming during deposition.

1. Sonicate sample in a beaker of acetone for 10 minutes
2. Transfer sample into a beaker of methanol and sonicate for 10 minutes
3. Transfer sample into a beaker of isopropanol and sonicate for 10 minutes
4. Remove samples and rinse in deionized water
5. Air dry with nitrogen

A.2 RCA-1 Clean

This procedure was adapted from Ref [110]. The RCA-1 clean is a standard technique in MEMS and microfabrication facilities to remove organic residue from silicon wafers. A thin film of silicon oxide is formed during this process; etching away this film reveals a pure silicon surface.

1. Heat 15 mL of NH_4OH to 90°C on a hotplate
2. Add 5 mL of H_2O_2 to the heated solution. Bubbles should begin to appear (similar to soda water)
3. Place silicon samples into the solution for 5 minutes
4. Remove sample and rinse in DI water
5. Etch away oxide layer with BHF solution (1:1 by volume BHF:DI water) for 1 minute
6. Remove silicon sample and rinse in DI water
7. Repeat steps 3-6 2 more times (3 total)
8. Blow dry with air gun as quickly as possible to minimize oxide layer formation

A.3 FIB Milling of Pre-crack

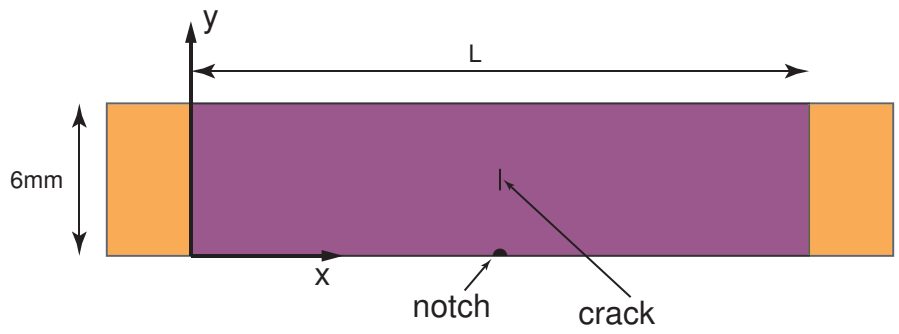

Figure A.1: Positions of pre-crack and notch in thin film silicon electrode samples. Not to scale.

Focused ion beam (FIB) milling is used to introduce microscale cracks to a thin film silicon electrode for fracture energy experiments (Chapter 4). This protocol is designed for the FEI Helios Nanolab.

1. Mount samples onto SEM stage using double-sided carbon tape with silicon-side up. Two samples (6 mm wide strips) can typically fit onto a 1 inch aluminum SEM stage.
   (a) Include one dummy sample for fine tuning extraction current and dwell time
2. (Optional) Use strips of tape to reduce adhesive strength to avoid delamination of copper layer on the back side of the sample.
3. (Optional) Ground the samples to the SEM stage to avoid charge buildup on the sample surface.
4. Place samples into the processing chamber and pump down the chamber
5. Once chamber is pumped, use the SEM to locate the dummy sample
6. Mill the pre-crack using the BITMAP template (Figure A.2)
7. Check the milled feature and adjust the extraction current and dwell time so that the crack is milled through the thickness of the film without going through the underlying copper layer.
8. Repeat steps (6) and (7) as many times necessary.
9. Move to the center of one of the edges of the samples (e.g., $x = L/2$, y =3 mm)
10. Mill a circular notch at the edge with the ion beam. This allows us to verify that the ion beam is properly focused while simultaneously providing a marker for locating the crack with the inverted microscope
11. Move the sample to y =3 mm and check for imperfections in the film using the SEM

12. (Optional) If pinhole defects or particles are in the field of view, move to an area free of defects. Avoid using the ion beam to image the surface, as it will alter the composition of the film

13. Use the parameters from (7) to mill the crack into the silicon film

14. Repeat Steps (9)–(13) for all samples

Figure A.2: Bitmap image of the pre-crack template. The RGB values at every pixel prescribe the dwell time (0..255) for the ion mill; black areas correspond to no milling involved.

Appendix B

Design of Electrode for Stress-Potential Experiments

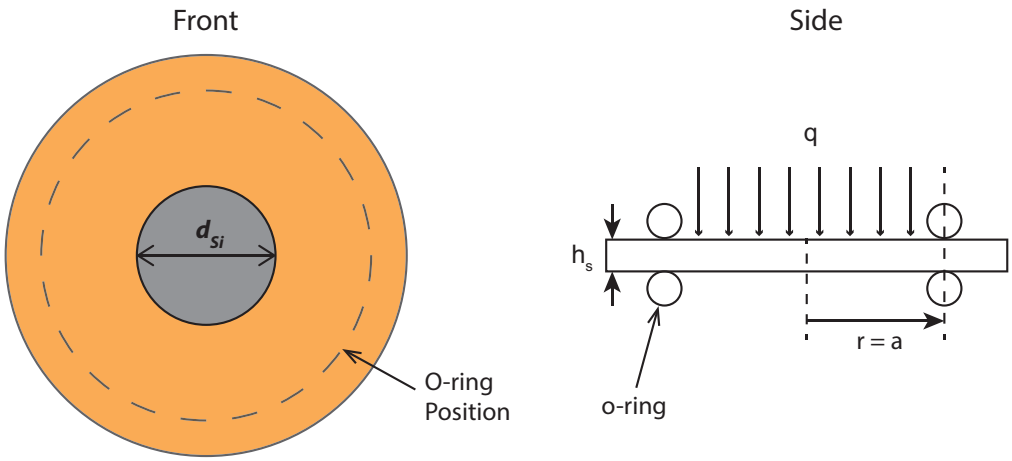

Figure B.1: Stress-potential wafer sample modeled as a circular plate with clamped edges at $r = a$ with an applied distributed load, q.

The wafer substrate is modeled as a circular plate with clamped boundary conditions at $r = a$ under uniform, distributed load, q. Setting $r = 0$ to be at the center of the substrate, its curvature due to an applied pressure is taken from linear elastic plate bending theory [111],

$$\kappa(r) = \frac{qa^2}{16D}\left(c_0 - \frac{3r^2}{a^2}\right) \tag{B.1}$$

where $1 \leq c_0 \leq \frac{3+\nu}{1+\nu}$ depends on the applied moment at $r = a$ due to the clamping force of the o-rings. Taking $\nu = 0.17$ for a fused silica wafer, $c_0 = 1$ corresponds to simply supported (no moment) and $c_0 = 2.7$ corresponds to rigidly clamped boundary conditions at $r = a$. D is the flexural rigidity of the substrate and is given as,

$$D = \frac{E_s {h_s}^3}{12(1 - {\nu_s}^2)} \tag{B.2}$$

where the subscript "s" corresponds to the properties of the substrate. Taking E_s = 71.7 GPa and a =18.9 mm to be the diameter of the o-rings, Figure B.2 plots the maximum variation in strain within the silicon electrode as a function of c_0. As an example, a silicon electrode of diameter d_{Si} =6 mm at a clamping force equivalent to $c_0 = 1.5$ will have a maximum strain variation of 5% at the outer edge of the electrode. A higher clamping force results in lower strain variations in the silicon film. Allowing for a maximum of 10% strain variation (blue curve in Figure B.2), the diameter of the electrode is set to d_{Si} =8 mm. Experimentally measured values of c_0 ranged from $c_0 = 1$ to $c_0 = 1.4$.

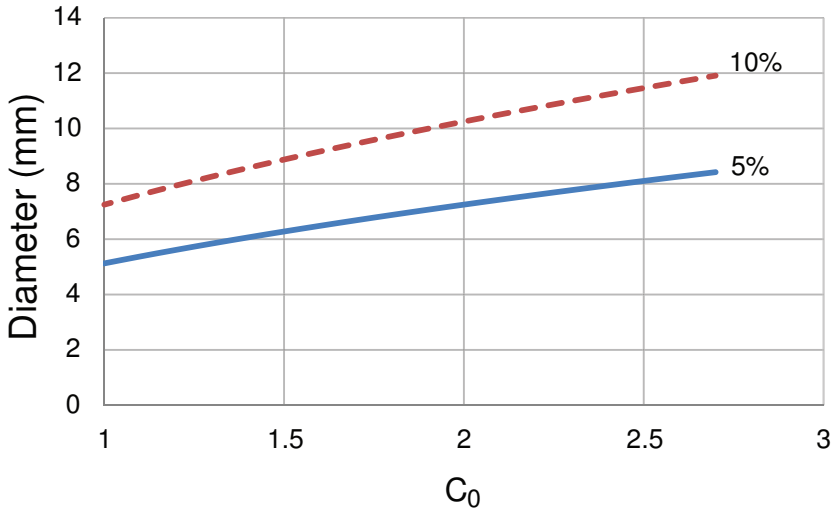

Figure B.2: Silicon electrode diameter design considerations.

Bibliography

[1] Alexander Del Regno and Axel Vartmann. *Press release*. Tech. rep. Zentrum für Sonnenenergie und Wasserstoff-Forschung, June 2015.

[2] R. Garcia-Valle and J.A. Pecas Lopes. *Electric Vehicle Integration into Modern Power Networks*. Ed. by Rodrigo Garcia-Valle and João A. Peças Lopes. New York, NY: Springer New York, 2013. ISBN: 978-1-4614-0133-9. DOI: 10.1007/978-1-4614-0134-6.

[3] Héctor D. Abruña, Yasuyuki Kiya, and Jay C. Henderson. "Batteries and electrochemical capacitors". In: *Physics Today* 61.12 (2008), p. 43. ISSN: 00319228. DOI: 10.1063/1.3047681.

[4] Alvaro Mendoza and Juan Argueta. *GM EV1 Performance Characterization*. Tech. rep. April. Idaho National Laboratoy, 2000.

[5] EVAmerica. *1999 GENERAL MOTORS EV1 with NiMH*. Tech. rep. Idaho National Laboratory, 1999.

[6] INL. *2011 Nissan Leaf - VIN 0356 Advanced Vehicle Testing - Baseline Testing Results*. Tech. rep. U.S. Department of Energy, 2011, pp. 1–5.

[7] USNews. *2011 Nissan Leaf Reviews, Pictures and Prices*. 2011.

[8] *2015 Tesla Model S AWD - 85D*. 2015.

[9] L. David Roper. *Tesla Model S*. 2015.

[10] H. Yamin et al. "Lithium Sulfur Battery". In: *Journal of The Electrochemical Society* 135.5 (1988), p. 1045. ISSN: 00134651. DOI: 10.1149/1.2095868.

[11] Xiulei Ji, Kyu Tae Lee, and Linda F. Nazar. "A highly ordered nanostructured carbon-sulphur cathode for lithium-sulphur batteries". In: *Nature Materials* 8.6 (June 2009), pp. 500–506. ISSN: 1476-1122. DOI: 10.1038/nmat2460.

[12] Xiao Liang et al. "A nano-structured and highly ordered polypyrrole-sulfur cathode for lithium–sulfur batteries". In: *Journal of Power Sources* 196.16 (Aug. 2011), pp. 6951–6955. ISSN: 03787753. DOI: 10.1016/j.jpowsour.2010.11.132.

[13] M. N. Obrovac and Leif Christensen. "Structural Changes in Silicon Anodes during Lithium Insertion/Extraction". In: *Electrochemical and Solid-State Letters* 7.5 (2004), A93. ISSN: 10990062. DOI: 10.1149/1.1652421.

[14] U Kasavajjula, C Wang, and A. John Appleby. "Nano- and bulk-silicon-based insertion anodes for lithium-ion secondary cells". In: *Journal of Power Sources* 163.2 (Jan. 2007), pp. 1003–1039. ISSN: 03787753. DOI: 10.1016/j.jpowsour.2006.09.084.

[15] J. P. Maranchi, a. F. Hepp, and P. N. Kumta. "High Capacity, Reversible Silicon Thin-Film Anodes for Lithium-Ion Batteries". In: *Electrochemical and Solid-State Letters* 6.9 (2003), A198. ISSN: 10990062. DOI: 10.1149/1.1596918.

[16] Candace K. Chan et al. "High-performance lithium battery anodes using silicon nanowires." In: *Nature nanotechnology* 3.1 (2008), pp. 31–35. ISSN: 1748-3387. DOI: 10.1038/nnano.2007.411.

[17] Bo Gao et al. "Alloy Formation in Nanostructured Silicon". In: *Advanced Materials* 13.11 (June 2001), pp. 816–819. ISSN: 09359648. DOI: 10.1002/1521-4095(200106)13:11<816::AID-ADMA816>3.0.CO;2-P.

[18] Kuiqing Peng et al. "Ordered silicon nanowire arrays via nanosphere lithography and metal-induced etching". In: *Applied Physics Letters* 90.16 (2007), pp. 1–4. ISSN: 00036951. DOI: 10.1063/1.2724897.

[19] Kuiqing Peng et al. “Silicon nanowires for rechargeable lithium-ion battery anodes”. In: *Applied Physics Letters* 93.3 (2008), p. 033105. ISSN: 00036951. DOI: 10.1063/1.2929373. arXiv: arXiv:1011.1669v3.

[20] Mino Green et al. “Structured Silicon Anodes for Lithium Battery Applications”. In: *Electrochemical and Solid-State Letters* 6.5 (2003), A75. ISSN: 10990062. DOI: 10.1149/1.1563094.

[21] Heon-Cheol Shin et al. “Porous silicon negative electrodes for rechargeable lithium batteries”. In: *Journal of Power Sources* 139.1-2 (2005), pp. 314–320. ISSN: 03787753. DOI: 10.1016/j.jpowsour.2004.06.073.

[22] M. N. Obrovac and L. J. Krause. “Reversible Cycling of Crystalline Silicon Powder”. In: *Journal of The Electrochemical Society* 154.2 (2007), A103. ISSN: 00134651. DOI: 10.1149/1.2402112.

[23] Ji Heon Ryu et al. “Failure Modes of Silicon Powder Negative Electrode in Lithium Secondary Batteries”. In: *Electrochemical and Solid-State Letters* 7.10 (2004), A306. ISSN: 10990062. DOI: 10.1149/1.1792242.

[24] B. a. Boukamp. “All-Solid Lithium Electrodes with Mixed-Conductor Matrix”. In: *Journal of The Electrochemical Society* 128.4 (1981), p. 725. ISSN: 00134651. DOI: 10.1149/1.2127495.

[25] Nikolay Dimov, Yonggao Xia, and Masaki Yoshio. “Practical silicon-based composite anodes for lithium-ion batteries: Fundamental and technological features”. In: *Journal of Power Sources* 171.2 (Sept. 2007), pp. 886–893. ISSN: 03787753. DOI: 10.1016/j.jpowsour.2007.06.026.

[26] Wei-Ren Liu et al. “Enhanced Cycle Life of Si Anode for Li-Ion Batteries by Using Modified Elastomeric Binder”. In: *Electrochemical and Solid-State Letters* 8.2 (2005), A100. ISSN: 10990062. DOI: 10.1149/1.1847685.

[27] Nian Liu et al. “A yolk-shell design for stabilized and scalable li-ion battery alloy anodes.” In: *Nano letters* 12.6 (June 2012), pp. 3315–21. ISSN: 1530-6992. DOI: 10.1021/nl3014814.

[28] S Bourderau, T Brousse, and D.M Schleich. “Amorphous silicon as a possible anode material for Li-ion batteries”. In: *Journal of Power Sources* 81-82 (1999), pp. 233–236. ISSN: 03787753. DOI: 10.1016/S0378-7753(99)00194-9.

[29] Andreas Netz, Robert a. Huggins, and Werner Weppner. “The formation and properties of amorphous silicon as negative electrode reactant in lithium systems”. In: *Journal of Power Sources* 119-121 (2003), pp. 95–100. ISSN: 03787753. DOI: 10.1016/S0378-7753(03)00132-0.

[30] Pimpa Limthongkul et al. “Electrochemically-driven solid-state amorphization in lithium-silicon alloys and implications for lithium storage”. In: *Acta Materialia* 51.4 (Feb. 2003), pp. 1103–1113. ISSN: 13596454. DOI: 10.1016/S1359-6454(02)00514-1.

[31] Borae Bang et al. “Electrochemical properties of silicon deposited on patterned wafer”. In: *Journal of Power Sources* 156.2 (2006), pp. 604–609. ISSN: 03787753. DOI: 10.1016/j.jpowsour.2005.05.096.

[32] V. Baranchugov et al. “Amorphous silicon thin films as a high capacity anodes for Li-ion batteries in ionic liquid electrolytes”. In: *Electrochemistry Communications* 9.4 (2007), pp. 796–800. ISSN: 13882481. DOI: 10.1016/j.elecom.2006.11.014.

[33] J. Graetz et al. “Highly Reversible Lithium Storage in Nanostructured Silicon”. In: *Electrochemical and Solid-State Letters* 6.9 (2003), A194. ISSN: 10990062. DOI: 10.1149/1.1596917.

[34] Jason L. Goldman et al. “Strain Anisotropies and Self-Limiting Capacities in Single-Crystalline 3D Silicon Microstructures: Models for High Energy Density

Lithium-Ion Battery Anodes". In: *Advanced Functional Materials* 21.13 (July 2011), pp. 2412–2422. ISSN: 1616301X. DOI: 10.1002/adfm.201002487.

[35] Vijay A. Sethuraman et al. "In situ measurements of stress evolution in silicon thin films during electrochemical lithiation and delithiation". In: *Journal of Power Sources* 195.15 (Aug. 2010), pp. 5062–5066. ISSN: 03787753. DOI: 10.1016/j.jpowsour.2010.02.013.

[36] Vijay A. Sethuraman et al. "In situ measurement of biaxial modulus of Si anode for Li-ion batteries". In: *Electrochemistry Communications* 12.11 (Nov. 2010), pp. 1614–1617. ISSN: 13882481. DOI: 10.1016/j.elecom.2010.09.008.

[37] Vijay A. Sethuraman et al. "In Situ Measurements of Stress-Potential Coupling in Lithiated Silicon". In: *Journal of The Electrochemical Society* 157.11 (2010), A1253. ISSN: 00134651. DOI: 10.1149/1.3489378.

[38] Vijay A. Sethuraman, Venkat Srinivasan, and John Newman. "Analysis of Electrochemical Lithiation and Delithiation Kinetics in Silicon". In: *Journal of the Electrochemical Society* 160.2 (2013), A394–A403. ISSN: 0013-4651. DOI: 10.1149/2.008303jes.

[39] Michael J. Chon et al. "Real-Time Measurement of Stress and Damage Evolution during Initial Lithiation of Crystalline Silicon". In: *Physical Review Letters* 107.4 (July 2011), p. 045503. ISSN: 0031-9007. DOI: 10.1103/PhysRevLett.107.045503.

[40] Allan F. Bower, Pradeep Guduru, and Vijay A. Sethuraman. "A finite strain model of stress, diffusion, plastic flow, and electrochemical reactions in a lithium-ion half-cell". In: *Journal of the Mechanics and Physics of Solids* 59.4 (Apr. 2011), pp. 804–828. ISSN: 00225096. DOI: 10.1016/j.jmps.2011.01.003.

[41] Siva P.V. Nadimpalli et al. “Quantifying capacity loss due to solid-electrolyte-interphase layer formation on silicon negative electrodes in lithium-ion batteries”. In: *Journal of Power Sources* 215 (2012), pp. 145–151. ISSN: 03787753. DOI: 10.1016/j.jpowsour.2012.05.004.

[42] Siva P.V. Nadimpalli et al. “On Plastic Deformation and Fracture in Si Films during Electrochemical Lithiation/Delithiation Cycling”. In: *Journal of the Electrochemical Society* 160.10 (2013), A1885–A1893. ISSN: 0013-4651. DOI: 10.1149/2.098310jes.

[43] Siva P.V. Nadimpalli et al. “Stress Evolution in Lithium-Ion Composite Electrodes during Electrochemical Cycling and Resulting Internal Pressures on the Cell Casing”. In: *Journal of The Electrochemical Society* 162.14 (2015), A2656–A2663. ISSN: 0013-4651. DOI: 10.1149/2.0341514jes.

[44] Giovanna Bucci et al. “Measurement and modeling of the mechanical and electrochemical response of amorphous Si thin film electrodes during cyclic lithiation”. In: *Journal of the Mechanics and Physics of Solids* 62 (2014), pp. 276–294. ISSN: 00225096. DOI: 10.1016/j.jmps.2013.10.005.

[45] Sumit K. Soni et al. “Thickness effects on the lithiation of amorphous silicon thin films”. In: *Scripta Materialia* 64.4 (Feb. 2011), pp. 307–310. ISSN: 13596462. DOI: 10.1016/j.scriptamat.2010.10.003.

[46] Matt Pharr, Zhigang Suo, and Joost J. Vlassak. “Measurements of the fracture energy of lithiated silicon electrodes of Li-Ion batteries”. In: *Nano Letters* 13.11 (2013), pp. 5570–5577. ISSN: 15306984. DOI: 10.1021/nl403197m.

[47] Brian W. Sheldon et al. “Stress Contributions to Solution Thermodynamics in Li-Si Alloys”. In: *Electrochemical and Solid-State Letters* 15.1 (2012), A9. ISSN: 10990062. DOI: 10.1149/2.016201esl.

[48] Sumit K. Soni et al. “Diffusion Mediated Lithiation Stresses in Si Thin Film Electrodes”. In: *Journal of the Electrochemical Society* 159.9 (2012), A1520–A1527. ISSN: 0013-4651. DOI: 10.1149/2.009209jes.

[49] Sumit K. Soni et al. “Stress Mitigation during the Lithiation of Patterned Amorphous Si Islands”. In: *Journal of The Electrochemical Society* 159.1 (2012), A38. ISSN: 00134651. DOI: 10.1149/2.048201jes.

[50] Hamed Haftbaradaran et al. “Modified Stoney Equation for Patterned Thin Film Electrodes on Substrates in the Presence of Interfacial Sliding”. In: *Journal of Applied Mechanics* 79.3 (2012), p. 031018. ISSN: 00218936. DOI: 10.1115/1.4005900.

[51] Kyung Yoon Chung and Kwang-Bum Kim. “Investigation of Structural Fatigue in Spinel Electrodes Using In Situ Laser Probe Beam Deflection Technique”. In: *Journal of The Electrochemical Society* 149.1 (2002), A79. ISSN: 00134651. DOI: 10.1149/1.1426396.

[52] F. Decker et al. “A Comparison of the Electrochromic Behavior and the Mechanical Properties of WO[sub 3] and NiO[sub x] Thin Film Electrodes”. In: *Journal of The Electrochemical Society* 138.11 (1991), p. 3182. ISSN: 00134651. DOI: 10.1149/1.2085389.

[53] Joo-Young Go and Su-Il Pyun. “Investigation of Stresses Generated during Lithium Transport through the RF Sputter-Deposited Li[sub 1-δ]CoO[sub 2] Film by a DQCR Technique”. In: *Journal of The Electrochemical Society* 150.8 (2003), A1037. ISSN: 00134651. DOI: 10.1149/1.1584438.

[54] Győző G. Láng et al. “Simultaneous Oscillations of Surface Stress and Potential in the Course of Galvanostatic Oxidation of Formic Acid”. In: *The Journal of Physical Chemistry B* 104.13 (Apr. 2000), pp. 2785–2789. ISSN: 1520-6106. DOI: 10.1021/jp9942116.

[55] Su-il Pyun, Kwang-hoon Kim, and Jeong-nam Han. "Analysis of stresses generated during hydrogen extraction from and injection into Ni(OH)2/NiOOH film electrode". In: *Journal of Power Sources* 91 (2000), pp. 92–98.

[56] J. M. Rosolen and F. Decker. "Stress in Carbon Film Electrodes during Li[sup +] Electrochemical Intercalation". In: *Journal of The Electrochemical Society* 143.8 (1996), p. 2417. ISSN: 00134651. DOI: 10.1149/1.1837024.

[57] S. N. Sahu, J. Scarminio, and F. Decker. "A Laser Beam Deflection System for Measuring Stress Variations in Thin Film Electrodes". In: *Journal of The Electrochemical Society* 137.4 (1990), p. 1150. ISSN: 00134651. DOI: 10.1149/1.2086618.

[58] F Tian et al. "Observation of the surface stress induced in microcantilevers by electrochemical redox processes." In: *Ultramicroscopy* 100.3-4 (Aug. 2004), pp. 217–23. ISSN: 0304-3991. DOI: 10.1016/j.ultramic.2003.12.012.

[59] Kaoru Ueno, Su-Il Pyun, and M. Seo. "Stresses of a Titanium Thin-Film Electrode Generated during Anodic Oxidation by a Beam-Bending Method". In: *Journal of The Electrochemical Society* 147.12 (2000), p. 4519. ISSN: 00134651. DOI: 10.1149/1.1394095.

[60] GG Stoney. "The tension of metallic films deposited by electrolysis". In: *Proceedings of the Royal Society of London. Series A, ...* 82.553 (1909), pp. 172–175.

[61] L. B. Freund and S Suresh. *Thin Film Materials: Stress, Defect Formation and Surface Evolution*. 2003, p. 768. ISBN: 9780521529778. DOI: 10.1017/CBO9780511754715.

[62] Seung-Joo Lee et al. "Stress effect on cycle properties of the silicon thin-film anode". In: *Journal of Power Sources* 97-98 (July 2001), pp. 191–193. ISSN: 03787753. DOI: 10.1016/S0378-7753(01)00761-3.

[63] Győző G. Láng, N S Sas, and S Vesztergom. "Experimental Determination of Surface Stress Changes in Electrochemical Systems - Possibilities and Pitfalls". In: *Chemical and Biochemical Engineering Quarterly* 23.1 (2009), pp. 1–9.

[64] Győző G. Láng et al. "In situ monitoring of the electrochemical degradation of polymer films on metals using the bending beam method and impedance spectroscopy". In: *Electrochimica Acta* 73 (2012), pp. 59–69. ISSN: 00134686. DOI: 10.1016/j.electacta.2012.01.068.

[65] J. a. Floro et al. "Real-time stress evolution during Si1-xGex Heteroepitaxy: Dislocations, islanding, and segregation". In: *Journal of Electronic Materials* 26.9 (Sept. 1997), pp. 969–979. ISSN: 0361-5235. DOI: 10.1007/s11664-997-0233-2.

[66] Eric Chason and Brian W. Sheldon. "Monitoring Stress in Thin Films During Processing". In: *Surface Engineering* 19.5 (Oct. 2003), pp. 387–391. ISSN: 02670844. DOI: 10.1179/026708403225010118.

[67] Jae Shin and Eric Chason. "Compressive Stress Generation in Sn Thin Films and the Role of Grain Boundary Diffusion". In: *Physical Review Letters* 103.5 (July 2009), pp. 1–4. ISSN: 0031-9007. DOI: 10.1103/PhysRevLett.103.056102.

[68] L. Y. Beaulieu et al. "Colossal Reversible Volume Changes in Lithium Alloys". In: *Electrochemical and Solid-State Letters* 4.9 (2001), A137. ISSN: 10990062. DOI: 10.1149/1.1388178.

[69] N. Ding et al. "Determination of the diffusion coefficient of lithium ions in nano-Si". In: *Solid State Ionics* 180.2-3 (2009), pp. 222–225. ISSN: 01672738. DOI: 10.1016/j.ssi.2008.12.015.

[70] Riccardo Ruffo et al. "Impedance Analysis of Silicon Nanowire Lithium Ion Battery Anodes". In: *Journal of Power Sources* 189.2 (2009), pp. 11390–11398. ISSN: 03787753. DOI: 10.1016/j.jpowsour.2009.01.007.

[71] Erwin Hüger et al. “Lithium transport through nanosized amorphous silicon layers”. In: *Nano Letters* 13.3 (2013), pp. 1237–1244. ISSN: 15306984. DOI: 10.1021/nl304736t.

[72] J. Xie et al. “Li-ion diffusion in amorphous Si films prepared by RF magnetron sputtering: A comparison of using liquid and polymer electrolytes”. In: *Materials Chemistry and Physics* 120.2-3 (2010), pp. 421–425. ISSN: 02540584. DOI: 10.1016/j.matchemphys.2009.11.031.

[73] Matt Pharr et al. “Kinetics of initial lithiation of crystalline silicon electrodes of lithium-ion batteries.” In: *Nano letters* 12.9 (Sept. 2012), pp. 5039–47. ISSN: 1530-6992. DOI: 10.1021/nl302841y.

[74] T. D. Hatchard and J. R. Dahn. “In Situ XRD and Electrochemical Study of the Reaction of Lithium with Amorphous Silicon”. In: *Journal of The Electrochemical Society* 151.6 (2004), A838. ISSN: 00134651. DOI: 10.1149/1.1739217.

[75] M. N. Obrovac et al. “Alloy Design for Lithium-Ion Battery Anodes”. In: *Journal of The Electrochemical Society* 154.9 (2007), A849. ISSN: 00134651. DOI: 10.1149/1.2752985.

[76] Technical Glass Products. *Properties of Fused Quartz*. 2010.

[77] M. Adams. *Fused Silica - SiO2 Material Properties*. 2013.

[78] Yong Min Lee et al. “SEI Layer Formation on Amorphous Si Thin Electrode during Precycling”. In: *Journal of The Electrochemical Society* 154.6 (2007), A515. ISSN: 00134651. DOI: 10.1149/1.2719644.

[79] Matthew T. McDowell et al. “In Situ TEM of Two-Phase Lithiation of Amorphous Silicon Nanospheres”. In: *Nano letters* 13.2 (Mar. 2013), pp. 758–764. ISSN: 1530-6992. DOI: 10.1021/nl3044508.

[80] Jiang Wei Wang et al. “Two-phase electrochemical lithiation in amorphous silicon.” In: *Nano letters* 13.2 (Feb. 2013), pp. 709–715. ISSN: 1530-6992. DOI: 10.1021/nl304379k.

[81] Pimpa Limthongkul et al. “Electrochemically-driven solid-state amorphization in lithium-metal anodes”. In: *Journal of Power Sources* 119-121 (June 2003), pp. 604–609. ISSN: 03787753. DOI: 10.1016/S0378-7753(03)00303-3.

[82] L. Y. Beaulieu et al. “Reaction of Li with Alloy Thin Films Studied by In Situ AFM”. In: *Journal of The Electrochemical Society* 150.11 (2003), A1457–A1464. DOI: 10.1149/1.1613668.

[83] Vivek B. Shenoy, P. Johari, and Yue Qi. “Elastic softening of amorphous and crystalline Li-Si Phases with increasing Li concentration: A first-principles study”. In: *Journal of Power Sources* 195.19 (2010), pp. 6825–6830. ISSN: 03787753. DOI: 10.1016/j.jpowsour.2010.04.044.

[84] Wei-Ren Liu et al. “Effect of electrode structure on performance of Si anode in Li-ion batteries: Si particle size and conductive additive”. In: *Journal of Power Sources* 140.1 (2005), pp. 139–144. ISSN: 03787753. DOI: 10.1016/j.jpowsour.2004.07.032.

[85] Xin Su et al. “Silicon-Based Nanomaterials for Lithium-Ion Batteries: A Review”. In: *Advanced Energy Materials* 4.1 (2014), n/a–n/a. ISSN: 1614-6840. DOI: 10.1002/aenm.201300882.

[86] Francis Larché and John W. Cahn. “A Linear Theory of Thermochemical Equilibrium of Solids under Stress”. In: *Acta Metallurgica* 21 (1973), pp. 1051–1063. ISSN: 00016160. DOI: 10.1016/0001-6160(73)90021-7.

[87] Francis Larché and John W. Cahn. “A nonlinear theory of thermochemical equilibrium of solids under stress”. In: *Acta Metallurgica* 26 (1978), pp. 53–60. ISSN: 00016160. DOI: 10.1016/0001-6160(78)90201-8.

[88] Francis Larché and John W. Cahn. "The effect of self-stress on diffusion in solids". In: *Acta Metallurgica* 30 (1982), pp. 1835–1845.

[89] Francis Larché and John W. Cahn. "The Interactions of Composition and Stress in Crystalline Solids". In: *Journal of Research of the National Bureau of Standards* 89.3 (1984), p. 467. ISSN: 0160-1741. DOI: 10.6028/jres.089.026.

[90] O. Renner and J. Zemek. "Density of amorphous silicon films". In: *Czechoslovak Journal of Physics* 23.11 (1973), pp. 1273–1276. ISSN: 00114626. DOI: 10.1007/BF01591210.

[91] Allan F. Bower et al. "A continuum model of deformation, transport and irreversible changes in atomic structure in amorphous lithium-silicon electrodes". In: *Acta Materialia* 98 (Oct. 2015), pp. 229–241. ISSN: 13596454. DOI: 10.1016/j.actamat.2015.07.036.

[92] Loïc Baggetto et al. "High energy density all-solid-state batteries: A challenging concept towards 3D integration". In: *Advanced Functional Materials* 18.7 (2008), pp. 1057–1066. ISSN: 1616301X. DOI: 10.1002/adfm.200701245.

[93] Hyejung Kim et al. "A Critical Size of Silicon Nano-Anodes for Lithium Rechargeable Batteries". In: *Angewandte Chemie International Edition* 49.12 (2010), pp. 2146–2149. ISSN: 14337851. DOI: 10.1002/anie.200906287.

[94] Ill Ryu et al. "Size-dependent fracture of Si nanowire battery anodes". In: *Journal of the Mechanics and Physics of Solids* 59.9 (2011), pp. 1717–1730. ISSN: 00225096. DOI: 10.1016/j.jmps.2011.06.003.

[95] Xiao Hua Liu et al. "Size-dependent fracture of silicon nanoparticles during lithiation". In: *ACS Nano* 6.2 (2012), pp. 1522–1531. ISSN: 19360851. DOI: 10.1021/nn204476h.

[96] Hamed Haftbaradaran, Xingcheng Xiao, and Huajian Gao. "Critical film thickness for fracture in thin-film electrodes on substrates in the presence of interfacial sliding". In: *Modelling and Simulation in Materials Science and Engi-*

neering 21.7 (Oct. 2013), p. 074008. ISSN: 0965-0393. DOI: 10.1088/0965-0393/21/7/074008.

[97] Yong Seok Choi et al. "A simple technique for measuring the fracture energy of lithiated thin-film silicon electrodes at various lithium concentrations". In: *Journal of Power Sources* 294 (2015), pp. 159–166. ISSN: 03787753. DOI: 10.1016/j.jpowsour.2015.06.063.

[98] J.L. Beuth. "Cracking of thin bonded films in residual tension". In: *International Journal of Solids and Structures* 29.13 (1992), pp. 1657–1675.

[99] Toshio Nakamura and SM Kamath. "Three-dimensional effects in thin film fracture mechanics". In: *Mechanics of Materials* 13 (1992), pp. 67–77.

[100] M. a. McArthur, S. Trussler, and J. R. Dahn. "In Situ Investigations of SEI Layer Growth on Electrode Materials for Lithium-Ion Batteries Using Spectroscopic Ellipsometry". In: *Journal of The Electrochemical Society* 159.3 (2012), A198. ISSN: 00134651. DOI: 10.1149/2.004203jes.

[101] Benjamin Hertzberg, Jim Benson, and Gleb Yushin. "Ex-situ depth-sensing indentation measurements of electrochemically produced Si-Li alloy films". In: *Electrochemistry Communications* 13.8 (2011), pp. 818–821. ISSN: 13882481. DOI: 10.1016/j.elecom.2011.05.011.

[102] Lucas a. Berla et al. "Mechanical behavior of electrochemically lithiated silicon". In: *Journal of Power Sources* 273 (2015), pp. 41–51. ISSN: 03787753. DOI: 10.1016/j.jpowsour.2014.09.073.

[103] Fredric Ericson, Stefan Johansson, and Jan-Åke Schweitz. "Hardness and fracture toughness of semiconducting materials studied by indentation and erosion techniques". In: *Materials Science and Engineering: A* 105-106 (Nov. 1988), pp. 131–141. ISSN: 09215093. DOI: 10.1016/0025-5416(88)90489-2.

[104] J. J. Wortman and R. a. Evans. "Young's Modulus, Shear Modulus, and Poisson's Ratio in Silicon and Germanium". In: *Journal of Applied Physics* 36.1 (1965), p. 153. ISSN: 00218979. DOI: 10.1063/1.1713863.

[105] W. A. Brantley. "Calculated elastic constants for stress problems associated with semiconductor devices". In: *Journal of Applied Physics* 44.1 (1973), pp. 534–535.

[106] S F Dos Santos and J Rodrigues. "Correlation Between Fracture Toughness, Work of Fracture and Fractal Dimensions of Alumina-Mullite-Zirconia Composites". In: *Mater. Res.* 6.2 (2003), pp. 219–226.

[107] J. P. Maranchi et al. "Interfacial Properties of the a-Si/Cu:Active-Inactive Thin-Film Anode System for Lithium-Ion Batteries". In: *Journal of The Electrochemical Society* 153.6 (2006), A1246. ISSN: 00134651. DOI: 10.1149/1.2184753.

[108] Maria E. Stournara et al. "Li segregation induces structure and strength changes at the amorphous Si/Cu interface". In: *Nano Letters* 13.10 (2013), pp. 4759–4768. ISSN: 15306984. DOI: 10.1021/nl402353k.

[109] X. Xiao et al. "Improved cycling stability of silicon thin film electrodes through patterning for high energy density lithium batteries". In: *Journal of Power Sources* 196.3 (2011), pp. 1409–1416. ISSN: 03787753. DOI: 10.1016/j.jpowsour.2010.08.058.

[110] Michael David Henry. "ICP etching of silicon for micro and nanoscale devices". PhD thesis. California Institue of Technology, 2010, p. 219.

[111] S Timoshenko and S Woinowsky-Krieger. *Theory of plates and shells*. 2nd ed. McGraw-Hill Book Company, Inc., 1959, pp. 51–58. ISBN: 978-0070647794.